X-rays from Compton scattering around accreting black holes

Wilson, Colin David

X–Rays from Compton Scattering Around Accreting Black Holes

Colin David Wilson

A dissertation submitted to the University of Durham in accordance with the regulations for admission to the degree of Doctor of Philosophy.

Department of Physics, University of Durham, 2002.

Not from the stars do I my judgement pluck;
And yet methinks I have astronomy,

Sonnet XIV, William Shakespeare

The thing about a black hole,
its main distinguishing feature,
is it's black!
And the thing about space,
the colour of space,
your basic space colour,
is it's black!
So how are you supposed to see them?

Red Dwarf: Marooned

Ph.D. THESIS ABSTRACT

X–Rays from Compton Scattering Around Accreting Black Holes

Colin David Wilson (2002)

Compton scattering is one of the most important radiation processes from accreting compact objects. Hard X–rays can be produced by Compton upscattering of soft seed photons from the accretion disk. Here we use both theoretical and observational methods to investigate the hard X–ray emission around accreting Black Holes.

We attempt to observationally constrain the geometry of the accretion flow using the observed spectra from the outburst of a transient black hole. The rapid rise of the hard X–ray flux is almost certainly associated with most of the disk mass moving inwards, so the optically thick disk should not extend down to the last stable orbit until the outburst peak. The low/hard state is seen at the start of the rise showing that this is probably associated with a truncated disk. Attempts to derive the inner disk radius from reflection model parameters are inconclusive due to the effects of ionization.

We describe a new approach to numerically modelling Compton scattering around accreting sources by solving the distribution functions. This approach (based on work by Guilbert 1981) involves breaking the scattering into individual segments of space and time. We show how a coarse angle grid can be adapted to mimic an arbitrarily fine grid with very little increase in run–time. The resulting code automatically includes time dependent behaviour.

We extend the code to calculate the time dependent, self consistent electron distribution resulting from the Compton cooling. This can be used even where the Compton cooling time is shorter than the light crossing time. We show that any system in which the seed photons are dominated by reprocessing should produce soft lags of the order of the light crossing time. Future observations, with more sophisticated satellites, may be able to identify this lag.

Contents

List of Figures

Preface and Declaration

The work presented in this thesis was undertaken whilst the Author was a graduate student working in the Department of Physics at the University of Durham under the supervision of Dr. Chris Done. The majority of this work is the authors own but the observational work presented in chapter 3 was carried out in close partnership with Dr. Done.

The observational work shown in chapter 3 made use of data obtained through the High Energy Astrophysics Science Archive, provided by the NASA Goddard Space Flight Center.

The majority of the material in chapter 3 appears in Wilson & Done 2001.

The material in chapters 5 and 6 will be published in the near future.

Acknowledgements

With a work of this size there are always one or two people to thank. Firstly, of course, PPARC who kindly paid me to do this work and even more kindly paid for me to go to Washington to do it with other people. Also to the British Council who paid for me to work in Warsaw and sightsee in Krakow. I would also like to thank all the people I met at the Goddard Space Flight Centre and the Copernicus Institute who made me feel so welcome.

During the construction of the code and in my occasional forays into observations there are several people who have smoothed the road and deserve a mention. Thanks to Marek Gierliński who has been of great assistance, especially in those cases where my computer was refusing to play or XSPEC was being more obtuse than normal. Thanks also to Juri Poutanen, who consistently replied to my increasingly outlandish questions about the working of `compPS` with a speed and accuracy that amazed me. Finally thanks to Piotr Życki for answering all the e–mails I sent to him when I couldn't get hold of Chris.

I would also like to thank my family and friends for their support and willingness to forgive my trying to explain my work to them. Particular thanks goes to Nathan Courtney for entertaining conversation during coffee breaks. Also to Oli Glidewell and Kris Beckwith for proof reading several chapters. Finally to all the undergraduates I have had the pleasure of teaching during my three years. I couldn't have asked for a nicer group of people.

I would like dedicate this work to Nic Garner in exchange for her help, her support and her saying 'yes'. Finally huge thanks to Chris Done who has made my years here easier than I had thought and more entertaining than I would have believed. I really couldn't have done it without you.

Colin D. Wilson, 8th November 2002.

Chapter 1

The Theory of Accreting Black Holes

1.1 On the nature of extra–solar X–Ray sources

1.1.1 Discovery of the first sources

In 1962 a group of scientists from American Science and Engineering launched a small X–ray detector into space. Although they were looking for X–ray emission from the moon they detected an extremely bright source in the constellation of Scorpius (Giacconi et al. 1962). 'Sco X–1' as it was later named, was the first of many extra–solar X–ray sources which share a variety of remarkable properties, including intense X-ray emission which is rapidly variable (van der Klis 1994). This variability constrains the size of the emission region, since the properties of the source cannot change faster than the light crossing time (ignoring the effects of relativistic beaming).

Most of the galactic sources are in some form of binary system so a model was developed in which material passed from a larger object (secondary) to a more compact object (primary). The material would gain gravitational energy as it fell and emit this energy as light. Since neutron stars had been known to exist since the discovery of pulsars in 1968, they seemed a natural choice for the central object. Black holes were also considered although there was some doubt that any energy liberation would occur (Zeldovitch & Novikov 1971). The possibility of disk–like structures was suggested as a physically reasonable method of energy emission from around black holes (Prendergast 1960; Gorbastky 1965; Prendergast & Burbidge 1968; Lynden-Bell 1969; Shakura 1972; Pringle & Rees 1972). Shakura & Sunyaev (1973) derived equations which show a geometric thin disc structure by assuming

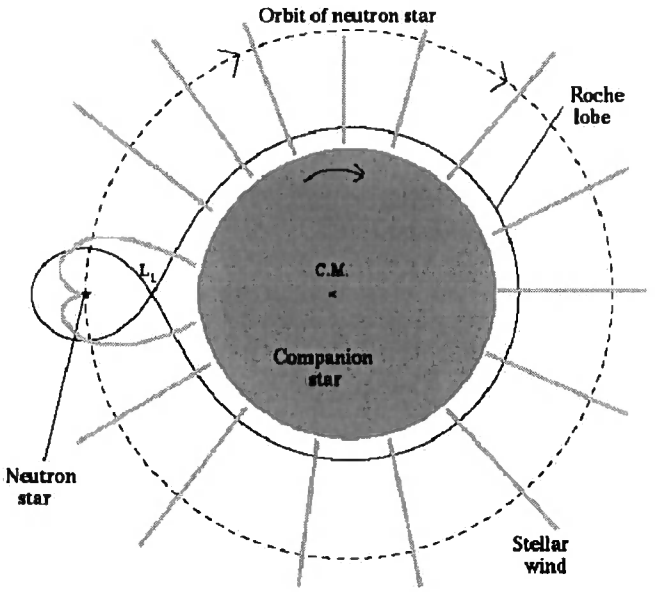

Figure 1.1: In wind accretion a high mass star ejects matter into the surrounding space. Its binary companion then accretes this matter as a turbulent flow. Taken from Audley 1998.

that the accretion flow is in steady state. When the mass estimates in binary systems were refined enough to show several compact sources which had to be more massive than the Chandresekhar limit, they were classified as galactic black hole candidates (GBHCs) (*e.g.* Cowley 1992).

Some extra–galactic sources have enormous luminosities, many times brighter than their galactic counterparts. These objects were named active galactic nuclei (if a host galaxy could be seen) and quasars (if no host could be seen). It later became clear that Quasars and AGN were the same type of object, viewed at differing distances and angles (*e.g.* Rowan-Robinson 1977). The luminosity of these sources precludes the possibility of their being neutron stars or ordinary black holes. Instead, they are classified as super–massive black holes. These monsters, thought to be $10^7 - 10^8$ times the mass of the sun are believed to reside in the centres of most galaxies (Magorrian et al. 1998).

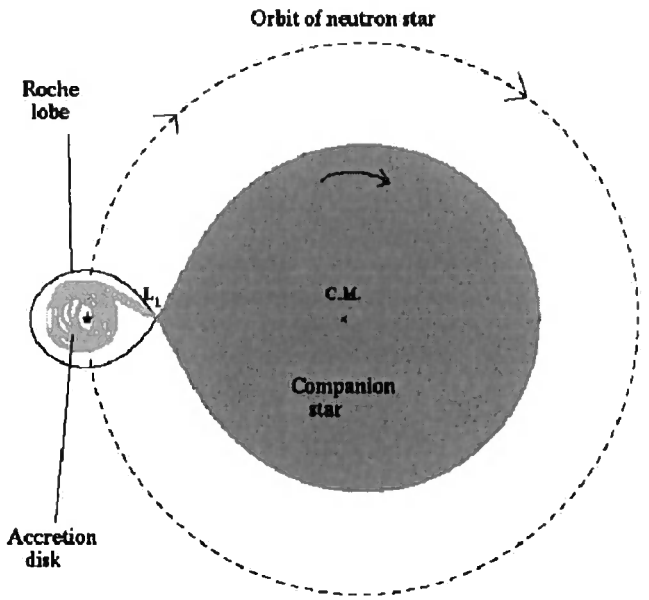

Figure 1.2: In Roche lobe overflow matter from a star falls under gravity towards the compact object via the inner Lagrange point. Due to the rotation of the star about the centre of mass of the system the material spirals inward rather than free–falling. Taken from Audley 1998.

1.1.2 Types of accretion

Theoretical investigation has shown that there are two basic circumstances in which accretion can occur in binary systems. Firstly, if the companion star is sufficiently large, its stellar wind will carry large amounts of material away from the star's surface. The material will encounter the compact object and fall onto it. This process is known as 'wind accretion' and is very complex. Figure 1.1 shows the a schematic of wind accretion. It only occurs when the companion star is massive enough to have a strong solar wind so these systems are known as high mass X–ray binaries (HMXRBs). High mass companion stars are not common in comparison to low mass stars and their lifetimes are shorter. The scarcity of such stars makes HMXRB systems comparatively rare (see the review by White, Nagase & Parmar 1995).

The second possibility is that the companion star is in such a close orbit with the compact object (relative to its size) that its radius is larger than the distance

between the star's centre and the centre of mass for the system. Some material from the edge of the star passes the point of equilibrium and 'falls' off the star toward the compact object. This is known as Roche lobe overflow and is shown in figure 1.2. Although this can happen where either high or low mass companions are present, the low mass systems are more common. Generally these are known as low mass X–ray binaries (LMXRBs) (White et al. 1995).

1.1.3 Useful accretion parameters

Even though the energy liberated by accretion is large, there is a theoretical limit on the rate at which mass can be accreted. As light is emitted by material, the resulting radiation pressure can push the incoming matter away from the compact object. It is possible to calculate the order of magnitude at which this effect becomes important, by making the following simple assumptions: the flow is steady, spherically symmetric over the whole of the compact object's surface and is composed of fully ionized hydrogen. Under such conditions the radiation force is provided by Thomson scattering. This force will be exerted mainly on the electrons since the cross–section is a factor $(m_e/m_p)^2$ smaller for protons. The radiation pressure will exert a force

$$F_{rad} = \frac{\sigma_T L}{4\pi r^2 c}$$

and the gravitational force is

$$F_{grav} = \frac{GMm_p}{r^2}$$

Thus the net force is

$$F_{tot} = \left(GMm_p - \frac{\sigma_T L}{4\pi c}\right)\frac{1}{r^2}$$

Clearly at a high enough luminosity, this force becomes zero and the material can no longer fall into the gravity well. This limiting value is called the Eddington luminosity (Eddington 1925). It is a result that is applicable to any system of matter/radiation equilibrium and is the reason that there is a limiting luminosity for stars (the very biggest O–type stars are skirting the Eddington limit). It is a very useful quantity when discussing accretion as it gives a method of quantifying

the amount of accretion that scales with the compact object mass. Hence

$$L_{\rm Edd} = 4\pi GMm_p c/\sigma_T$$

which can be parameterised to a value of

$$L_{\rm Edd} = 1.3 \times 10^{38}(M/M_\odot){\rm ergss}^{-1}$$

The Eddington limit is an approximation as the assumptions are clearly not justified. An accretion flow is rarely steady, contains a number of ions of different masses and is certainly not purely spherical. However, it is satisfying to note that the luminosities of many of the sources, both galactic and cosmological, are of the correct order of magnitude.

Another property of accreting systems which scales with the size of the system is the Schwarzschild radius. This is the radius of a black hole's event horizon. It is defined as

$$R_s = \frac{2GM}{c^2}$$

The value GM/c^2 is known as the gravitational radius (R_g). In the case of a non–rotating black hole, the event horizon is at 1 Schwarzschild radius, the last stable orbit for photons is at 1.5 and the last stable orbit for matter is at 3.

1.2 The accretion disk

1.2.1 Formation properties

The formation of an accretion disk follows from the dynamics of a binary system (where mass falls from a large star to a compact object). The companion star in a binary system has an intrinsic angular momentum, as does all the material coming from that star. As matter falls from the star it flows in a stream until it reaches its circularization radius (2–3 times smaller than the Roche lobe of the compact object) where it continues to orbit the compact object. As more mass falls into the orbit, a ring of matter is produced, allowing the transfer of angular momentum via energy dissipation. Some material loses angular momentum, speeds up and fall inwards to a faster Keplerian orbit. Similarly, some material is pushed outwards as

it gains angular momentum. This produces a disk stretching from some way inside the companion star's orbit to the compact object, where the disk material will be moving at relativistic speeds.

At present the exact nature of the dissipative mechanism in accretion disks is a matter of debate but it is generally agreed that it is a result of magnetic reconnection (as put forward by Balbus and Hawley 1991). They postulate a series of tangled magnetic fields which can interact, passing energy. The system, known as the Magnetic Rotational Instability (MRI) is self generating. It also produces very high viscosity values which match well with our observations of accretion disk viscosities (Smak 1999). There is some discussion as to whether the Balbus–Hawley mechanism works under all circumstances as it requires an ionized plasma to generate the fields. It seems unlikely that the process can operate as efficiently in low temperature disks as material below 10^4 K will be neutral. Since it cannot then maintain tangled magnetic fields, the mechanism will not work (Gammie & Menou 1998; Fleming, Stone & Hawley 2000).

1.2.2 Energetics of accretion disks

As a particle in a disk loses angular momentum it falls a small distance towards the compact object. In doing so, it moves down into the gravitational potential well and so gains energy. The potential energy in a Newtonian gravity well is given by

$$E = \frac{GMm}{r}$$

where M is the mass of the compact object and m is the mass of the particle at radius r. Consequently this is the maximum possible energy gain of a particle falling into a gravity well. However, because the particle is in an orbit and not in free fall, only half the potential energy gained is converted into kinetic energy. The other half, according to the virial theorem, increases the particle's temperature. Therefore for any given system,

$$E = \frac{1}{2}\frac{GMm}{r}$$

will be gained by material as it is accreted. It is then released as electromagnetic radiation (providing that there is some mechanism of converting internal energy to

radiation). In the case of a very compact object, the gravity well is so steep that the thermal energy gain is enormous. Consequently, the central regions of an accreting object will emit a huge amount of radiation.

Clearly, the total amount of available energy depends on the smallest radius achievable by the disk and this puts some limits on the efficiency of the accretion process. In the case of both black holes and neutron stars the smallest radius transpires to be roughly the last stable orbit (three Schwarzschild radii from the centre of the object). Below this radius, material rapidly spirals inwards in free fall (for black holes). Since all the potential energy is converted into kinetic, there is no extra to be liberated. This is known as the stress–free boundary condition (Abramowicz, Jaroszynski & Sikora 1978). The stress–free condition has recently been questioned by Agol and Krolik (2000) who suggest that magnetic connections can provide stress across this barrier. As a result the minimum orbit which can be used to generate energy is decreased. For the moment, however, we assume that a disk stretches to the standard last stable orbit. Given that, we can estimate the maximum possible accretion efficiency.

The radius of the last stable orbit for a black hole is given by

$$R = 3R_s = \frac{6GM}{c^2}$$

Substituting for R in the equation of available energy from accretion, we get

$$E = \frac{1}{12}mc^2$$

Thus the maximum efficiency (using Einstein's mass energy conversion) is $0.08\dot{3}$. Comparing this with the efficiency of nuclear burning, which is 0.007 shows how incredibly powerful accretion is as a source of energy. The efficiency can be used to find the maximum mass accretion rate for a system as we can apply the mass to luminosity conversion to the Eddington limit.

$$\dot{M}_{\rm Edd} = 1.4 \times 10^{17}(M/M_\odot){\rm gs}^{-1}$$

This is a very rough calculation as it does not take either general relativity or the possibility of the disk having a different inner radius into account. Providing that the energy gained by the matter is radiated, then the luminosity can be found

from the mass accretion rate $\dot{M} = dm/dt$. Hence

$$L = \frac{1}{2}\frac{GM\dot{M}}{R}$$

and

$$L = \frac{1}{12}\dot{M}c^2$$

The amount of luminosity released from material at radius R to $R + dR$ is

$$dL = \frac{1}{2}\frac{GM\dot{M}}{R^2}dR$$

and from the Steffan–Boltzman law

$$dL = 2\pi R dR \sigma_{SB} T^4$$

Equating these and rearranging gives the temperature as a function of radius.

$$T^4 = \frac{1}{4}\frac{GM\dot{M}}{\pi R^3 \sigma_{SB}}$$

We define $m = (M/M_\odot)$, $\dot{m} = (\dot{M}/\dot{M}_{\rm Edd})$ and $r = (R/R_s)$. Then converting the equation into a function of known constants gives

$$T = \left(\frac{G}{4\pi\sigma_{SB}}\frac{M_\odot \dot{M}_{\rm Edd}}{R_s^3}\frac{\dot{m}}{r^3 m}\right)^{1/4} = (3 \times 10^7)\left(\frac{\dot{m}}{r^3 m}\right)^{1/4} \text{K}$$

This equation does not include temperature shifts which result from angular momentum transport in the disk structure. Such shifts result in a constant of order unity. An accretion rate of 10% of Eddington and an inner radius of $3R_s$ generates an approximate value for a typical temperature in both GBHCs and AGNs. In the GBHC case, the mass of the central object is around $10M_\odot$. This gives a temperature of $\sim 10^7$ K, which is equivalent to 1 keV. So, for a galactic source, the accreting material will emit in the soft X–ray band. It is interesting to note that, in the case of AGN, the increased mass of the central object *decreases* the temperature. A black hole of mass $10^8 M_\odot$ would have a maximum temperature of only $\sim 10^5$ K, putting it in the UV band. In this case the increase in the mass of the accreting object is more than offset by the increase in disk surface area. As a result, although the liberated energy is bigger, the temperature of the disk surface is lower.

Instead of a simple Schwarzschild black hole it is possible to use a rotating Kerr metric (Kerr 1963). In this circumstance frame dragging makes the last stable orbit smaller (down to 1.2 gravitational radii in the maximally rotating case). This increases the efficiency up to values of $\sim 50\%$ (and consequently the temperature by $\sim 25\%$). It is sometimes used to explain those sources which are observed to be unusually hot and efficient (Fabian & Rees 1979, Zhang, Cui & Chen 1997).

1.2.3 The 'Shakura–Sunyaev' disk

Before examining some of the basic features of SS disks, we should look at the parameterization of the dissipative forces. Although we often talk of viscosity, it is the formation of torque within the disk that is the issue. By claiming that the dissipative forces are viscous we are limiting the torque to being formed locally and being proportional to the shear. Although there are a few possibilities for non–viscous torques, assuming a viscous paradigm produces reasonably convincing results (Krolik 1999).

Shakura and Sunyaev's idea was that, even though the viscosity mechanism was unknown, it would behave in similar ways to known viscosities. Hence the local viscosity was proportional to the local hydrodynamical stress.

$$\nu = \alpha c_s H$$

where ν is the kinematic viscosity averaged over depth, c_s is the local sound speed in the disk and H is the scale height (which is assumed to be much less than the disk radius: a thin disk). This is the famous 'Alpha prescription' from which the rest of the Shakura–Sunyaev disk is derived. This parameterization of viscosity is equivalent to the assumption that the heating rate of the protons in the disk is proportional to the local pressure. The actual value of α is unknown. Fortunately, the dependence of most of the disk parameters on α can be derived even without knowing α itself (the actual values of disk properties depend very weakly on α). Observations of genuine disks (especially those around white dwarfs which are considerably easier to observe), show the value of α to be less than or equal to 1, which matches well with the predictions (*e.g.* review by Osaki 1996). Although

the Balbus–Hawley mechanism does not generate a true viscosity, recent calculations have shown that α models can be obtained from the mechanism (Balbus & Papaloizou 1999).

The Shakura–Sunyaev disk equations are derived for those situations where the accretion flow is steady and the protons and electrons are at the same temperature. The height of the disk is calculated as a function of the radius and the other parameters are derived at the mid–plane. The details of the solutions vary depending on what form of pressure and opacity is dominant. In the following equations (taken from Treves, Maraschi & Abramowicz 1988) the opacity is assumed to be dominated by electron scattering. In the first case the disk is gas pressure dominated and in the second it is radiation pressure dominated. The original SS equations contain information about local pressure, density, luminosity and other such factors. However, to understand the stability of the disk, only two parameters need be discussed. The surface density of the disk (Σ) is a representation of how much mass is present in each point in the disk at any one time. To convert from this value to mass, one must multiply by the surface area and disk height (see Frank, King & Raine 1992). The temperature of the disk will vary with radius but also with height since the disk has a measurable thickness. The central temperature (T_c) is the temperature at the mid–plane of the disk. These equations are found by assuming that the disk is in a pseudo–Newtonian potential. Since we should really be using general relativity these equations are likely to be incorrect at small radii.

Case 1: $P \propto kT$, $\kappa = \kappa_{es}$

$$\Sigma = 7.08 \times 10^4 \alpha^{4/5} \dot{m}^{3/5} m^{1/5} r^{-3/5} f^{3/5} g cm^{-2}$$

$$T_c = 3.53 \times 10^8 \alpha^{-1/5} \dot{m}^{2/5} m^{-1/5} r^{-9/10} f^{2/5} K$$

Case 2: $P \propto T^4$, $\kappa = \kappa_{es}$

$$\Sigma = 4,24 \alpha^{-1} \dot{m}^{-1} r^{3/2} f^{-1} g cm^{-2}$$

$$T_c = 3.10 \times 10^7 \alpha^{-1/4} m^{-1/4} r_{10}^{-3/8} f^{2/5} K$$

$$f = 1 - \left(\frac{R_{in}}{R}\right)^{1/2}$$

where R_{in} is the innermost radius of the disk, $\dot{m} = \dot{M}/\dot{M}_{Edd}$, $m = M/M_{\odot}$ and $r = R/R_G$.

The profiles of these parameters with radius using a relativistic potential are shown in figures 1.3 and 1.4. In this circumstance, the disk is gas pressure dominated so the surface density of the disk decreases slowly with radius. A large amount of *mass* resides in the outer regions (where the disk area is much larger). The largest amount of energy gain occurs in the last few Schwarzschild radii so the disk is hottest near its centre. In general, the disk is radiation pressure dominated in its inner regions if

$$\dot{m} > \frac{1}{170}(\alpha m)^{-1/8}$$

(Shakura & Sunyaev 1973)

1.2.4 Boundary layers and advection

For a steady state disk, roughly half of the available energy will be liberated as the matter spirals inwards. What happens to the other half depends on the object at the receiving end. In the case of a neutron star or white dwarf, there is a surface onto which the matter must eventually settle. For a black hole there is no such thing. Any matter which falls far enough will simply slip quietly below the event horizon, never to be seen again. Any energy which the accreted matter may have had is lost to the universe and this includes the half which has yet to be liberated. This process is called advection, and becomes vital when considering the circumstances under which the assumptions of the SS disks break down.

As for neutron stars and white dwarfs, their surfaces will be rotating at considerably less than Keplerian velocity. In the last few orbits, the matter stream will be forced to slow to the velocity of the object's surface. The particles release all of their kinetic energy in one short region above the compact object (Popham & Sunyaev 2001). These regions, which are known as boundary layers, should be one of the simplest ways of differentiating between a neutron star and a black hole although detecting them has proven difficult (Narayan, Garcia & McClintock 1997).

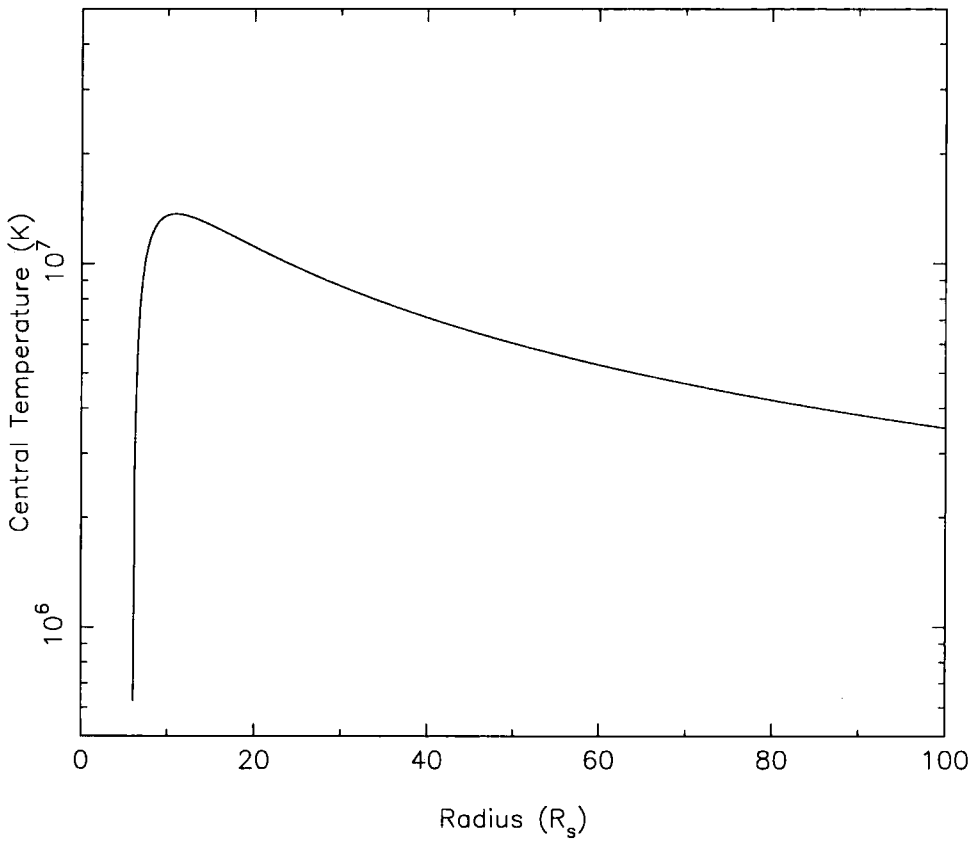

Figure 1.3: The relation of central temperature against radius (as a function of Schwarzschild radius) for a gas pressure dominated, Shakura–Sunyaev disk in a relativistic potential. This is calculated for a $10M_{\odot}$ non–rotating disk accreting at 10% of the Eddington limit. The disk is hottest nearest the centre because the energy gain from accretion is largest in the last few Schwarzschild radii. The temperature lowers around $6R_g$ as the matter is in free–fall and so gains no energy.

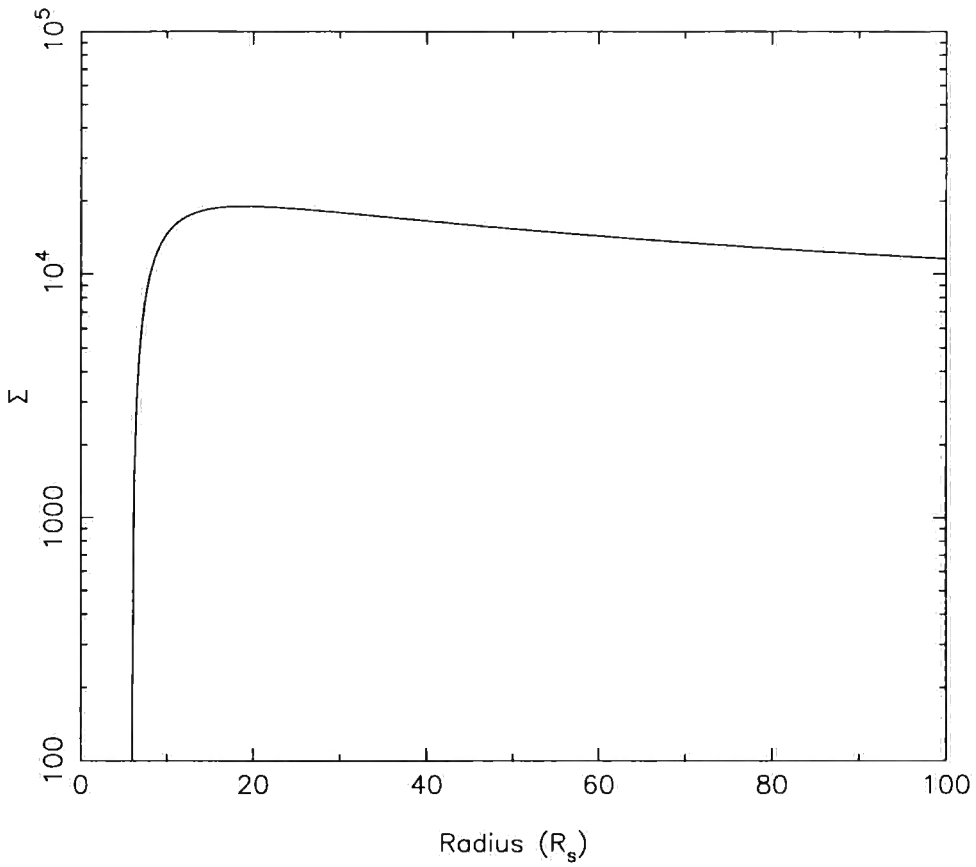

Figure 1.4: The relation of surface density against radius (as a function of Schwarzschild radius) for a gas pressure dominated Shakura–Sunyaev disk in a relativistic potential. This is calculated for a $10M_{\odot}$ non–rotating disk accreting at 10% of the Eddington limit. The surface density decreases towards the outer radii although the largest amount of mass is at the outer edge of the disk where the disk has the largest surface area.

1.2.5 The assumptions of the Shakura–Sunyaev disk

The Shakura–Sunyaev disk is considered as a mixture of protons and electrons, held together by electromagnetic forces. It seems likely that the gravitational energy gained as material falls inward is imparted mainly to the protons and then passed to the electrons and radiated. Shakura and Sunyaev assume that the energy transfer between the protons and the electrons is fast. Given that a standard SS disk is generally optically thick, this is a reasonable condition to impose. As a result of this transfer of energy, the electrons and protons remain in thermal equilibrium (a single temperature flow). However, the exact nature of the gravitational energy transfer is not known so it is possible that the energy is imparted directly to the electrons (Quataert & Gruzinov 1999). Provided that the thermalization time is short, a single temperature flow is still established.

In the SS disk, the assumption is also made that once an electron has gained energy, it radiates it efficiently and so loses the energy at approximately the same radius that it gained it. Local radiation is therefore the most important energy loss mechanism in the disk. Finally, a condition that the mass accretion rate is constant across the whole disk is imposed. If these assumptions are not true then the energetics of the situation change and the structure of the accretion flow can be very different to that of an SS disk.

1.2.6 Transients and the disk instability model

The most obvious difference between the prediction made by Shakura and Sunyaev and the observed reality is in the assumption of stability. It is taken as an initial condition that the disk is in a steady state. However most of the black holes in our galaxy fall into a class of object which shows that this cannot possibly be the case; these are the X–ray transients (Osaki 1974).

Transients demonstrate huge variability in luminosity, starting very low (normally below the detectable threshold) and increasing by several orders of magnitude over a very short period (several days). They then radiate at a very high level for several months, dying slowly down to invisibility (quiescence) again. The outburst (as this process is known) is very violent in those sources which are associated with

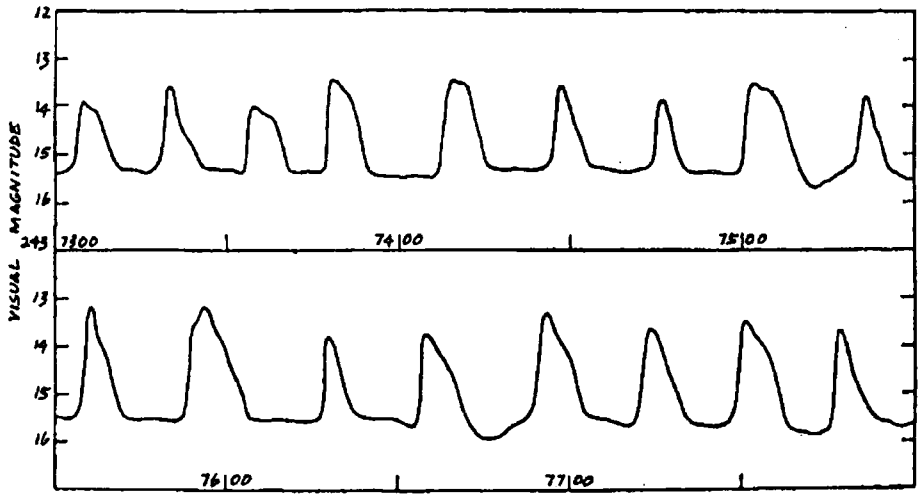

Figure 1.5: A typical lightcurve of a cataclysmic variable. It demonstrates repeating outbursts with a short recurrence time. The outburst has a small luminosity increase which is commonly associated with White Dwarves. Taken from Treves, Maraschi & Abramowicz 1988.

neutron stars and black holes. White dwarf outbursts are generally calmer and quasi–regular although this is not always the case (*e.g.* review by Lasota 2001). See figure 1.5 for a typical set of white dwarf outbursts. The luminosity increase is small and the outbursts recur.

For this sort of behaviour to occur, the rate of mass accretion onto the compact object must be changing. Although it is possible for the amount of material entering the disk from the secondary to change, this is an unlikely mechanism as the rate would have to change substantially on small timescales. Instead, we abandon the Shakura–Sunyaev hypothesis that mass accretion rate is constant across the disk and allow the possibility that the accretion rate changes both temporally and spatially.

The present model for an outburst is based on the disk instability model (see Lasota 2001 for an exhaustive review of all parts of the DIM). The basic principle was put forward by Osaki in 1974 and the model was fully established over the following decade (Hoshi 1979; Smak 1982; Smak 1984; Lin, Faulkner & Papaloizou 1985; Mineshige & Osaki 1983). Originally it was designed to explain white dwarf outbursts, but can be applied (with a little modification) to other systems.

The model calculates the time dependent disk structure and finds that the disk is not in the Shakura–Sunyaev state before the outburst begins. The calculated starting formation is called a quiescent disk and is found to be a cool flow with a flat radial temperature profile. This is has been confirmed by observations of white dwarf disks (Lasota 2001). The quiescent disk has a very low rate of mass transfer (and hence a low luminosity) which is not constant through the disk. Specifically, the rate of accretion onto the central object is lower than the rate at which material is passed into the disk by the secondary. As a result there is a build up of mass over time. This mass is stored in the outer layers and never reaches the inner regions.

When the whole disk is cool, there is very little opacity, so the radiation from within the disk can escape with little difficulty. However, as the amount of mass in the disk increases, local fluctuations become more likely to push the temperature high enough for the thermal photons to ionize Hydrogen. This sudden change in available opacity stops the photons from escaping. Instead, the energy from the photons is trapped in the disk causing the temperature to rise even further. This thermal runaway changes the local sound speed and so alters the rate of transfer of angular momentum. Gammie & Menou (1998) suggest that the change of temperature will cause the Balbus–Hawley viscosity system to start working, resulting in a local shift in the value of α. A 'heating wave' will then propagate through the disk increasing the mass accretion rate in its wake. The hot disk falls into a Shakura–Sunyaev formation, accreting at a high rate and consequently emitting at a high luminosity.

Generally, the accretion rate from the secondary is not high enough to support the high rate of mass transfer in the SS disk. Eventually enough of the mass stored in the disk drains away and a cooling wave forms. The disk then switches back to the quiescent flow and becomes radiatively dim. Since the disk is now back in its original formation, the cycle can begin again. The cycle can be seen in figure 1.6 which shows the regions of stability in the temperature/surface density parameter space. If the temperature and surface density is not on the line, the disk is heated or cooled until a stable state is reached. If a disk is perturbed while occupying the parameter space at the end of each bend, it is forced into a new stable state.

Such models can explain the amplitude, shape and frequency of the outbursts

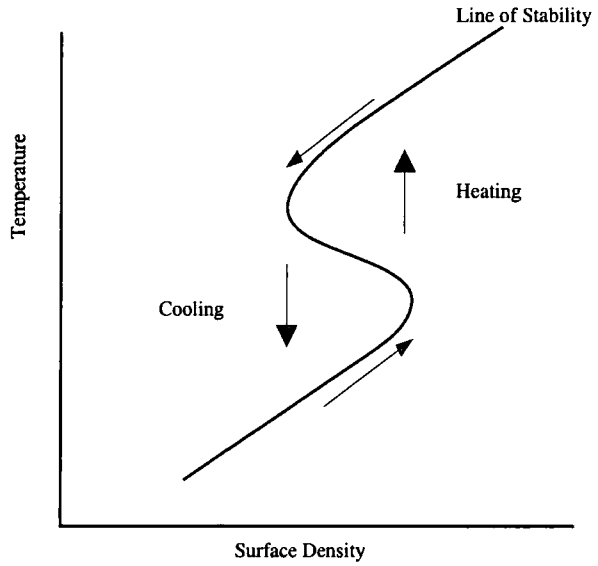

Figure 1.6: This graph of surface density against temperature shows the places where a stable accretion flow can exist. Perturbations can force the disk into regions of heating and cooling creating a limit cycle (shown by arrows) between the various stable solutions. In this way a small instability can generate a full outburst (Frank, King & Raine 1992).

seen in white dwarfs (Lasota 2001). In neutron stars and black holes the outburst behavior is different. Although outbursts do repeat, the timescales are much longer and much less regular. Similarly the lightcurves of individual outbursts are very different, both from each other and from the white dwarf case. Figure 1.7 shows a black hole exhibiting the fast rise, exponential decay behaviour. This is not unusual in black holes and neutron stars but is not always seen. Van Paradijs and Verbunt (1984) suggested that the outbursts of neutron stars and black holes has the same underlying DIM mechanism but making the model fit was generally unsuccessful (Lasota 2001).

Van Paradijs (1996) suggested that irradiation can solve these differences (see also King & Ritter 1998; Menou et al. 2000). In the case of a white dwarf, the amount of X–rays from the central source is quite low. This is not true for neutron stars and GBHCs. X–ray radiation from the central source can have several effects. The strong X–ray flux can keep the disk temperature above the critical level required for the cooling wave to start. As a result, the disk remains in outburst for a longer time. The disk loses a huge amount of material in this sort of outburst so the time necessary for another outburst to start is much longer (see Shahbaz et al. 2000 for

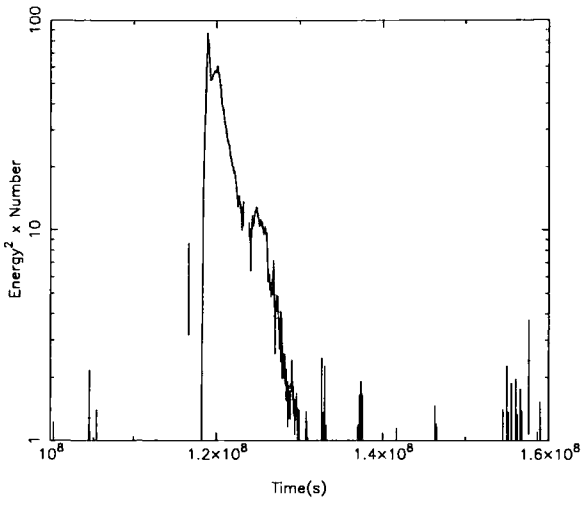

Figure 1.7: An outburst of the black hole J1859+226. This lightcurve approximately follows the fast rise exponential decay pattern predicted by the DIM (including irradiation). Unlike Cataclysmic Variables the luminosity increase is large and there is a long recurrence time (possibly with no recurrence at all). Such a clean curve is a rarity among neutron stars and black holes.

an observational view of irradiation).

Irradiation can also affect the companion star. If there is enough radiation from the central source, the outer layers of the star are heated, resulting in an increase in accretion rate. This can put the system into a state of quasi–stability resulting in a plateau in the outburst lightcurve (Esin, McClintock & Narayan 1997).

The advantages of the disk instability model is that it accurately predicts the behaviour of outbursts and provides a simple explanation for the difference between transient and steady sources. If the mass accretion rate is high enough, sources will be stable as the disk will always be in a standard hot state. A lower $\dot{m}$ leads to a disk which is capable of transition since the disk is not always in a Shakura–Sunyaev state. This model is well supported by those few sources (white dwarfs and a few Neutron star LMXRBs) whose accretion rate puts them very close to the line of stability. In these cases, the sources are stable for some length of time, then pass through a series of outbursts and eventually return to stability (Burderi, King & Szuszkiewicz 1998; Lasota 2001).

1.3 Alternative accretion structures at low mass accretion rates

While the disk instability model explains how a disk can change from a quiescent disk into a Shakura–Sunyaev formation, it does not explain the true nature of quiescence. The structure of the accretion flow during quiescence is by no means certain and there is no guarantee that a disk is the *only* available geometry. Several possible models for the flow (either the whole or in part) exist.

1.3.1 Quiescent disks

The quiescent disk is calculated to be very cool in comparison to standard disks (Lasota 2001). This could be a problem because the predicted (and observed) temperatures of quiescent disks are below the critical temperature necessary for the Balbus–Hawley viscosity mechanism to work (Gammie & Menou 1998). Without magnetic tangling the viscosity must be caused by a something different. Whatever the mechanism involved the angular momentum transfer must be apparently local. This is equivalent to saying that the quiescent disk is still controlled by an α type torque. (Lasota 2001).

X–ray fluxes are seen from the central regions of quiescent systems. They appear to come from the central regions of the accreting system implying that at least some matter reaches the compact object. (Mukai et al. 1997). Unfortunately, the required accretion rate implies a local disk temperature which would already have crossed the critical temperature necessary to generate an outburst (Meyer & Meyer–Hofmeister 1994; Lasota et al. 1996). It has been posited that the central regions do not contain a disk at all and that another type of flow is present. These 'hole in the disk' ideas are built on the principle of removing some of the assumptions which support the Shakura–Sunyaev disk.

1.3.2 The Shapiro, Lightman and Eardley solution

The main assumptions of a Shakura–Sunyaev disk are:

1. The mass accretion rate is constant across the whole accretion flow.

2. The gravitational energy gained by the protons is instantaneously passed to the electrons so the flow is in thermal equilibrium.

3. The electrons radiate almost immediately, so energy is liberated locally.

The result of the second of these assumptions is that the temperature of the protons and electrons is identical; the disk is a single temperature flow. The third means that radiation is the primary method of cooling the electrons (and consequently, the protons).

In the Shapiro, Lightman and Eardley solution (hereafter SLE) the second of these assumptions is relaxed. It is assumed that gravitational energy is still gained by the protons but there is no longer an instantaneous transfer of energy. The electrons can be at a different temperature from the hot protons. We now have a two temperature accretion flow where the protons have a much higher temperature than the electrons. It seems likely that the electrons do not gain much energy from gravity themselves and so remain at a lower temperature (Narayan, Mahadevan & Quataert 1998). They are also actively cooled by Compton scattering. In the SLE solution, an extended disk is assumed to exist in the outer regions of the flow. In the original formulation (Shapiro, Lightman & Eardley 1976) this outer area of matter flow was a Shakura–Sunyaev disk, which became an SLE at a transition radius. Since we are trying to explain outbursts, we require the presence of a cool quiescent disk instead. Photons from this extended disk irradiate the hot flow. Consequently they collide with the electrons and gain energy, lowering the electron temperature. As the protons are at roughly the virial temperature, the flow is geometrically thick, with $H \sim R$.

One of the principle problems with the SLE solution is its instability. A slight perturbation of its temperature apparently leads to a catastrophic runaway (Piran 1978; Wandel & Liang 1991; Narayan & Yi 1995). This transforms the SLE into our second form of optically thin flow.

1.3.3 Advective flows

The advection dominated accretion flow (ADAF) is built on the same principles as the SLE solution. Again a two temperature plasma is generated in an optically

thin environment, and again the flow has a height similar to its radius. The main difference in this case is that the primary cooling mechanism is advection. Instead of being liberated (eventually) by radiation from the electrons, most of the energy is carried by the protons into the event horizon. Of course, this should lead to different observable behaviour when the compact object is a neutron star rather than a black hole. The presence of a surface would mean that a boundary layer would form and all the remaining energy would be liberated there (Narayan & Yi 1995; Garcia et al. 2000). In the case of black holes, these ADAFs are extremely under–luminous. With no efficient radiation mechanism, the amount of X–rays emitted from the central regions are far smaller than would be expected given the mass accretion rate. This explains the low levels of flux in quiescence (Narayan & Yi 1995).

Both ADAFs and SLEs have a critical mass accretion rate above which they cannot exist. This rate (about 10% of the Eddington limit) is that at which the flow becomes dense enough for a single temperature plasma to form. Since advection is no longer dominant and since radiation is not only present but efficient, the optically thin flows collapse into a Shakura–Sunyaev disk. This can be seen in figure 1.8, where the SLE/ADAF branch has a limiting point in its temperature/surface density relation. Consequently there is a mass accretion rate above which such flows cannot remain stable. It is interesting to note that, at this point, the two optically thin flows are indistinguishable (Igumenshchev, Abramowicz & Novikov 1998; Chen et al. 1995; Zdziarski 1998).

Recent work on hydrodynamic modelling of ADAFs has shown that advective flows exhibit significant convection (Igumenshchev, Chen & Abramowicz 1996; Igumenshchev & Abramowicz 1999; 2000; Stone, Pringle & Begelman 1999; Igumenshchev, Abramowicz & Narayan 2000). The simulations show that convection severely dampens the accretion rate, efficiently transporting energy outwards. These new flows have been termed convection dominated accretion flows, or CDAFs (Narayan, Igumenshchev & Abramowicz 2000; Quataert & Gruzinov 2000; Abramowicz et al. 2002).

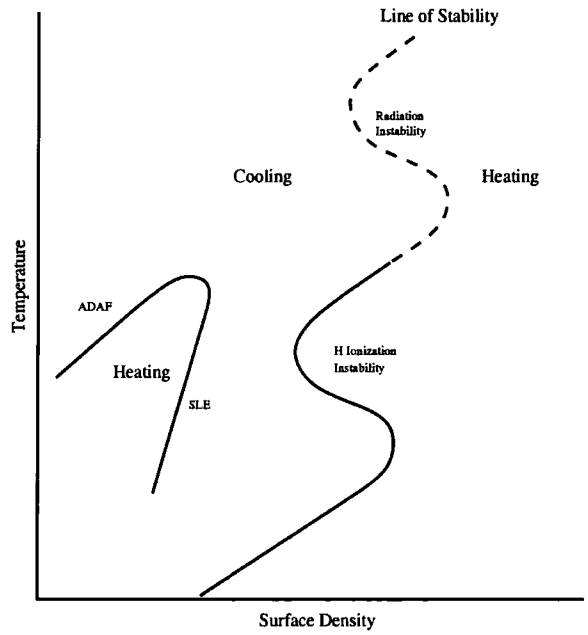

Figure 1.8: This graph of surface density against temperature shows the places where a stable flow can exist. Perturbations can force a stable flow into regions of instability which can change the disk structure radically. Clearly the SLE and ADAF branches cannot exist at high densities and temperatures. Instead, they have a limiting mass accretion rate above which they collapse into a disk.

1.4 Alternative accretion structures at high mass accretion rates

1.4.1 Radiation instabilities and slim disks

Having discussed the problems of disk structure at low accretion rates, it is also important to mention how the structure is affected by extremely high rates of mass transfer. In the Shakura–Sunyaev disk, the heating rate of the protons is assumed to be proportional to the total pressure in the disk (the α prescription). This is perfectly reasonable when the disk is gas pressure dominated, which is the case of SS disks, SLEs and ADAFs. Gas pressure is proportional to temperature ($P_{gas} = nkT$) so an increase in disk temperature leads to a similar increase in heating. This needs to be balanced by an equally similar increase in radiative cooling. Normally, this balance is achieved, however, at high enough rates of accretion, radiation pressure becomes dominant. Such pressure has a much higher temperature dependence ($P_{rad} = a_{RAD}T^4$) and so a slight temperature increase leads to a huge increase in heating rate. Standard radiative cooling cannot keep up and so the disk becomes unstable (Stella & Rosner 1984; Abramowicz et al. 1988).

With such a *very* large amount of mass falling onto the compact object, the disk becomes extremely optically thick in its central regions. As a result the photons within the disk may be lost into a black hole before the energy they carry has the chance to escape. This is merely a different form of advection where the disk is *too* dense. Optically thick advective cooling can stabilise the disk and this new type of flow is called a slim disk (Abramowicz et al. 1988). Since we now have another S–curve on our stability diagram (figure 1.8), we have another limit cycle of accretion rate and surface density which the disk can pass through. Observationally this should mean that the disk can outburst again, starting at high accretion rates and jumping to very high ones (Pringle, Rees & Pacholczyk 1973; Lightman & Eardley 1974; Abramowicz et al. 1988; Szuszkiewicz & Miller 2001).

This argument relies on the assumption that heating is proportional to local pressure. Due to our sketchy understanding of the magnetic viscosity mechanism, this may not be the case. If the heating is proportional to gas pressure only, then

the radiative instability will never be encountered and the Shakura–Sunyaev disk will continue to be stable even at very high accretion rates. Eventually, optically thick advection will become an issue again and the SS disk will gradually become a slim disk. The important point is that there is no instability. Thus there is no S-curve and so no limit cycle. This sort of disk, where the viscosity is dependent only on the gas pressure, is known as a β disk (Abramowicz et al. 1988; Stella & Rosner 1984). If the α prescription is incorrect at these mass accretion rates, we would expect to see no such thing as a high luminosity outburst cycle (with high mass accretion rates). Interestingly, most objects pass through the critical region of accretion rate without any problems whatsoever (Gierliński , Maciolek–Niedzwiecki & Ebisawa 2001). Only GRS1915+105 exhibits this type of luminosity cycle and that could be explained by matter ejection in the jet (Migliari, Vignarca & Belloni 2001; Janiuk, Czerny & Siemiginowska 2002).

1.5 Summary

It is clear that while many of the principles of accretion have been established, some key details are still remarkably vague. It is certain that a disk of the Shakura–Sunyaev type does occur in nature, albeit only in a few steady sources and at the high luminosity end of outburst. A combination of the principles of ADAFs, CDAFs, SLE flows and quiescent disks is the likely form for low luminosity accretion flows but there is still no convincing theory for quiescence. Equally, the concept of slim disks (or β disks) at very high mass accretion rates opens up the possibility that the SS disk exists only in a *very* limited region of parameter space. It is likely that the key to understanding disk behaviour in general lies in magneto-hydrodynamics. The Balbus–Hawley mechanism appears to be a robust theory for the nature of energy transfer in disks and so increasingly detailed disk models can be constructed. It is this sort of model, in conjunction with observations, which will provide the next generation of accretion disk theories.

Chapter 2

Observations of Accreting Black Holes

2.1 Analysing variability in X–ray lightcurves

Theories of accretion are meaningless without some level of observational testing. Although X–ray observations of compact object sources have been carried out for over three decades, it is only in the last fifteen years that the instruments have been sensitive enough to test the theories effectively.

The light from an accreting X–ray object can be examined in a variety of ways. Transients clearly show enormous variation in their X–ray luminosity and the shape of the outburst light curve can be examined in relation to the disk instability model. The model can be used to predict rise times, recurrence times, re–flares and other features of a light curve. Although there is some model dependence, the DIM can be used to find approximate values for several disk parameters (*e.g.* size, average accretion rate; Lasota 2001). Figure 2.1 shows an example of an observed lightcurve. It shows the ASM lightcurve from the 1998 outburst of the black hole XTE J1550-564 (of which more is discussed in chapter 3). The system remained in outburst for several months before fading exponentially.

Analysis of lightcurves probes the behaviour of X–ray sources on long timescales (hours/days). Fourier analysis is used to explore the nature of accretion on smaller times. The squared Fourier transform of a light curve shows the relative power associated with different frequencies. Generally there is a flat spectrum at low frequencies which dies off at higher ones. Sharp peaks are occasionally noted at certain frequencies and are called quasi–periodic oscillations (QPOs). They are quasi–periodic because, although they linger around particular frequencies, they

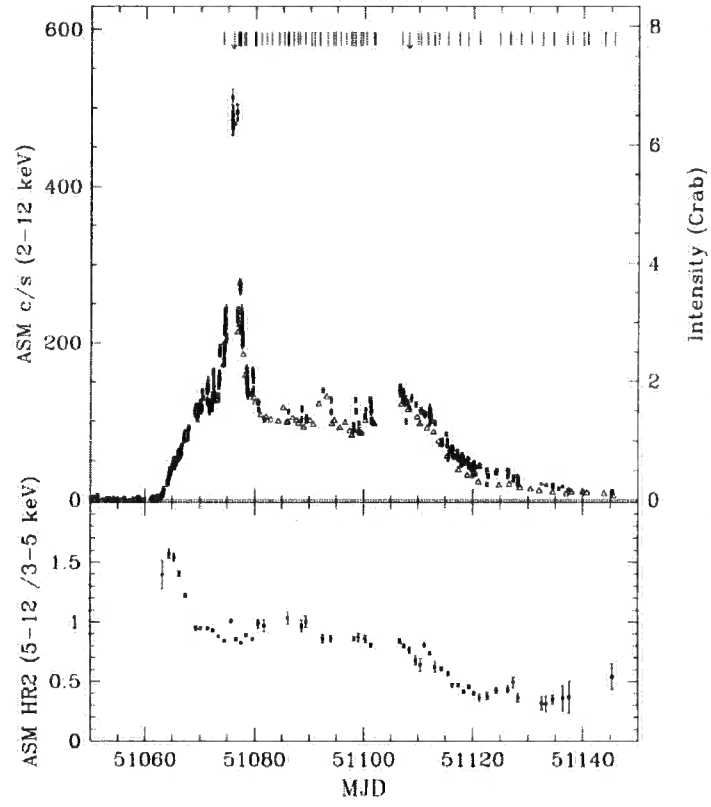

Figure 2.1: The light curve of this 1998 outburst of J1550-564 shows the sort of variability that can be seen in a real outburst. The initial rise peaks at an unusually high luminosity level. Instead of an exponential decay, the luminosity settles to a plateau for several months before dying away to quiescence. Taken from Sobczak et al. 1999.

are not at a constant period. They tend to be divided into low frequency QPOs and high frequency kilohertz QPOs. These high frequency QPOs are most often seen in neutron stars but have recently been detected in GBHCs as well (for a review of QPOs and power spectra see van der Klis 2000). Figure 2.2 shows the power spectra of several sources. All show a plateau at low frequencies which suddenly turns down above some break frequency. This is seen in both black holes and neutron stars showing that the timing behaviour is consistent between both types of compact object. The low frequency QPO is normally near the break frequency. A close up of specimen high–frequency QPOs can be found in figure 2.3 showing that they are made up of several peaks.

There are many models of QPO formation, most of which rely on some way of picking out the spin period of the compact object. Some models use the magnetic field of a neutron star to generate the oscillations, but this fails to explain how QPOs would be seen in black holes where there can be no magnetic connection between black hole and the disk (van der Klis 2000). A second theory uses relativistic frame dragging to generate oscillations in the disk which are related to the spin frequency of the object and the precession frequency of the disk. The advantage of this theory is that it can apply to any compact object irrespective of whether a magnetic field is present (Stella & Vietri 1998; Psaltis and Norman 2003).

2.2 Energy spectra of accretion flows

2.2.1 Spectra of accretion flows: The disk black body

The other main method of analysing accreting systems is to make a spectrum of the X–ray light by energy rather than variability. This is a particularly useful way of analysing data as, unlike the power spectra, we possess several physical models of accretion behaviour with which we can interpret the data.

The spectra from nearly all accreting sources share a set of common features. The two most obvious spectral components are the thermal hump and the powerlaw tail which are shown schematically in figure 2.4. The soft X–ray thermal component is from the disk. At any particular radius, an optically thick disk emits approxi-

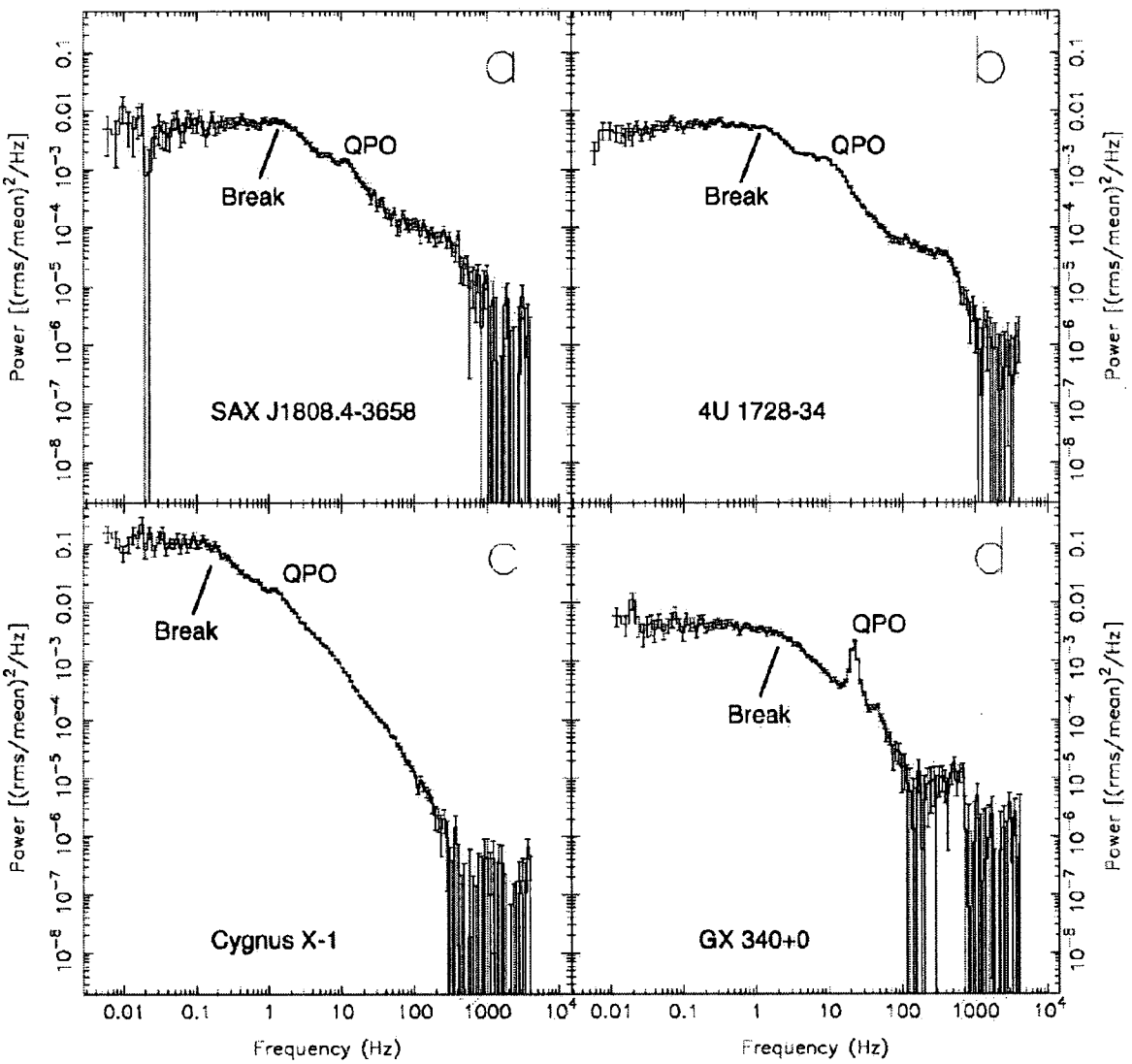

Figure 2.2: These power spectra from a variety of sources all show the usual features. These include a plateau at low frequencies followed by a downturn at a break frequency. A variety of low frequency QPOs can also be seen. Plates a, b and d are neutron stars but plate c shows the power spectrum from a black hole. Taken from van der Klis 2000.

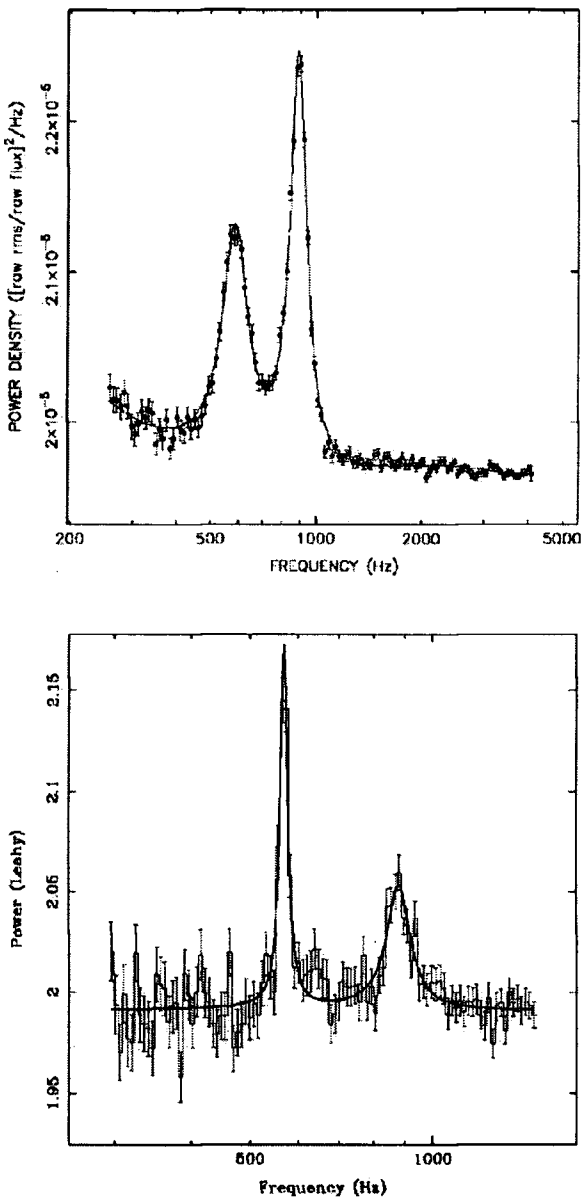

Figure 2.3: Detail of high–frequency Quasi-Periodic Oscillations showing that they are made up of several peaks at a variety of frequencies. Top panel shows a QPO from Sco X–1 and the bottom shows 4U 1608–52. Both of these are neutron star sources. Taken from van der Klis 2000.

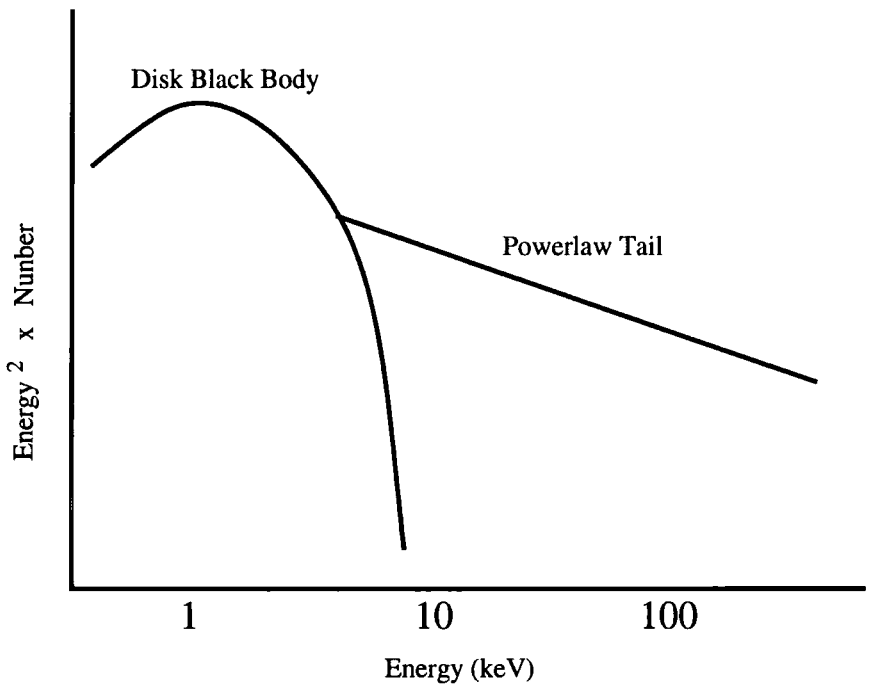

Figure 2.4: This schematic spectrum shows the two primary components of a spectrum from an accreting black hole. A black body like component is seen at low energies with a powerlaw tail that extends out onto the hard X–ray region.

mately as a black body (because the disk has a single local temperature). The black body temperature, which characterises the emission, will be a function of radius so the entire disk radiates as a series of black bodies of different temperatures. Since parts of the disk are rotating at relativistic velocities, doppler shifting and gravitational redshift also affect the emission in a radius dependent way (Ebisawa et al. 1994; Laor 1995).

The hottest temperature (and hence highest energy) in such a profile will depend on the closest radius that the disk reaches. Ideally, one could use the profile of this thermal emission to test if a disk extends to the last stable orbit or instead truncates, leaving a hole to be filled by an inner, hot accretion flow. Unfortunately, the amount of uncertainty generated in deconvolving X–ray spectra is so large that this method has significant uncertainties. Even if deconvolution were possible, there are theoretical difficulties in modelling the disk emission. Depth effects can significantly change the disk's spectral profile. These problems are examined in detail in Merloni, Fabian & Ross (2000).

2.2.2 Spectra of accretion flows: The hard X–ray tail

The other obvious component is the tail of photons extending out into the hard X–ray regions. Our original picture of accretion flows (as examined in chapter 1) predicted maximum temperatures in the soft X–ray regions because we only accounted for direct thermal emission from the disk. The cause of these harder X–rays is Comptonization of the soft photons by hot electrons (Sunyaev & Titarchuk 1980). To generate such a tail, thermal photons emitted by the disk travel through a region of electrons, which are at relativistic temperatures. Compton scattering takes place, draining energy from the electrons and increasing the frequency of the photons (Sunyaev & Trumper 1979). The observed photon spectra imply that a significant amount of the energy gained in accretion can be dissipated via Comptonization in an optically thin environment. Such a region cannot be the disk, which we know is optically thick and cannot reach the necessary temperatures. Consequently, the hot electrons must either be above the disk or parts of the accretion flow must be optically thin (*e.g.* an inner hot flow). To differentiate between these

regimes, it is vital to look at the observable elements of disk spectra.

2.3 Hard X–ray reprocessing by a cold disk

By considering the Compton scattered photons which escape the optically thin region we can infer some of its properties. Some of these photons head back towards the disk where they interact with the cold (relative to them) disk material. This reflection (if properly understood) can allow us to derive parameters of both the disk and hot electron cloud. Reflection is a balance between photo–electric absorption and Compton scattering. Low energy photons have a high absorption probability and so a low chance of reflection. These photons are absorbed by the disk material and re-emitted at the local black body temperature (this is called reprocessing). Higher energy photons are Compton downscattered to lower energies by the cool disk electrons. The resulting reflected photons have a very specific spectrum (Lightman & White 1988; George & Fabian 1991; Matt, Perola & Piro 1991). This distinctive component has been clearly detected in both AGN (Pounds et al. 1990) and GBHCs (Done et al. 1992).

The reflected spectrum (shown in figure 2.5) is made of several components. At low energies, absorption dominates so few photons are reflected. Those photons at the lowest energies are the most absorbed so reflection rises towards an energy of ~ 6 keV. Iron is the heaviest element found in accretion disks so absorption tails off at energies higher than the absorption edge energy of iron (~ 7 keV). As a result, Compton scattering is the dominant mechanism at the higher energy end of the spectrum.

2.3.1 Iron fluorescence as a method of measuring disk parameters

One of the most interesting components of the reflected spectrum is the line emission from iron in the disk. All elements in the accreting material will fluoresce but iron, at the highest energy, is the most visible. The line, which is emitted at energies around $6 - 7$ keV (depending on ionization), can be used as a measure of the innermost

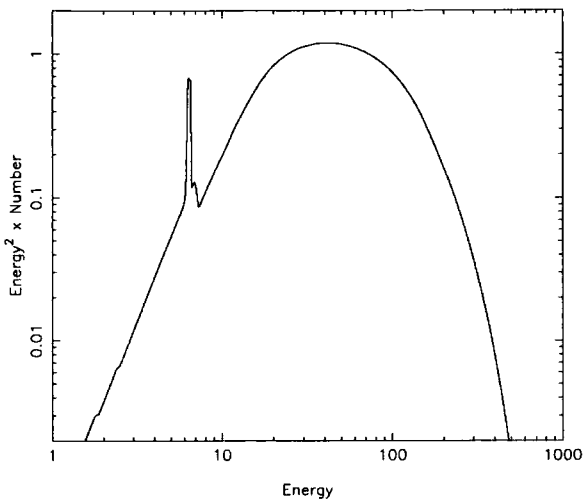

Figure 2.5: The above spectrum was constructed with the `thComp` model (Zdziarski, Johnson & Magdziarz 1996) using an illuminating powerlaw with a spectral index of 1.8. It shows the signature of neutral reflection. At low energies most of the incident energy is photo–electrically absorbed. The iron fluorescence line and absorption edge can be seen at 6-7 keV. At higher energies, Compton downscattering reduces the reflection probability at the highest energies so the spectrum tails off.

radius of the disk. Like all emission from the disk it is affected by relativistic doppler shifts and gravitational redshifts. These radius dependent effects result in very distinctive line profiles. The process by which a narrow fluorescence line is transformed into a broad component is shown in figure 2.6. Doppler shifts split the line in two as it is both red and blueshifted at different points in the disk. Special relativistic effects boost the blue peak and dampen the red. General relativity (in the form of gravitational redshift) lowers the energy of the whole feature. Since the line is affected differently at each radius a smeared version is built up which looks nothing like the original line (Fabian et al. 1989; Fabian et al. 2000; see figure 2.6). Since an iron line will only be seen where there is a disk to reflect, the innermost radius should be observable from the width of the iron line (Fabian et al. 2000).

2.3.2 Ionized reflection

Clearly, because so much of the reflected spectrum is a function of the disk absorption opacities, ionization is going to make a large difference. At mid ionizations, the low atomic number elements are stripped of all electrons and so are unable to

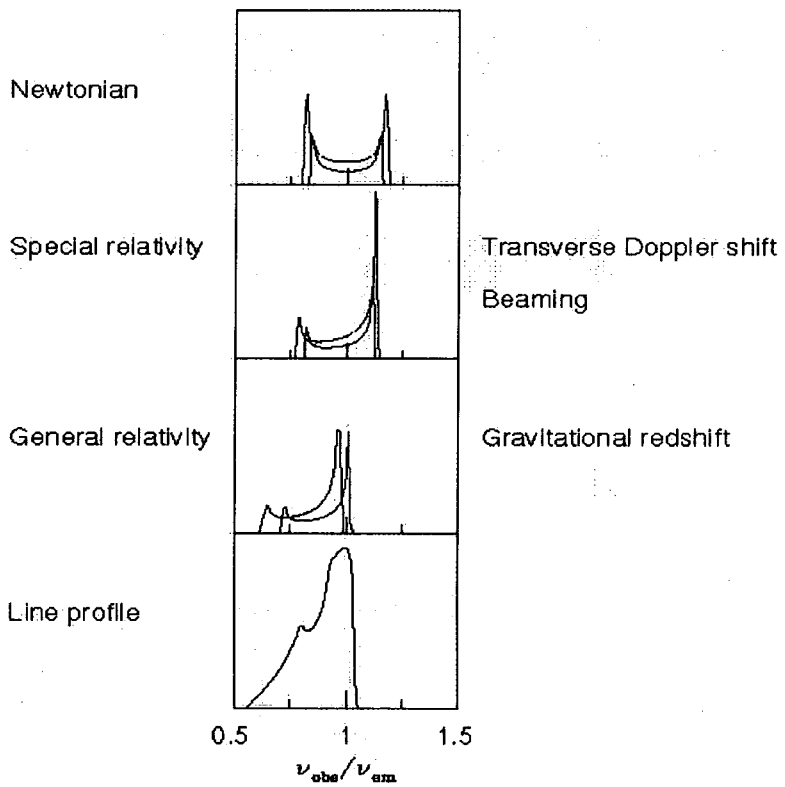

Figure 2.6: The reflected iron line here has been shaped by doppler shifting (top panel), relativistic beaming (second panel) and gravitational redshift (third panel). The final result (bottom panel) is clearly different from the single peak that we would expect from an atomic line. Picture taken from Fabian et al. 2000.

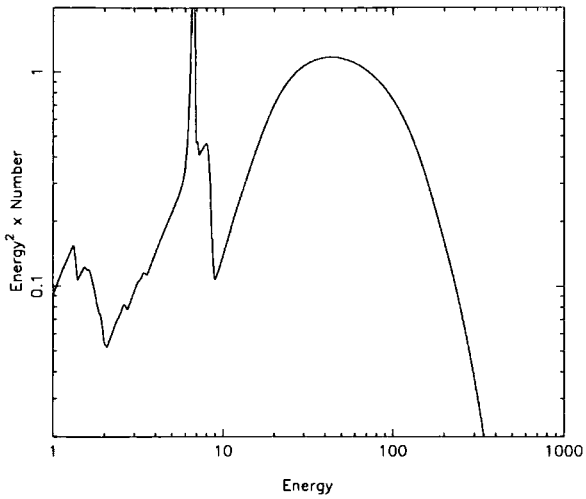

Figure 2.7: The above spectrum was constructed as in figure 2.5 but with a spectral index of 1.8. It shows partially ionized reflection. Note the increased iron line and edge at 6-7 keV and the loss of absorption at lower energies. This loss of absorption results in a series of complex features which depend heavily on ionization state.

absorb photons. As a result, low energy photons are not absorbed but mid energy ones are. This results in a complicated series of lines and edges which changes with the ionization state of the disk (see figure 2.7). The iron line also moves toward 7 keV as material at higher ionization state fluoresces at higher energies.

At high enough levels of ionization, all the elements are stripped of their electrons and so are unable to absorb or emit photons. The reflection spectrum is generated by Compton scattering only. The resulting spectrum is of the same index as the incident spectrum at low energies and rolls over at around 100 keV as any photon with a higher energy are Compton downscattered by the disk electrons (see figure 2.8).

2.3.3 Correlation between amount of reflection and spectral index

The amount of reflection in an accreting system can be represented by the value $\Omega/2\pi$. This is a solid angle showing how much of the sky is filled by reflecting material as seen from the hard X-ray source. A small hot region sitting immediately above a disk (possibly part of a corona or an individual flare) has $\Omega/2\pi$ equal to

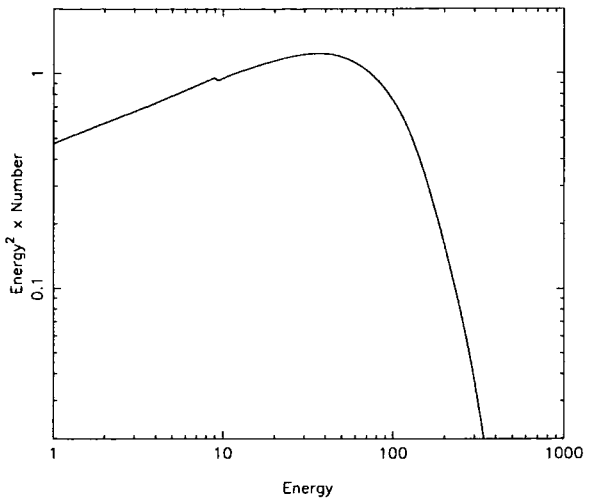

Figure 2.8: The above spectrum was constructed as in figure 2.5 but with a spectral index of 1.8. It shows fully ionized reflection. The loss of all absorption features leaves only a Compton scattered spectrum. It matches the spectral index of the incident spectrum until around 100 keV when a roll–over occurs due to Compton downscattering.

unity (as half the sky is filled with reflecting material). In the case where there is a hot flow in the centre of the disk, the value is less.

Observations of both AGN and GBHCs show a correlation between the reflected fraction and the spectral index of the hard X–ray powerlaw. Figure 2.9 shows how a flat powerlaw is associated with a low reflected fraction whereas a steeper powerlaw tends to be seen with a higher reflected fraction (Zdziarski, Lubiński & Smith 1999). Correlations between QPO frequency and reflection, and relativistic line width and reflection have since been found (see figure 2.10) (Gilfanov, Churazov & Revnivtsev 2000).

The correlation can be explained in several ways. In the model where there is a hole in the disk filled with a hot electron cloud, the disk penetrates further into the hot cloud as the outburst progresses. This leads to an increase in the level of reflection. The presence of more soft photons from the disk drives down the temperature of the hot electrons, steepening the spectrum. This model also predicts the change in QPO frequency as the inner radius of the disk moves to generate the change in reflection (Zdziarski, Lubiński & Smith 1999).

A different interpretation is that the disk always extends to the last stable orbit but has a corona moving with bulk velocity towards or away from it. If this corona

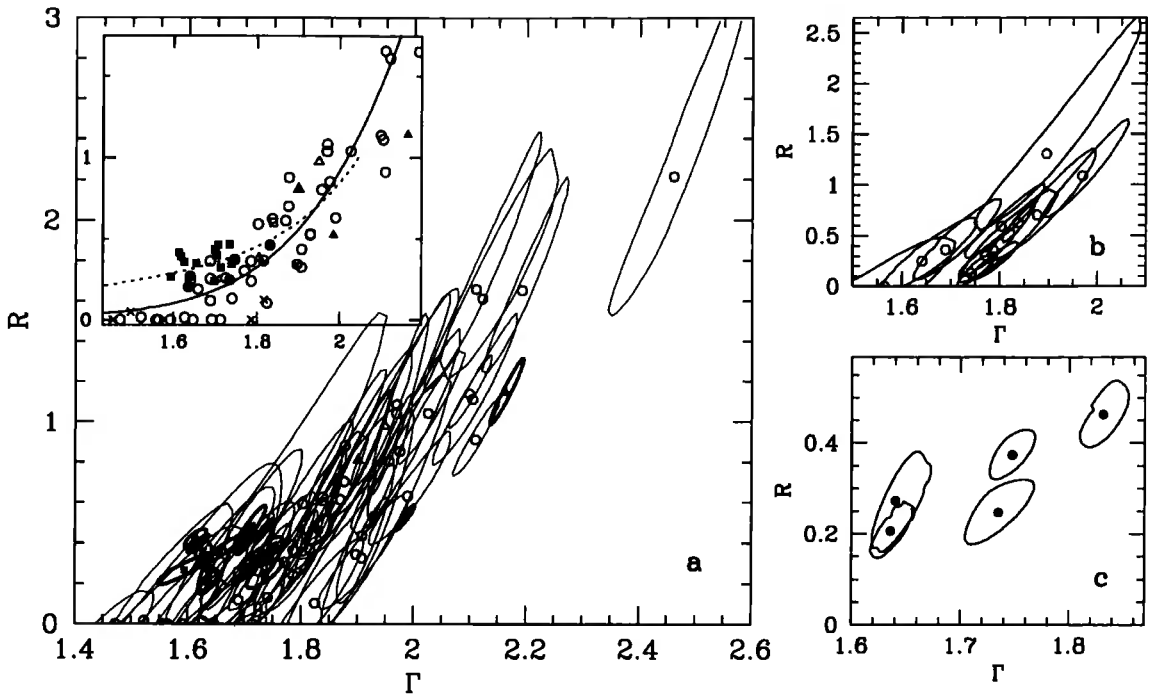

Figure 2.9: This plot shows the observed correlation of spectral index with reflected fraction in observations of AGN and GBHCs. Panel (a) shows the data and the models (curves inset) while panels (b) and (c) show the correlation from NGC 5548 and GX339–4 respectively. Taken from Zdziarski, Lubiński & Smith 1999.

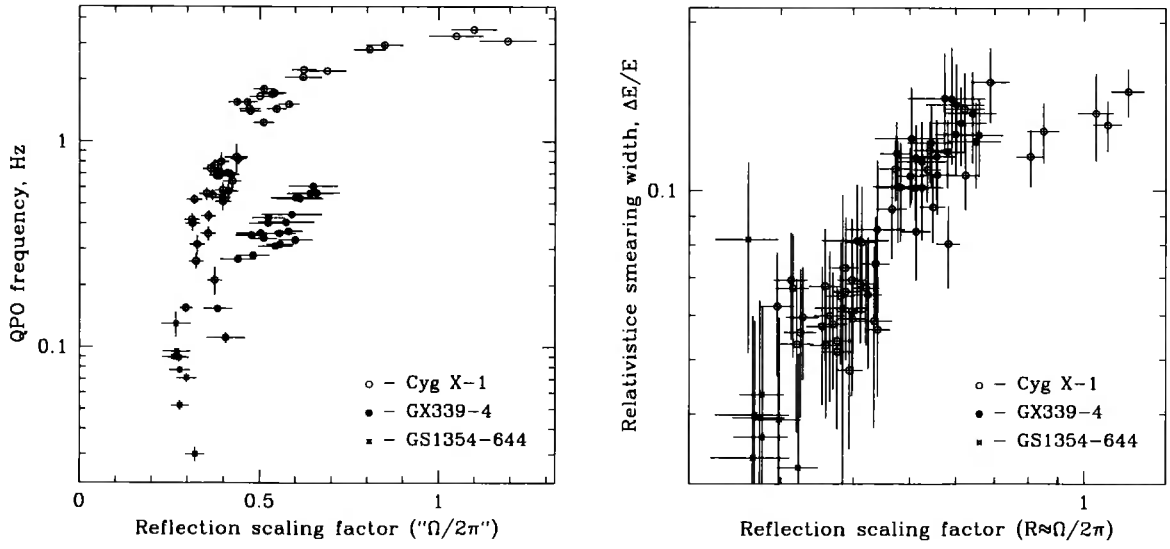

Figure 2.10: These plots show the observed correlation of QPO frequency with reflected fraction (left panel) and the correlation of relativistic smearing line width with reflected fraction in observations of Cyg X–1, GX339–4 and GS1354–644. Taken from Gilfanov, Churazov & Revnivtsev 2000

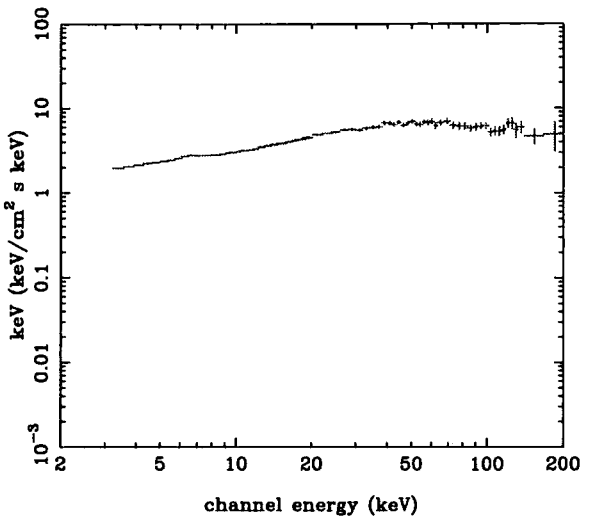

Figure 2.11: This spectrum shows the classic low state where there is very little soft X–ray flux and a hard X–ray tail which generally rolls over at high energies. In this case the roll–over is beyond our instrument's range. The spectrum is taken from the 1998 outburst of J1550–564.

is moving at sufficient velocity the hard X–ray photons would be boosted in the forward direction and suppressed towards the disk, lowering the level of reflection and reprocessing. The low level of reprocessing generates a hard spectrum as the electrons are not efficiently cooled. If the bulk velocity slows, reflection increases and the spectral index steepens. However, this model does not predict the observed change in QPO frequency with reflection (Beloborodov 1999).

2.4 Spectral states: The behaviour of transient spectra

The simple spectrum shown in figure 2.4 is not truly representative of the variety of spectral shapes (or states) which can be generated by accreting compact objects. Changes of these states are occasionally seen in stable sources but more commonly in transients.

The lowest luminosity state (low/hard) is characterised by a *very* hard powerlaw tail with no (or very little) disk emission (*e.g.* figure 2.11). The index of the powerlaw is very flat, so most of the energy in the spectrum is contained in

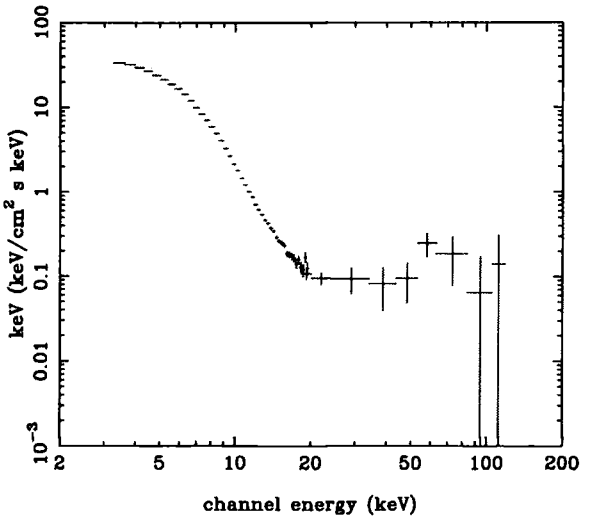

Figure 2.12: This spectrum shows the classic high state. There is large soft X–ray flux and very little (in some sources no) hard X–ray photons. The spectrum is taken from the 1998 outburst of J1550–564.

the highest energy photons. This state is most often associated with strong Comptonization of a low luminosity and low temperature disk by extremely hot electrons. It is commonly seen at the tail end of outbursts, when the disk is returning to its quiescent geometry. It has also been seen at the very beginning of the rise phase, again associating it with quiescence. Although a few steady state sources (Cyg X–1 and LMCX–1) exhibit this state it is normally associated with transient sources. In those steady source cases it is caused by the system being stable, but on the border of the state change mechanism so it manifests state transitions without being truly transient (Gierliński et al. 1999).

The high/soft state is more often associated with high luminosities seen in the middle stages of the outburst cycle (Nowak 1995). Its most notable feature is the enormous thermal spectrum, emitted by the disk. Although hard X–ray emission is sometimes noted, this is not always the case (see figure 2.12). It is perfectly feasible that the rate of heating in the hot electron region does not change between the low/hard state and the high state. Instead, the rate of cooling is hugely increased by the large number of photons from the disk. The sudden loss of hot electrons would severely dampen the high energy tail (Poutanen & Coppi 1998).

At the highest luminosities, which occur near the peak of the outburst cycle, the very high state appears. Again there is enormous emission from the disk, which is

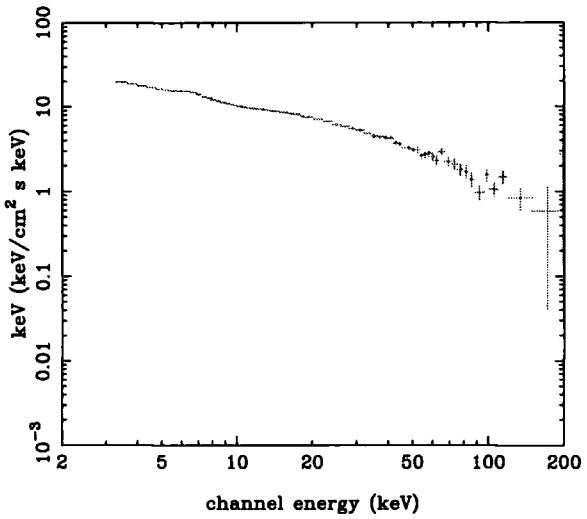

Figure 2.13: This spectrum shows the very high state where there is large soft X–ray flux and a very visible, steep hard X–ray tail. The spectrum is taken from the 1998 outburst of J1550–564.

to be expected if the disk is now in the Shakura–Sunyaev formation. There is also an equally enormous powerlaw tail which must come from a Comptonizing region. This tail slopes downwards showing that the spectrum is still intrinsically soft (*e.g.* figure 2.13).

Disks move from one state to the next during the outburst cycle. The low/hard state is seen only at low luminosities. Sources do sometimes complete an outburst without moving out of the low/hard state but they tend to have low maximum flux. Generally, there is only a limited correlation between the spectral states and luminosity (Nowak 1995; Done & Gierliński 2003). The nature of the state change mechanism is not known. A change in relative energy dissipation between optically thin and thick regions or the collapse of an inner hot flow have both been suggested (Esin et al. 1997). The second of these suggestions is the more convincing as it contains an automatic state change mechanism which results from the structure of the accretion flow itself.

2.5 Models of hot electron regions

It is possible to infer some properties of the hot electron region from observations of reflection and state change in transient X–ray binaries. These properties can be used

to differentiate between the coronal and inner hot flow models suggested earlier. In the first model, the disk extends all the way to the last stable orbit. Above it, the plasma attenuates into a corona which (being optically thin) maintains a very high temperature (Galeev, Rosner & Vaiana 1979). Some photons from the disk have to travel through this cloud to escape the system and so will be Comptonized. Reprocessing rules out a model in which the corona covers the *whole* disk on the grounds that the level of feedback from the disk would raise the amount of cooling to unacceptable levels. In such a situation around half the energy dissipated in the corona would be reprocessed by the disk, so a spectral index of around 2 would be expected (Haardt & Maraschi 1991, 1993). The spectra (for example in Cygnus X–1) are not compatible with such a situation as they show hard spectra and imply that the seed photons from the disk have only $\sim 10\%$ of the luminosity of the corona (Pietrini & Krolik 1995; Poutanen et al. 1997; Gierliński et al. 1997). Instead, the corona may be associated with individual magnetic flares on the surface of the disk (an outcome of the Balbus–Hawley mechanism). These flares are limited in space and so only a small amount of the photon flux from the disk passes through the Comptonizing regions (Stern et al. 1995b).

In the alternative models, the disk has a hole in the centre containing some form of inner, hot flow (which act as the Comptonizing environment). The optically thin flows naturally have high enough temperatures to cause the observed energy boost. Also, these clouds take up a limited region of space, so a relatively small number of the photons from the disk will pass through the Comptonizing region, avoiding the problem of excessive feedback.

Mechanisms of heating the electrons in these clouds (whatever their location) could be deduced by determining whether the electron energy distribution is thermal or non–thermal. The high energy roll–over in low state spectra implies a quasi–thermal distribution with a maximum temperature of approximately $100-200$ keV, although any non–thermal distribution with the same mean energy can mimic this effect (Ghisellini, Haardt & Fabian 1993). These temperatures are easily reached by the electrons in ADAFs or SLEs or with electrons associated with magnetic flares (as in the disk corona model; di Matteo 1998).

The observed spectrum in the very high state provides good evidence for the

existence of magnetic flare heating. At such high mass accretion rates, any optically thin inner flow *must* have collapsed, yet hard X–rays are still seen. There has to be a region of Comptonization and flares provide the only convincing model. Recent observations at very high energies show that there is an underlying non–thermal component to the hard X–ray tail in some spectra (Grove et al. 1998; Gierliński et al. 1999; Wilson & Done 2001; Zdziarski et al. 2002). This could be caused either by a separate region of non–thermal electrons or a mixed (thermal/non–thermal) plasma (Poutanen & Coppi 1998; Coppi 2000).

2.6 Summary

Observations of the timing and spectral properties of compact objects show several features which could be used to investigate the nature of accretion. Although theories of QPO formation remain sketchy they are consistent with a change in inner disk radius as an outburst progresses. Similarly, changes in spectral state are difficult to fully explain but tie in well with models of a truncated disk with an inner, hot flow.

The presence of hard X–rays in the spectra of accretion disks opens a whole new region of theoretical interest. The shape of the Compton scattered spectrum can provide information about the geometry of the disk and its local environment. The hard X–rays also give rise to disk reprocessing which is one of the most productive methods of observational analysis. The sensitivity of reflection to disk geometry and temperature could give a very accurate method of judging those parameters if the theoretical principles of continuum formation could be solved. As the technology of X–ray telescopes improves, reflection and disk reprocessing should pave the way for a better theoretical understanding of accretion.

Chapter 3

X–ray Observations of RXTE J1550-564

3.1 Methods of observation with relation to J1550–564

Observing disks in the rise phase has only recently become possible due to the rapid response of the RXTE satellite. RXTE J1550–564 is the first GBHC to be intensively observed during its rise and decline phases, giving unprecedented coverage of the X–ray spectrum over a huge range in mass accretion rate. These data give several ways to observationally track the disk. Firstly there are the Quasi–Periodic Oscillations (QPO's) seen in the X–ray spectra. While the origin of these are not well understood, *all* QPO models use a characteristic radius (this radius is a local change in disk properties and is sometimes associated with the inner edge of an SS disk, *e.g.* Psaltis & Norman 2003). For the QPO frequency to change then requires that this radius is *not* fixed at the last stable orbit of $6R_{\rm g}$ (where $R_{\rm g} = GM/c^2$). As its luminosity increases, RXTE J1550–564 shows a dramatic increase in QPO frequency by a factor of $\sim$ 50 (Cui et al. 1999; Remillard et al. 1999). This most probably indicates that the transition radius (or SS disk radius) is moving inwards (di Matteo & Psaltis 1999). Diskoseismology puts forward a model where QPO frequencies change because of a change in density during an outburst rather than because the disk radius is moving. However, these models can only generate small changes of frequency which are not compatible with the data from J1550–564 (Nowak et al. 1997; Wagoner, Silbergleit & Ortega–Rodrígues 2001).

A second way to track the inner disk is to use X–ray reflection. Hard X–rays illuminating optically thick material give rise to a Compton reflection component

and associated iron fluorescence line (Lightman & White 1988; George & Fabian 1991; Matt, Perola & Piro 1991). These features are smeared by special and general relativistic effects of the motion of the disk in the deep gravitational potential well (Fabian et al. 1989). The amount of reflection is a function of the solid angle of the optically thick disk as observed from the hard X–ray source, while the amount of smearing shows how far the material extends into the gravitational potential of the black hole.

In quiescence and the low state (LS) there are two potential mechanisms for producing hard X–rays. One of these has a truncated disk, and an optically thin, hot flow, while the other has a steady state or quiescent disk which extends down to the last stable orbit. If there is a truncated disk in quiescence/LS, then the disk material has to *move* in order to produce the high state (HS) and very high state (VHS) spectra which are dominated by emission from an optically thick, inner disk. In this chapter we attempt to use data from the rise to outburst of a GBHC transient as a diagnostic of the nature of the accretion flow since the majority of the disk material is *known* to be moving inwards in this phase. We expect the reflected fraction to increase to unity if the disk starts with a hole in the centre. If there is no hole we would expect the reflected fraction to start at 1 and remain there throughout the outburst.

In an effort to establish the reflected fraction, we analyze the detailed spectral properties during the rise phase. The 3-200 keV spectral changes during this time are shown in Figure 3.1. The 2–20 keV spectrum showed a dramatic softening during the rise (See also the lightcurve and hardness ratio plots in Sobczak et al. 1999), concurrent with the increasing QPO and break frequencies in the variability power spectrum (Cui et al. 1999). Taken together, these imply a LS–VHS state transition during the rise. The PCA and HEXTE spectra show that the broadband continuum is indeed consistent with a LS–VHS transition. We also identify a smeared reflected component in all the spectra. For the LS, the reflection signature is similar to that seen in other LS spectra, *i.e.* reflection from mainly neutral material, which subtends a solid angle of substantially less than 2π and is broadened, but not by as much as expected if the reflecting material extends to the last stable orbit (Gierliński et al. 1997; Życki, Done & Smith 1997; Done & Życki 1999; Gilfanov, Churazov

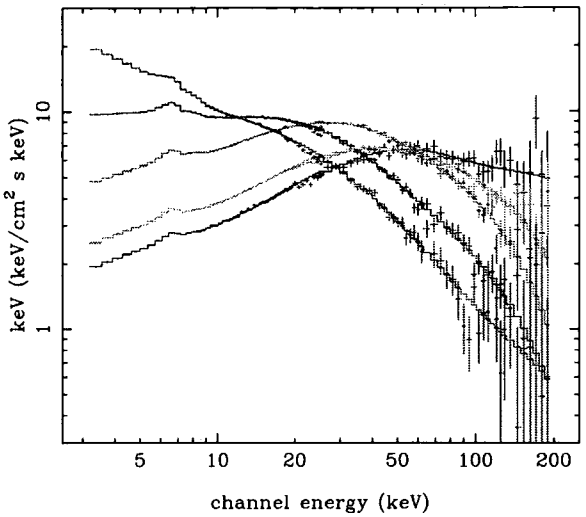

Figure 3.1: The spectral transition of XTE J1550–564 from low/hard to very high state. It should be noted that this transition, which takes place over the space of nine days is very smooth and shows no sign of a classic high state.

& Revnivtsev 1999; Zdziarski, Lubiński & Smith 1999). Both the disk instability model and QPO data imply a truncated SS disk at this point. This strongly favours models which identify the LS with a truncated disk, and rules out models which *require* an inner disk (of the Shakura and Sunyaev form).

Unfortunately, the reflected fraction remains significantly less than unity all the way through our data set showing that *neither* of our standard models are able to fit the data. We then attempt to identify the reasons that our original models are incorrect and how these problems can be overcome in future work.

3.2 The data from the rise to outburst of J1550–564

Calibration issues are important in any detailed spectral analysis. We have attempted to quantify these by analyzing a Crab spectrum taken contemporaneously with the RXTE J1550–564 rise data. The Crab spectrum is complex, since it contains both the nebula and pulsar components. The synchrotron nebula gives a spectrum which is approximately a power law ($\Gamma = 2.3$) in the 3–20 keV band, although there is subtle spectral curvature over a wider bandpass (*e.g.* Atoyan &

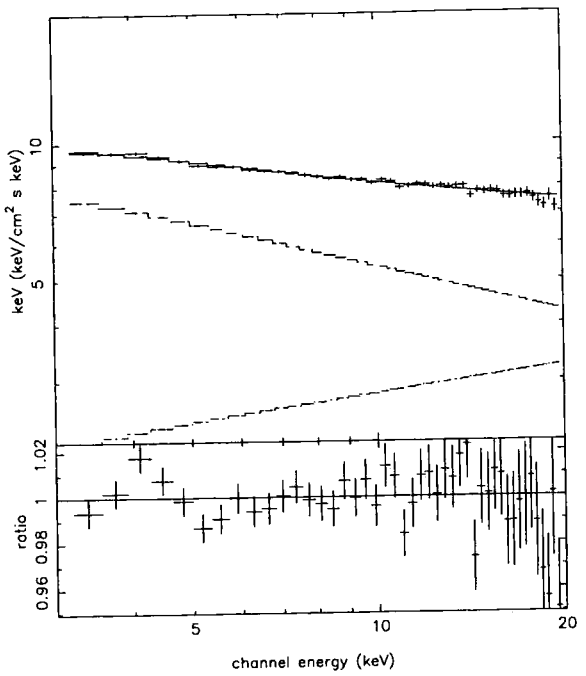

Figure 3.2: The PCA spectrum of the crab nebula taken concurrently with our data. The top panel shows the data fit with two powerlaws and a warm absorber. The lower panel shows the residuals from that fit.

Aharonian 1996; Pravdo, Angelini & Harding 1997; Massaro et al. 2000 and references therein). The pulsar spectrum is generically harder but has stronger curvature and is phase variable. It is consequently only approximately a power law over a rather restricted energy band. We approximate the total spectrum in the 3–20 keV range by two power laws, representing the nebula and pulsar, respectively. We fix the pulsar component to a spectral index of $\Gamma = 1.8$ and its flux at 10–20 % of that of the nebula, and obtain a good fit ($\chi^2_\nu = 46.2/42$) using only the top layers from detectors 0 and 1, with 0.5% systematic errors. Figure 3.2 shows the PCA spectrum of the crab nebula taken concurrently with our data. The top panel shows the model described above fit to the data (with absorption) and the lower panel shows the residuals from that fit.

Given the complex nature of the total emission from the Crab, the HEXTE data should not lie on a single power law extrapolation of the PCA. The data from HEXTE overlaps the data from OSSE when the two are compared (Gierliński et al. 1999). While work on the cross–calibration is still ongoing, there is currently no reason not to fit the two datasets together, allowing for a normalization offset.

This is an important point, since this 'discrepancy' has been used to argue that the PCA–HEXTE cross–calibration is unreliable (Sobczak et al. 1999).

We have used the public RXTE dataset 30188-06, which traces the rise of the outburst from 07/09/1998 to the 16/09/1998. The PCA (detectors 0,1 top layer only) and HEXTE (detector 0 only) data were extracted using the REX script in FTOOLS 5.0. Systematic errors of 0.5% were added to all the PCA spectra. Selected spectra from the rise of J1550–564 are shown in Figure 3.1, showing the dramatic spectral softening. Although the 2-10 keV lightcurve of the ASM shows a spectacular increase in luminosity (a factor of ~ 7), figure 3.1 shows that this is a bandpass effect caused by ignoring the higher energies. The estimated bolometric luminosity only increases by a factor of ~ 2.

3.3 Description of the model used

We analyzed the spectra using the XSPEC spectral fitting package (Arnaud 1996) v10.0. The spectrum is expected to contain soft emission from the accretion disk (approximated here by the `diskbb` model) and hard emission from Compton scattering of these soft seed photons by energetic electrons. A power law with exponential roll–over at the electron energy is often used to approximate this, but it seriously overestimates the Comptonized flux at energies close to those of the seed photons, and underestimates it at high energies (Zdziarski et al. 2002). This renders most parameters derived from such models unreliable. Instead we use an approximate solution for thermal Comptonization based on Kompaneets' equation (`thComp`: Zdziarski et al. 1996). The Kompaneets' equation represents Compton scattering as a diffusion through energy and position. A diffusion approximation relies on the energy not changing much at each scattering and the system having a high optical depth. Consequently this solution becomes inaccurate at optical depths < 1 and temperatures above > 100 keV.

The Comptonized spectrum can illuminate the accretion disk, giving rise to a reflected component. Both the continuum reflection (Magdziarz & Zdziarski 1995) and iron emission line are calculated self consistently for a given ionization state (Życki & Czerny 1994), and the total reprocessed spectrum is relativistically

smeared by convolving it with the `diskline` model of Fabian et al. (1989) including corrections for light bending. The reflected spectrum is then determined from a number of free parameters. The amount of reflection is parameterized by the solid angle of the reflector, as seen from the X–ray source, Ω. This is normalized to 2π so that when $\Omega/2\pi = 1$ the X–rays are reflected from half the sky. Other input parameters are its inclination i, ionization parameter, $\xi = 4\pi F_X/n$ (where F_X is the illuminating flux and n = number density), and inner disk radius, $R_{\rm in}$ (see Życki ,Done and Smith 1999 for model details). The abundances of Morrison & McCammon (1983) are used.

When this data was analysed there was no good determination of the inclination of the system, so we fixed this at 30°. The distance was also fairly uncertain, but E(B–V)$\sim$ 0.7 measured from optical spectra suggests 2.5 kpc (Sanchez–Fernandez et al. 1999). This E(B–V) predicts a column density of $\sim 4 \times 10^{21}{\rm cm}^{-2}$, consistent with the column we measure from fitting the publicly available archived ASCA GIS data (sequence ID 15606000 taken on 12/09/98). We fix the column to this value in all the fits, and note that the much larger column of $\sim 2 \times 10^{22}{\rm cm}^{-2}$ inferred by Sobczak et al. (1999) is an artifact of their more approximate spectral model. More recent optical work has posited an inclination of $\sim 70°$ (Orosz et al. 2002). We have re–fit the data using the higher inclination. In the LS spectra the derived $\Omega/2\pi$ changes by $\sim$ 0.1. However, in the softer spectra (found at higher luminosities) modelling a reflected spectrum of any sort becomes difficult.

Different attempts to model the same spectra can often generate very different results. As stated in chapter 2, a generic spectrum can be broken down into various components which can be modelled separately. The commonly used phenomenological method, models the continuum spectrum as a low energy black body or `diskbb` together with an exponentially cut–off powerlaw. Reflection is represented by a Gaussian iron line. This produces excellent fits but suffers from a lack of physicality. There is no physical limit on where the Compton tail gets its seed photons or how much reflection there can be. Consequently, parameters derived from such spectra are suspect (see figure 3.3 for an example of this problem). The figure shows a comparison of a thermal Comptonization model with a powerlaw and exponential cut–off. Clearly the exponential roll–over starts too early and is

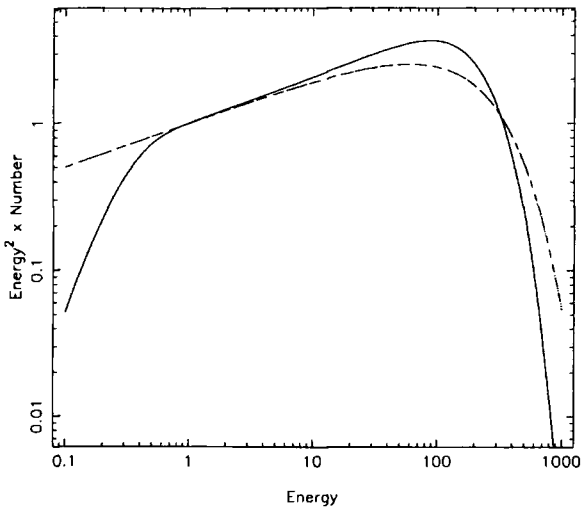

Figure 3.3: This figure shows a comparison of a thermal Comptonization model with a powerlaw and exponential cut–off. Clearly the exponential roll–over starts too early and is too shallow in comparison to the thermal roll–over which begins at approximately 100 keV. The powerlaw also overestimates the number of photons in the low energy region as it does not account for the temperature of the seed photons.

too shallow in comparison to the thermal roll–over which begins at approximately 100 keV. The powerlaw also overestimates the number of photons in the low energy region as it does not account for the seed photons being a black body with a specific temperature.

3.4 Results of fitting the data

3.4.1 The initial spectrum

The PCA data alone cannot be well fit by a thermal Comptonization continuum and disk blackbody spectrum ($\chi^2_\nu = 304.3/40$). Including a reflected spectrum and its associated iron fluorescence line gives a good fit to the data ($\chi^2_\nu = 43.0/38$), but this is further *significantly* improved by including relativistic smearing ($\chi^2_\nu = 37.1/37$, for $R_{in} = 26^{+63}_{-15}\, R_g$). The reflected fraction is $\Omega/2\pi = 0.24^{+0.03}_{-0.04}$ from mainly neutral material ($\xi = 16^{+23}_{-5}\,\mathrm{ergss^{-1}cm}$). The disk blackbody is *not* significantly detected in the spectrum, and assuming that it provides the soft photons for the thermal Comptonization gives a limit on its temperature of ≤ 0.5 keV).

These findings are qualitatively different to those derived from using more approximate spectral models. The often used continuum of a disk blackbody and power law, together with a broad Gaussian line and smeared edge to phenomenologically model the reflected spectral features (as used for later parts of the outburst in Sobczak et al. 1999) gives a comparably good fit if the column is allowed to be free ($\chi^2_\nu = 26.0/36$). With this model the disk blackbody is *required*, and has $kT = 0.75^{+0.12}_{-0.11}$ keV (which seems unusually high for a low state spectrum). We strongly caution against using parameters derived from such phenomenological fits to derive physical quantities such as disk radii (see also the detailed criticism of the `diskbb` model of Merloni, Fabian & Ross 2000).

The model is further constrained if the HEXTE data (30–200 keV) is used as the electron temperature can be determined from the high energy roll–over in the spectrum. A single thermal Comptonization model (with its relativistic reflection) can fit both PCA and HEXTE data ($\chi^2_\nu = 71.5/75$), as shown in the upper panel of figure 3.4. The reflection parameters remain similar to those derived from the PCA data alone, $R_{in} = 26^{+48}_{-14}\,R_g$, $\Omega/2\pi = 0.25^{+0.04}_{-0.03}$ and $\xi = 14^{+26}_{-8}\,\mathrm{ergss^{-1}cm}$. However, the broad bandpass covered also shows evidence for subtle spectral curvature which can be modelled by including a second Comptonized component. This gives a significantly better fit and is shown in the lower panel ($\chi^2_\nu = 51.5/72$) but for rather different reflection parameters ($\Omega/2\pi = 0.08^{+0.05}_{-0.05}$, $\xi = 350^{+9000}_{-280}\,\mathrm{ergss^{-1}cm}$ and $R_{in} = 20^{+31}_{-10}\,R_g$). The second Compton component has a shape which is clearly rather similar to a reflection hump, so if this is the shape of the continuum then it significantly reduces the derived reflected fraction.

While this spectral curvature is significantly detected it does not necessarily mean that the continuum is truly described by a two (or multi) temperature form. Firstly, it could be an artifact of residual cross–calibration uncertainties between the PCA and HEXTE instruments (although this is unlikely given the correspondence between HEXTE and OSSE). However, spectral curvature is marginally detected in the PCA data alone: including a second Comptonized component (with its reflection tied to that of the first Comptonized spectrum) gives a reduction in χ^2_ν to 27.3/34. It could also indicate that the reflected spectral models used here underestimate the Compton reflection hump, such as might be expected if there was

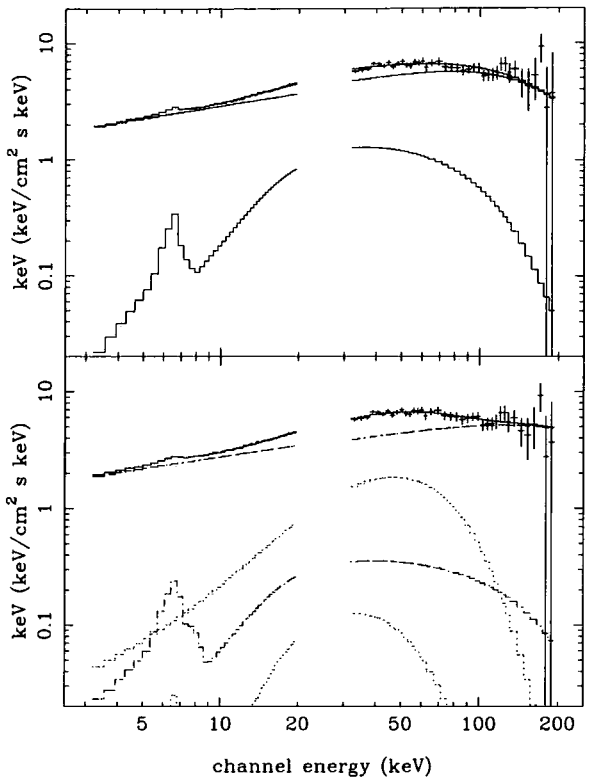

Figure 3.4: These panels show the first spectrum of the data set fit with (top panel) one and (bottom panel) two thermal Comptonized continua. The individual reflection components have also been included.

an ionized skin overlying a neutral disk that produced Compton reflection but no spectral features (Nayakshin, Kazanas & Kallman 2000; Done & Nayakshin 2001). Alternatively there can be complex curvature in a Comptonized spectrum due to the visibility of the individual scattering orders (*e.g.* Pozdnyakov, Sobol & Sunyaev 1983), which are not included in our approximate `thComp` model. As a test, we use a numerical solution of the Comptonization equations for optically thin material and its reflection (`CompPS`: Poutanen & Svensson 1996). This does not include the self consistent line emission for the reflection spectrum, so the line is included as a `diskline` with free energy and normalisation. This results in $\chi^2_\nu = 60.1/73$, with $\Omega/2\pi = 0.26$ and $\xi = 62\,\mathrm{ergss^{-1}cm}$ (*i.e.* similar reflected parameters and χ^2_ν to the single Compton component model).

The initial spectrum is very similar to the classic Low State spectra seen in many Galactic Black Holes (little or no thermal emission and a large Compton component). The power spectrum of these data shown by Cui et al. (1999) is also

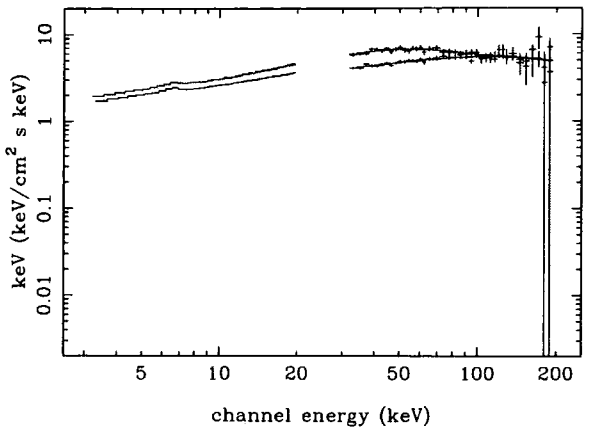

Figure 3.5: The spectra of J1550–564 in the low/hard state (above) overlaid with the hardest detected state of Cygnus X-1 (below). The spectra are clearly similar showing that J1550 started the outburst in the low/hard state.

very similar to low/hard state power spectra (*e.g.* van der Klis 1995), being flat below ~ 0.1 Hz, breaking to $\sim f^{-1}$, and then to $\sim f^{-2}$ above ~ 10 Hz, with a high r.m.s. amplitude of $\sim 30\%$. Comparing these with the compilation of RXTE Cyg X–1 data of Gilfanov et al. (1999) shows that both spectrum and variability are typical of Cyg X–1 in its *hardest* low/hard state as observed by RXTE.

We illustrate this spectrally by showing the hardest low/hard spectrum of the RXTE Cyg X–1 observation (10238-01-03-00), extracted identically to the J1550–564 data. We fit this to the same spectral model of a disk black body and two Comptonized continua (together with their reflected emission). This gives an excellent fit, with $\chi^2_\nu = 74.6/72$. Figure 3.5 shows this with the data from RXTE J1550–564 over-plotted. Again, the spectrum is slightly curved: a single `thComp` Compton continuum and its reflection gives a significantly worse fit ($\chi^2_\nu = 88.9/75$), although again this could be due to the same cross-calibration uncertainties rather than necessarily pointing to a more complex continuum or reflected spectrum. We conclude that in the first part of the rise then RXTE J1550–564 was in a classic LS.

3.4.2 The final spectrum

The model which provided an acceptable fit to the LS PCA data (disk blackbody as seed photons for thermal Comptonization and its reflected spectrum with relativistic

smearing) also gives an adequate fit to the final spectrum ($\chi^2_\nu = 44.4/37$) but with very different parameters. The disk blackbody is now significantly detected, with $kT \sim 0.7$ keV, and there is significant spectral curvature in the PCA spectrum which causes the derived electron temperature to be ~ 19 keV, much lower than the LS. The ionization state of the reflector is now extremely high, $\xi \sim (3 \times 10^3)\,\mathrm{ergss^{-1}cm}$. The phenomenological model (a disk black body and powerlaw) gives a statistically similar fit, $\chi^2_\nu = 43.1/36$, with seed photon temperature $kT \sim 0.6$ keV. Including the HEXTE data results in a χ^2_ν of 328.0/74 although this drops to $\chi^2_\nu = 70.4/72$ with an exponential roll–over in the continuum.

The single Comptonized component (modelled with `thComp` and its reflection (with a disk blackbody from the accretion disk) can fit the PCA and HEXTE data adequately ($\chi^2_\nu = 89.1/75$), with $\Omega/2\pi = 0.11^{+0.02}_{-0.02}$, $\xi = (2.6 \times 10^3)^{+3500}_{-1300}\,\mathrm{ergss^{-1}cm}$ and $R_{in} = 15^{+20}_{-8}\,R_\mathrm{g}$. Once again there are hints of spectral curvature. Using a second Compton component again gives a (marginally significantly) better fit ($\chi^2_\nu = 79.43/72$) which is shown in Figure 3.6. However, this time the reflection parameters are robust to changes in the spectral form, with $\Omega/2\pi = 0.12^{+0.015}_{-0.01}$, $\xi = (2.5 \times 10^3)^{+3500}_{-1390}\,\mathrm{ergss^{-1}cm}$ and $R_{in} = 18^{+13}_{-7.5}\,R_\mathrm{g}$ for the two `thComp` continuum, and $\Omega/2\pi = 0.15$, $\xi = (8.2 \times 10^3)\,\mathrm{ergss^{-1}cm}$ and $R_{in} = 13\,R_\mathrm{g}$ for a single `CompPS` continuum.

The two temperature model continuum gives a combination of low energy curvature with a high energy tail which is very similar to that seen in Cyg X–1 in its high state (Poutanen & Coppi 1998; Coppi 1999; Gierliński et al. 1999), the difference here being that low temperature Comptonized emission is much stronger in RXTE J1550–564 (thus making the disk emission less obviously dominant) than in the HS of Cyg X–1. This, together with its power spectrum (Cui et al. 1999) clearly shows that by the end of slow rise RXTE J1550–564 is in the very high state. The classic high/soft state (defined as that which contains a dominant black body spectrum and little or no Comptonized component) is *never* encountered during the rise, and the spectral transition is from LS to VHS.

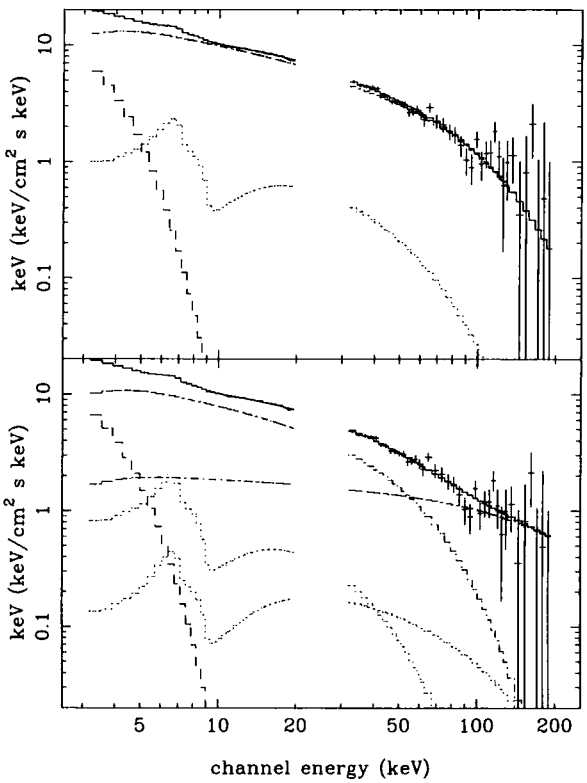

Figure 3.6: These panels show the last spectrum of the data set fit with (top panel) one and (bottom panel) two thermal Comptonized continua. The individual reflection components have also been included.

3.4.3 The intermediate spectra

Any system of models must be able to fit *all* the data, so here we look at a spectrum taken from the middle of the rise (spectrum number 3), where the hardness ratio clearly indicates that the source is in transition. A single Compton component model using the PCA data alone gives $\chi^2_\nu = 27.0/37$ with $\Omega/2\pi = 0.07^{+0.01}_{-0.01}$, $\xi = (7 \times 10^3)^{+4700}_{-3750}$ ergss^{-1}cm, and $R_{in} = 45^{+115}_{-20}\, R_{\rm g}$, but including the HEXTE data gives 225.2/75, a completely inadequate fit. The curvature is *not* well modeled even by `CompPS` which gives $\chi^2_\nu = 129/73$. The two component Comptonization model is the only one which gives a good fit to the broad band data ($\chi^2_\nu = 66/75$), as shown in Figure 3.7. The reflection parameters are then similar to those derived from the PCA data alone with $\Omega/2\pi = 0.07^{+0.01}_{-0.007}$, $\xi = (7.1 \times 10^3)^{+4700}_{-2400}$ ergss^{-1}cm, and $R_{in} = 42^{+73}_{-19}\, R_{\rm g}$. The nature of the spectral curvature is not subtle, and the spectrum clearly shows that there is a low temperature, curving component in the PCA, together with rather higher temperature emission which dominates the HEXTE band. In the final spectrum the lower temperature component is somewhat hotter and dominates more of the high energy spectrum, making the single temperature models an adequate description.

3.4.4 Data from all spectra

The previous sections have shown that the parameters derived from reflection are not always robust to changing the continuum spectral form. Accordingly we give results for two sets of spectral fits. In the first we assume that the HEXTE cross–calibration is reliable and fit all the rise PCA/HEXTE spectra with a model consisting of seed disk blackbody photons, together with two thermal Compton continua and their relativistically smeared reflection (Table 3.1). The last column of Table 3.1 gives the χ^2_ν for a single Compton continuum model fit to the PCA/HEXTE data, showing that it cannot acceptably fit most of the intermediate spectra (see previous section). The second set of fits assumes that the HEXTE cross–calibration is not reliable at this level and so uses only the PCA data with a model of seed disk blackbody photons, a single temperature thermal Compton continuum and its relativistically smeared reflection (Table 3.2). Given the uncertainty on the contin-

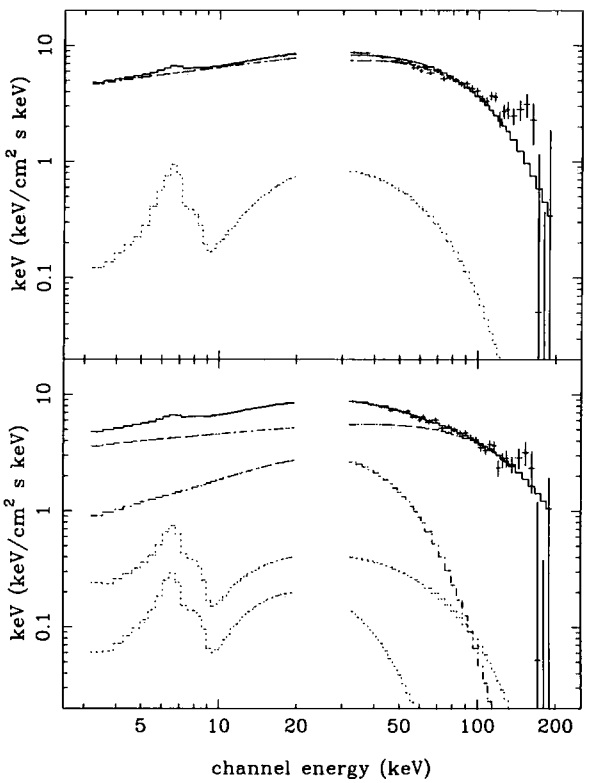

Figure 3.7: These panels show the third spectrum of the data set fit with (top panel) one and (bottom panel) two thermal Comptonized continua. The individual reflection components have also been included.

uum model (and the fact that the temperatures derived from `thComp` are inaccurate above $\sim$ 50 keV) we show spectral evolution by the changing hardness ratio of the PCA data.

The evolution of the reflector parameters during the rise is shown in Figure 3.8. Irrespective of the continuum model used, the derived amount of reflection is always significantly less than unity. The amount of relativistic smearing (while always significant although with large error bars) is *never* as large as that expected for a disk extending down to the last stable orbit in a Schwarzschild geometry.

If the single Comptonized component is the correct model for the hard spectrum in the low state, there is a sharp increase in ionization state, coupled with a decrease in the amount of reflection at the onset of the spectral state transition. In the two component Comptonization model then there are hints of the same effect, although it is less significant due to the larger error bars on the derived ionization state.

For the single temperature continuum fits to the PCA data the onset of the LS–VHS transition is marked by an increase in ionization state of the reflector from $\sim$ 20 to $\sim$ 5000/, ergss^{-1}cm and a decrease in the solid angle subtended by the disk, from $\Omega/2\pi \sim 0.25 - 0.12$. Apart from this jump at spectrum 3 the parameters are remarkably stable throughout large changes in spectral form. This stability is even more marked in the two temperature PCA/HEXTE fits (see figure 3.8). There is some indication of a jump in ionization at the onset of the LS–VHS transition, though it is less significant due to the larger error bars on the reflection parameters from the LS data. However, there is no evidence for any change in the solid angle.

It should be noted that ionization and the amount of reflection are correlated in the fits. As the ionization increases the photoelectric opacity decreases, so there is more reflected continuum below $\sim$ 15 keV. The spectral features (line and edge) shift to higher energies, and their contrast with respect to the continuum increases (although this also depends on the hardness of the illuminating continuum). In general the line increases by more than the edge as the fluorescence yield increases with ionization state (see *e.g.* Ross & Fabian 1993; Życki & Czerny 1994 for photo–ionized reflected spectra). Figure 3.9 shows the residuals to the best fit continuum only model (disk blackbody and single thermal Compton spectrum but no reflection) to the data before and after the transition (PCA spectra 1 and 5). There is clearly

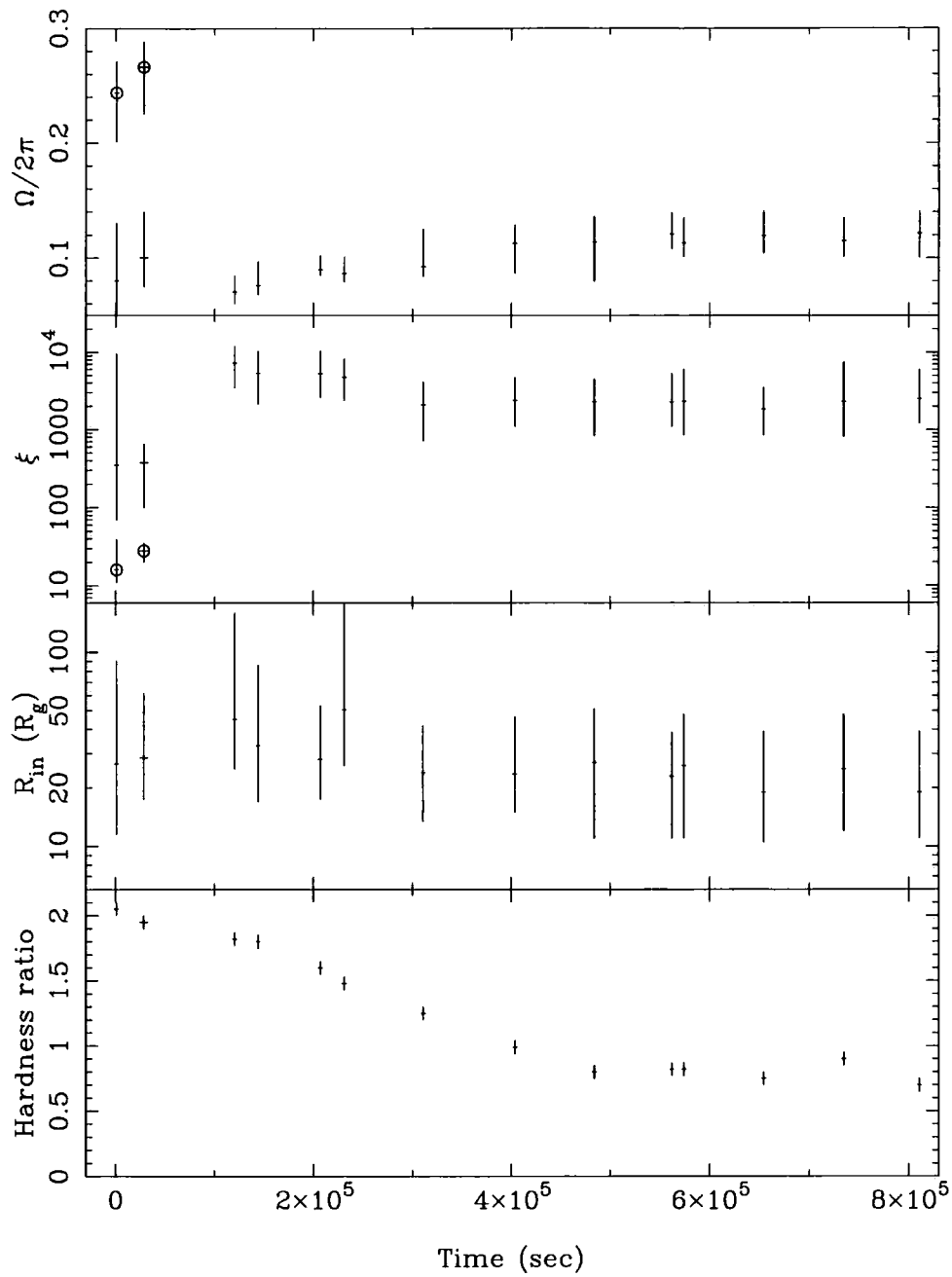

Figure 3.8: The change in fit parameters during the first nine days of the outburst of J1550–564. The spectral transition is represented as a change in hardness ratio (bottom graph). Also included are the changes in covering fraction, ionization state and disk inner radius. The points with circles shown in the top panel ($\Omega/2\pi$) and second panel (ξ) are the parameters which result from a fit with one Comptonized spectrum rather than two.

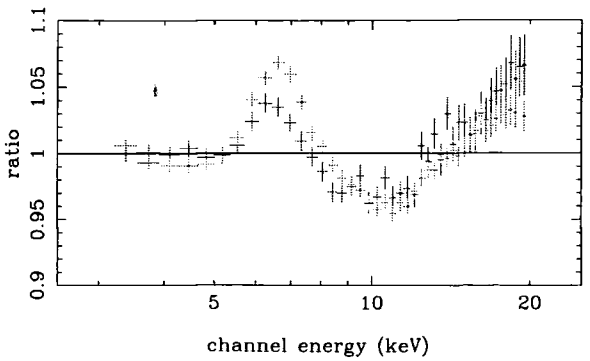

Figure 3.9: The residuals to a continuum only model fit to data before (first spectrum) and after (fifth spectrum) the shift in reflection parameters. Plainly the line and edge energy increase, but only the line increases in strength, while the edge depth and Compton hump stay approximately constant.

more line and its mean energy has shifted up, indicating ionization. The edge energy has also increased, but its strength has not. While ionization predicts that the line should increase by more than the edge, the edge depth should also increase if the solid angle remains the same. So to get increasing ionization with the same edge depth requires that the solid angle decreases.

3.5 Models of the low state during the outburst

As has been mentioned in chapter 1, there are two main theories for how the LS spectrum is formed. The first is that the accretion disk truncates, forming an inner, optically thin, X–ray hot accretion flow, while the second postulates magnetic flares above a disk. We review here the very different predictions of these models for how the X–ray emitting region evolves during the rise to outburst, but show that both can give the observed initial (LS) spectrum.

3.5.1 Truncated disk with an inner, X–ray hot flow

The geometry of a truncated disk and inner, X–ray hot flow can explain the weak disk emission, hard (photon–starved) X–ray spectrum, and generally low amplitude of X–ray reflection seen in the LS (*e.g.* Poutanen, Krolik & Ryde 1997). Certainly in quiescence it seems very likely that the disk structure does not extend all the

Table 3.1: The table shows the reflection parameters for the PCA and HEXTE data using a model of a disk black body with two Comptonized reflectors. The χ^2_ν values for a single Compton reflector are also included. Errors are calculated for $\Delta\chi^2 = 2.7$

Spectrum number	$\Omega/2\pi$ [a]	ξ [b]	Inner radius [c]	hardness ratio [d]	$\chi^{2\,e}_\nu$	$\chi^{2\,f}_\nu$
1	$0.08^{+0.05}_{-0.05}$	350^{+9150}_{-280}	20^{+31}_{-10}	$2.05^{+0.05}_{-0.05}$	51/72	72/75
2	$0.10^{+0.04}_{-0.025}$	375^{+275}_{-275}	$21.5^{+23.5}_{-8.5}$	$1.95^{+0.05}_{-0.05}$	65/72	104/75
3	$0.07^{+0.01}_{-0.006}$	5100^{+4700}_{-2400}	42^{+73}_{-19}	$1.85^{+0.05}_{-0.05}$	66/72	225/75
4	$0.08^{+0.01}_{-0.007}$	4800^{+4220}_{-3280}	30.5^{+52}_{-13}	$1.82^{+0.03}_{-0.03}$	59/72	147/75
5	$0.09^{+0.01}_{-0.006}$	4480^{+3920}_{-2280}	28^{+23}_{-12}	$1.60^{+0.05}_{-0.05}$	59/72	192/75
6	$0.08^{+0.01}_{-0.009}$	3865^{+3135}_{-1965}	49^{+226}_{-23}	$1.50^{+0.03}_{-0.03}$	62/72	165/75
7	$0.10^{+0.02}_{-0.008}$	2230^{+1470}_{-1430}	$24^{+18}_{-9.5}$	$1.25^{+0.025}_{-0.025}$	63/72	166/75
8	$0.11^{+0.01}_{-0.01}$	2190^{+1800}_{-1100}	26^{+23}_{-10}	$1.00^{+0.03}_{-0.03}$	91/72	168/75
9	$0.12^{+0.02}_{-0.01}$	2375^{+1525}_{-1480}	19^{+11}_{-6}	$0.85^{+0.01}_{-0.01}$	69/72	118/75
10	$0.12^{+0.02}_{-0.01}$	2450^{+2550}_{-1450}	$17.5^{+12.5}_{-7}$	$0.87^{+0.015}_{-0.015}$	58/72	90/75
11	$0.12^{+0.015}_{-0.01}$	2520^{+1680}_{-2040}	$18^{+15}_{-5.5}$	$0.87^{+0.01}_{-0.01}$	81/72	117/75
12	$0.12^{+0.03}_{-0.01}$	2200^{+1400}_{-1600}	$17^{+11}_{-7.5}$	$0.77^{+0.015}_{-0.015}$	72/72	92/75
13	$0.12^{+0.02}_{-0.01}$	2400^{+3575}_{-1400}	$19.5^{+17.5}_{-7}$	$0.90^{+0.01}_{-0.01}$	68/72	94/75
14	$0.12^{+0.015}_{-0.01}$	2500^{+3500}_{-1390}	$18^{+13}_{-7.5}$	$0.75^{+0.01}_{-0.01}$	80/72	89/75

a Solid angle subtended by reflector

b Ionization parameter in ergss^{-1}cm

c Measured in gravitational radii, GM/c^2

d Ratio of 8-20keV and 1-5keV data

e For two Compton components

f For one Compton component

Table 3.2: The table shows the reflection parameters for the PCA data only, using a model of a disk black body with a single Comptonized reflector. Errors are calculated for $\Delta\chi^2 = 2.7$

Spectrum number	$\Omega/2\pi$ [a]	ξ [b]	Inner radius [c]	hardness ratio [d]	χ^{2e}_ν
1	$0.24^{+0.03}_{-0.04}$	16^{+23}_{-5}	$26.5^{+63.5}_{-15}$	$2.05^{+0.05}_{-0.05}$	37/37
2	$0.27^{+0.02}_{-0.04}$	28^{+7}_{-8}	28.5^{+33}_{-11}	$1.95^{+0.05}_{-0.05}$	44/37
3	$0.07^{+0.01}_{-0.01}$	7250^{+4700}_{-3750}	45^{115+}_{-20}	$1.85^{+0.05}_{-0.05}$	27/37
4	$0.08^{+0.02}_{-0.01}$	5345^{+5000}_{-3200}	33^{+53}_{-16}	$1.82^{+0.03}_{-0.03}$	22/37
5	$0.09^{+0.01}_{-0.01}$	5300^{+5000}_{-2700}	$28^{+25}_{-10.5}$	$1.60^{+0.05}_{-0.05}$	34/37
6	$0.09^{+0.01}_{-0.01}$	4750^{+3330}_{-2360}	$50.5^{+180}_{-24.5}$	$1.50^{+0.03}_{-0.03}$	30/37
7	$0.09^{+0.03}_{-0.01}$	2100^{+2000}_{-1380}	$24^{+18}_{-10.5}$	$1.25^{+0.025}_{-0.025}$	25/37
8	$0.11^{+0.01}_{-0.02}$	2380^{+2320}_{-1280}	$23.5^{+23}_{-8.5}$	$1.00^{+0.03}_{-0.03}$	41/37
9	$0.11^{+0.02}_{-0.03}$	2290^{+2200}_{-1540}	27^{+24}_{-16}	$0.85^{+0.01}_{-0.01}$	41/37
10	$0.12^{+0.02}_{-0.01}$	2280^{+3000}_{-1200}	$23^{+15.5}_{-12}$	$0.87^{+0.015}_{-0.015}$	37/37
11	$0.11^{+0.02}_{-0.01}$	2325^{+3675}_{-1475}	26^{+22}_{-15}	$0.87^{+0.01}_{-0.01}$	35/37
12	$0.12^{+0.02}_{-0.02}$	1850^{+1650}_{-1000}	$19^{+20}_{-8.5}$	$0.77^{+0.015}_{-0.015}$	36/37
13	$0.12^{+0.02}_{-0.01}$	2300^{+5200}_{-1500}	25^{+23}_{-13}	$0.90^{+0.01}_{-0.01}$	34/37
14	$0.12^{+0.02}_{-0.02}$	2500^{+3500}_{-1300}	19^{+20}_{-8}	$0.75^{+0.01}_{-0.01}$	44/37

a Solid angle subtended by reflector

b Ionization parameter in ergss^{-1}cm

c Measured in gravitational radii, GM/c^2

d Ratio of 8-20keV and 1-5keV data

e For one Compton component

way down to the last stable orbit. In chapter 1 we noted that the observed X–ray luminosities of quiescent objects, while low, still imply a mass accretion rate which is too high for the inner disk to remain below the instability threshold. A disk which truncates at larger radii can carry this mass accretion rate without triggering the instability (Lasota et al. 1996). However, the inner regions of a quiescent disk structure are generally optically thin to both true absorption and electron scattering (see *e.g.* Cannizzo 1998). Such material cannot cool efficiently, so will heat up. Conduction between this and the remaining quiescent disk can lead to progressive evaporation of the inner regions of the quiescent disk into a hot flow (Meyer & Meyer–Hofmeister 1994; Meyer–Hofmeister & Meyer 1999). Conduction from a hot flow can lead to evaporation of even an SS disk, so this can be a mechanism to truncate the disk even at the much higher mass accretion rates generally seen for the LS emission (Różańska & Czerny 2000).

When the instability is triggered in the outer quiescent disk, a large amount of mass flows towards the black hole, increasing the hot flow's density (and also its luminosity). However, at a certain critical mass accretion rate, the density is such that electron–ion collisions become frequent, so the electrons gain most of the ion energy. In the case of an ADAF, the advected fraction becomes small and the ADAF collapses into a standard SS disk (similar events will collapse an SLE solution). This predicts that the LS will end at accretion rates of $\dot{m} \sim 1.3\alpha^2$ (where $\dot{m} = \dot{M}/\dot{M}_{Edd}$, and $\dot{M}_{Edd} = 10L_{Edd}/c^2$). This corresponds to luminosities of $1 - 8\%$ of Eddington for a viscosity of $\alpha = 0.1 - 0.3$, as around a third of the energy is advected rather than radiated at these densities (Esin et al. 1997; Quataert & Narayan 1999).

These models predict $\Omega/2\pi < 1$ as the hot flow is centrally concentrated so the solid angle subtended by the disk is fairly small (Esin et al. 1997). However, more detailed predictions are difficult as they critically depend on the geometry at the transition between the disk and hot flow. Current ADAF models generally *assume* a transition radius of $\sim$ 1000 Schwarzschild radii, and these give LS spectra which have $\Omega/2\pi << 1$ (Esin et al. 1997) and very little relativistic smearing. Previous observations of 2–20 keV LS spectra show $\Omega/2\pi \sim 0.3$ (Gierliński et al. 1997; Życki et al. 1997; Życki Done & Smith 1998; Gilfanov et al. 1999), and smearing characteristic of an inner radius of 10–20 Schwarzschild radii (Życki et

al. 1997; 1998; 1999; Done & Życki 1999). These are incompatible with a disk truncated at 1000 Schwarzschild radii. By decreasing the transition radius between the ADAF and the cold disk the predicted solid angle and smearing can match the observations. However, this is not a completely free parameter. A small transition radius gives rise to a strong disk flux which Compton cools the ADAF, and can lead to its collapse (Esin 1997). A transition at 10 Schwarzschild radii decreases the maximum ADAF luminosity by a factor of ~ 2, making it only just feasible to get the observed LS luminosity of $\sim 3\%$ of Eddington (Esin et al. 1997; Gierliński et al. 1999). These problems disappear entirely if the PCA/HEXTE cross–calibration spectra is reliable. Continuum curvature can give an *overestimate* of the amount of reflection present in single temperature/power law fits to low energy (≤ 20 keV) spectra (compare Tables 3.1 and 3.2 for the LS spectra).

The inner radius of most of the disk material is almost certainly moving during the rise to outburst. If the edge of the ADAF follows the inner radius of the heating wave (*i.e.* the inner radius of the SS part of the disk), then the reflected fraction should be small and remain fairly constant. Alternatively, if the disk penetrates some way into the ADAF, $\Omega/2\pi$ is rather larger and can increase or remain constant as the heating wave moves inwards, depending on the details of the geometry. In both of these options the amount of relativistic smearing should increase as the radius decreases, but our data do not cover much of the LS evolution so we cannot tell.

While this gives continuity of properties between the quiescent and LS spectra, there should be an abrupt change when the ADAF finally collapses into whatever very different mechanism powers the LS/VHS emission. The viscous timescale for a quasi–spherical flow to collapse is only $\sim 1/\alpha$ times longer than the dynamical timescale at a given radius (*i.e.* much less than a second for a flow of $10R_s$ around a $10M_\odot$ black hole). However, the collapse might be triggered locally by the disk underneath the hot flow, in which case it will be determined by the viscous timescale for the SS disk, which is $\sim$ a few hours for the same parameters. This is still a much shorter than the observed ~ 3 day timescale for the spectral transition (see Figure 3.1), although evaporation of the disk material into the hot flow may slow this considerably (Różańska & Czerny 2000). Dubus, Hameury & Lasota (2001)

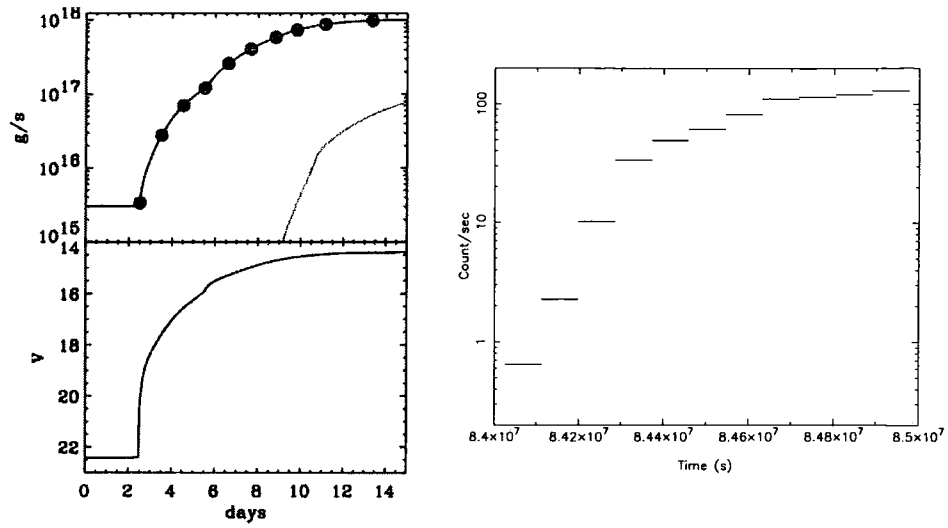

Figure 3.10: This shows the modelled rise phase of a disk including irradiation and evaporation. The upper left panel shows $\dot{m}_{in}$ and $\dot{m}_{irr}$ (dotted line); the bottom left panel shows the V magnitude. Taken from Dubus, Hameury & Lasota 2001. The right panel shows the ASM data of the first 11 days of the outburst of J1550–564. There is a clear similarity in fractional change and timescale.

have calculated models including evaporation and irradiation of the disk during the outburst rise. Encouragingly, when they include both of these effects on a model disk, the rise times are reminiscent of J1550–564. The timescale and magnitude of the predicted lightcurve matches very well with the lightcurve seen in J1550–564 (see figure 3.10 where the predicted changes in parameter are shown with the lightcurve from J1550–564).

3.5.2 Magnetic corona above an untruncated disk

In the second theory for the LS emission, some (large) fraction of the gravitational potential energy of the infalling material is released in an optically thin environment by magnetic reconnection above the dense disk material. In quiescence this can power the observed low level X–ray emission without triggering the instability as long as these are distributed over the whole disk (powered by the local $\dot{m}$ at a

given radius which is not constant) rather than requiring that the X–rays are produced solely by the central $\dot{m}$ (Nayakshin & Svensson 2001). However, numerical simulations imply that the Balbus–Hawley dynamo mechanism for the magnetic field shuts off when the disk material becomes mainly neutral and so has a large resistivity (Gammie & Menou 1998; Fleming, Stone & Hawley 2000). The quiescent disk is then unlikely to be able to power *any* magnetic reconnection, so the continuity of spectral properties from the LS to quiescence is hard to explain. Also, the inner quiescent disk is predicted to be optically thin to both absorption and scattering, so the caveats listed in the previous section still apply as to whether it can exist as a geometrically thin, cool disk.

Irrespective of whether this can produce the hard X–rays observed in quiescence, the X–ray emission from magnetic reconnection above the outbursting disk is likely to be dominant once the the instability is triggered since its local $\dot{m}$ will be so much larger. The heating wave starts in the outer disk and moves inwards, carrying with it an ever increasing amount of matter. While the disk remains quiescent in front of the wave, it switches into a hotter SS state behind it (*e.g.* Cannizzo 1998). The X–rays during the rise are then associated with magnetic reconnection generated by the MRI above the outbursting disk. In this case we would expect to see a steadily decreasing radius (*i.e.* an increasing amount of relativistic smearing) and $\Omega/2\pi$ remaining constant at a value of unity.

Again our data do not cover enough of the LS evolution to directly test this, but previous observations (both in Cyg X–1 and during the decline phase of the transient systems) show $\Omega/2\pi < 1$ (irrespective of the continuum model used), which is incompatible with the magnetic flares model described above (Gierliński et al. 1997; Życki, et al. 1997; 1998; Done & Życki 1999; Gilfanov et al. 1999; Zdziarski et al. 1999). However, if the reconnection regions are out-flowing rather than static then the reflection signature can be suppressed by the resulting anisotropic emission (Beloborodov 1999). For a constant outflow velocity this predicts that $\Omega/2\pi$ remains constant at some value < 1, while the amount of relativistic smearing increases. Alternatively, the generally observed LS correlation between spectral index and $\Omega/2\pi$ can be explained by a variable outflow velocity. Faster outflow velocities mean that more of the X–ray radiation is beamed away from the disk so there is

a smaller reflected fraction. This also means fewer soft photons from the disk are intercepted by the active region, so the spectra are harder (Beloborodov 1999).

3.6 Models of the very high state during the outburst

The (admittedly few) broad band HS/VHS spectra show a rather complex spectrum. There is plainly a strong disk component at $\sim$ 1 keV, and a high energy tail. The VHS spectrum shown in Figure 3.6 shows the tail extending out beyond 200 keV, while OSSE data from other objects show it out to even higher energies (Grove et al. 1998; Gierliński et al. 1999; Zdziarski et al. 2001). The lack of distinct scattering orders strongly argues against thermal Comptonization models in the HS of Cyg X–1 (Gierliński et al. 1999), and the two proposed mechanisms in the literature involve a non–thermal electron distribution either from magnetic flares (Poutanen & Coppi 1998) or from bulk motion of the infalling material as it approaches the black hole event horizon (Chakrabarti & Titarchuk 1995). The major problem with the bulk motion model is that the free–fall electron velocities are not high enough (typical velocities of $\sim 0.7c$ imply Lorentz factors of only $\gamma \sim 1.4$) to extend the power law past $\sim 100-300$ keV (Laurent & Titarchuk 1999; Zdziarski 2000) yet the highest signal–to–noise HS/VHS spectra extend unbroken beyond this (GRO J1655-40: Grove et al. 1998; Cyg X-1: Gierliński et al. 1999). Thus it seems that the power law *must* arise from a highly relativistic non–thermal electron distribution.

As well as the non–thermal power law, there is an additional continuum component which is clearly seen in the few broad band VHS/HS spectra (Figure 3.6, Figure 3.7 and Cyg X–1: Gierliński et al. 1999; Frontera et al. 2000; Kubota et al. 2002). This can be described as a thermal Comptonized continuum, but at lower temperature than the standard LS emission. It seems entirely possible that the difference between the VHS and HS spectra is merely in the strength of this additional thermal component. This thermal/non–thermal (or hybrid) plasma most likely represents incomplete thermalization of the magnetic reconnection energy, so that the thermal and non–thermal electron distributions are co–spatial rather than there

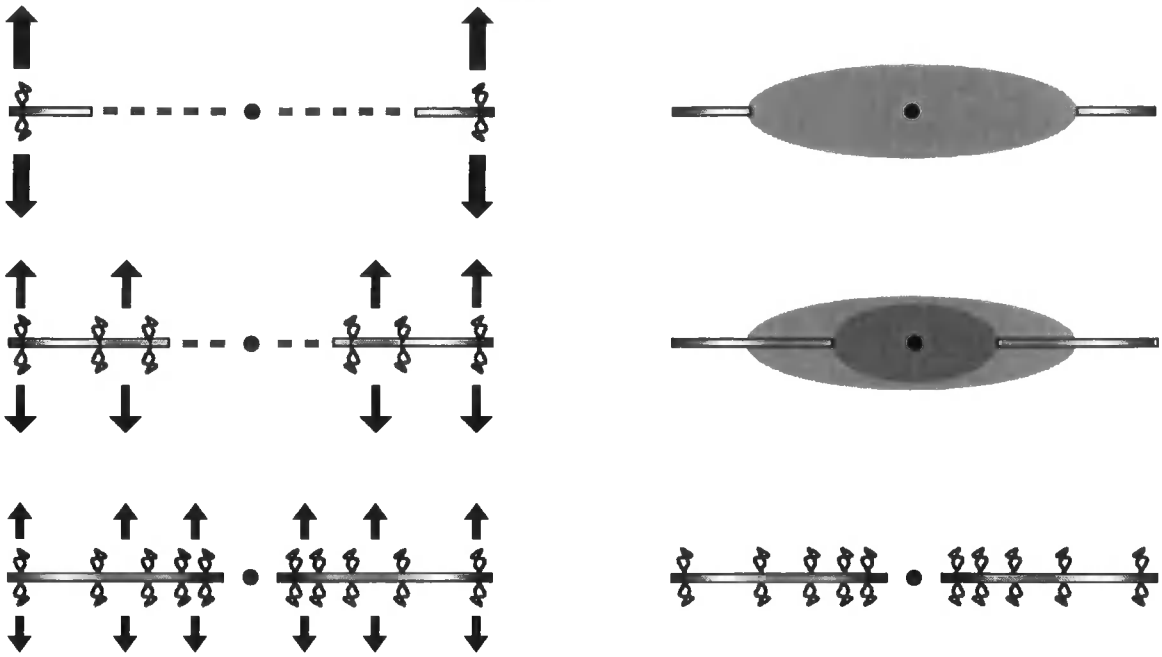

Figure 3.11: The left hand side shows a quiescent disk being gradually replaced by a hot/thin disk as the outburst progresses. A slowing relativistic wind is theorized as a mechanism for reducing the reflected fraction as the outburst progresses. The Balbus-Hawley reconnection regions are only present in the hot disk. The right hand side shows an ADAF being penetrated and eventually destroyed by an encroaching hot disk. In the final state, magnetic reconnection acts as the hard X–ray source.

being two separate electron populations (Poutanen & Coppi 1998; Coppi 1999).

Since there is very little radio emission in the HS (Fender 2000) the emission regions are probably not linked to a relativistic outflow. Thus, the HS (and by extension the VHS) are most likely to be linked with low velocity outflows, or static regions above the disk, (shown schematically in Figure 3.11). These regions should give rise to $\Omega/2\pi \sim 1$ in the reflector, and to an inner radius equal to the last stable orbit. This presents us with a problem as our data show a value of $\Omega/2/pi < 1$ even in the VHS. In the next section we examine the details of the mismatch between our models and the data and attempt to identify areas where our models could be incorrect.

3.7 A discussion of the derived parameters

The parameters which we actually derive are shown in figure 3.8. The reflected fraction, $\Omega/2\pi$, either remains essentially constant around a value of $\sim$ 0.1, or drops from $\sim$ 0.25 to 0.1 at the onset of the LS–VHS transition (depending on the continuum model used). The inner radius remains fairly constant: the errors on the data are large enough to cover most trends although we note that the results are never consistent with a disk extending down to the last stable orbit, nor with a disk truncated at 1000 Schwarzschild radii.

The LS spectrum is *roughly* consistent with the presence of either an ADAF or out-flowing magnetic flares above the (outbursting) disk. The data can even be compatible with *static* magnetic flares, as there is an ionization instability which is present in X–ray illuminated material in hydrostatic balance. Intense X–ray irradiation of the disk can produce a sharp transition in the vertical structure of the disk, with a highly ionized skin forming on top of mainly neutral material. In the LS, the hard spectrum has a Compton temperature which is high enough to completely strip iron. The skin is then almost completely reflective, and forms no spectral features. The observed reflection signature is then dominated by photons reflected from deeper in the disk, where the material is much less ionized (Nayakshin, Kazanas & Kallman 2000). If the skin has an optical depth of around unity then this appreciably reduces the reflection signature to $\Omega/2\pi < 0.3$ (Nayakshin 2000; Done & Nayakshin 2001). With magnetic flares, the ionized skin gives the observed $\Omega/2\pi < 1$ and correlation with spectral index, without requiring a moderately relativistic outflow from the disk (although such outflow may be additionally present). However, recent work has shown that this is unlikely to be true in the low state of Cygnus X–1 and so may *not* be the case in J1550–564 (Barrio, Done & Nayakshin 2003).

For the ADAF, the presence of a skin on the top of the disk could give rise to an *overestimation* of the amount of relativistic smearing. The observed, mainly neutral, reflected spectrum is subject to Compton scattering in the skin before it escapes. This can lead to some broadening of the spectral features (line and edge) in addition to the relativistic broadening of the features (see also Ross et al. 1999). Thus the

theoretical difficulties in maintaining an ADAF with a small transition radius could be removed if the transition radius is overestimated because of Compton smearing.

The detailed properties of the VHS reflected spectra are not at all consistent with the magnetic flares model developed earlier. The amount of reflection is very much less than $\sim$ unity predicted by such flares at low outflow velocity. However, the ionization is also high, indicating that we are *not* dealing with a mainly neutral disk. Unlike the LS spectrum, photo–ionization of the disk surface cannot easily suppress the amount of observed reflection. The Compton temperature is low, so the ionization state of the X–ray illuminated skin is not high enough to completely strip iron, and the derived solid angle is generally not strongly underestimated (Nayakshin, Kazanas & Kallman 2000; Done & Nayakshin 2001). However, there can also be substantial *collisional* ionization as the observed disk temperature is $\sim$ 0.7 keV, provided that the disk is in local thermal equilibrium (a likely assumption). We used reflection models which assume that the whole disk can be described by a single photo–ionization parameter, but plainly the hotter the disk, the more highly ionized it will be (due to collisional processes). From the Saha equation the mean ionization state of iron will be one in which the ionization energy is roughly equivalent to the temperature (*i.e.* we expect that iron should be dominated by He– and H–like ions in the central regions where the X–rays are predominantly produced). However, the electrons are very nondegenerate, and a better estimate of the ionization state is one with ionization energy $\sim 20kT$ *i.e.* the inner regions of the disk will contain iron that has been completely stripped through collisional ionization processes (Rybicki & Lightman 1979). Thus reflection from the inner disk could be completely ionized, and has no spectral features. It is, therefore, counted as continuum rather than reflected flux in spectral fitting. Observable reflection is only detected from further out in the disk, where relativistic smearing effects are smaller, although Compton up-scattering can again be an important broadening mechanism (Ross et al. 1999) which is not accounted for in our reflection code.

The importance of Compton up-scattering on our spectra can be demonstrated by the residuals to the VHS spectra. The co–added residuals to all the spectra after the sudden parameter transition are shown in figure 3.12. There is clearly a systematic problem with the modelling of the reflected features at a level of $\sim$ 1%.

A similar pattern of residuals is seen when models of ionized disks which include Compton up-scattering of the reflected spectrum are fit with the simpler reflection models used here (S. Nayakshin, private communication). Complete collisional ionization of the inner disk in the VHS can then lead to an underestimate of the solid angle subtended by the reflector, and to an overestimate of the inner disk radius, although this latter effect can be partially compensated for by the Compton up-scattering associated with the ionized disk reflection. Thus our derived $\Omega \sim 0.1$ and inner radius ≥ 10 Schwarzschild radii for the very high state may be consistent with a disk which subtends a solid angle of ~ 1 and extends down to the last stable orbit when *collisional* ionization effects are properly included.

This leaves us in the unfortunate situation of knowing even less than we did before. Ionization removes the last of our ability to test models for the origin of the X–ray spectra using currently available spectral models for fitting the X–ray reflected spectrum. However, we note one inconsistency which we suspect will remain even within properly calculated ionization models. The continuing increase in frequency of the QPO indicates that the switch to the VHS occurs before the heating wave has propagated all the way down to the last stable orbit. If so then we expect that the magnetic corona will continue to increase in luminosity as the disk radius decreases, but without a corresponding reflected signature. This would imply that the hard X–ray flux should increase, without a corresponding increase in reflection, so the measured reflected fraction should decrease (while the ionization state and relativistic smearing remain constant). However, we see the solid angle remain constant from the onset of the VHS transition. Plainly there is much that is still not understood about the nature of the VHS emission.

3.8 Summary

We have intensively studied the spectra of the rise phase of the outburst of RXTE J1550–564 in an attempt to identify observational differences between those models which have a hole in the disk and those without. At the onset of the XTE coverage, the source is in a classic LS, and can be fit with a spectrum consisting of seed photons from an accretion disk (not detected in the RXTE bandpass) being thermally

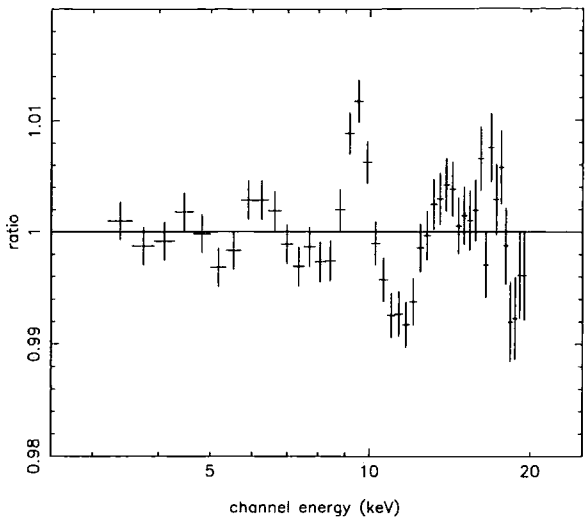

Figure 3.12: Co-added residuals of the later rise of J1550–564 showing the feature at 9 – 10 keV. This may be part of the instrument response or may be a result of our not modelling Compton upscattering of the reflected photons.

Comptonized into a hard X–ray spectrum which is then reflected from the disk. There is subtle curvature in the spectrum, perhaps indicating that a single temperature Comptonization model with reflection is inadequate, although it may also be an artifact of the PCA calibration. The source then makes a *very* smooth transition to the VHS (without going through the classic HS), where the spectrum is dominated by disk emission which is strongly Comptonized. The high energy spectral curvature during the transition is inconsistent with a single temperature Comptonization model. This effect is much larger in the later spectra and so is unlikely to be due to calibration issues. The transition and VHS spectra can be modeled by two thermal Compton components (one at low electron temperature, the other considerably higher). This could be indicative of a hybrid thermal–nonthermal plasma such as has been fit to Cyg X–1 HS spectra (Gierliński et al. 1999).

We are most interested in the reflected spectrum rather than the continuum, as this can be used to give an indication of the source geometry and whether this changes dramatically at the LS/VHS transition as required by ADAF models. We have derived values for the reflected fraction, the ionization parameter and the inner disk radius for each spectrum.

A sharp transition is seen in the ionization at the onset of the LS–VHS transition. The reflected fraction remains essentially constant at a value of $\Omega/2\pi = 0.1$ while

the ionization increases from mainly neutral to highly ionized. The inner radius inferred from relativistic smearing of the reflected spectral features could not be well constrained, but is never as small as the last stable orbit around a black hole. This is not consistant with *either* of our proposed models so we have attempted to identify any weaknesses in our model which may account for the difference.

Given theoretical uncertainties in the transition radius and extent of overlap between the ADAF and disk, the LS reflected spectrum is consistent with an ADAF interpretation, especially if photo–ionization of the disk gives rise to an ionized skin which introduces significant Compton broadening as well as relativistic smearing. Similarly, a photo–ionized skin can make magnetic reconnection models of the X–ray flux fit the data, even without significant outflow velocities of the hard X–ray region, although these can be additionally present. However, the fact that the LS is seen when the increasing QPO frequency and disk instability models clearly indicate that the outbursting disk has not yet reached the last stable orbit, shows that an inner SS disk is not a *necessary* condition on the LS X–ray emission.

Ionization can distort the reflected spectrum derived in the VHS, only this time it is collisional rather than photo–ionization which is likely to be important (assuming a disk which is in LTE). Again this can suppress the observed amount of reflection, and distort (generally suppress) the most highly relativistically broadened features from the inner disk.

Chapter 4

Astrophysical Compton Scattering

4.1 An overview of Compton scattering

An observational constraint of the physical location of the disk and the electron atmosphere would enable us to move forward with the theoretical modelling of disks. Since the principles in forming the components of a spectrum are well understood, establishing the geometry should be relatively simple. However, untangling the disk emission from the continuum is difficult, and untangling reflection is nearly impossible. Clearly we need a *very* accurate model of the Compton spectrum, so we can generate the correct continuum for a given situation.

Compton scattering, discovered by Arthur Compton in 1923, is a deceptively simple process. A single photon encounters (and loses energy to) a stationary electron which recoils. If the electron is originally moving, Lorentz transforms show that the energy exchange is very different in the laboratory frame. If the electron has sufficient momentum, the photon can gain energy.

Astrophysically, the Compton process is essential to understanding many of the phenomena associated with black holes. Compton downscattering, where the electron gains energy from the photon, is common in any situation where there are cold (low energy) free electrons and photons to encounter them (*e.g.* reflection from a cool disk). Inverse Compton scattering (sometimes called Compton cooling or Compton upscattering) occurs when the electron has more energy than the photon. In the resulting collision the photon will gain and the electron will lose energy (the electron will cool). In this way, low energy photons can be boosted to considerably higher energies.

4.2 Compton scatterings of single particles

4.2.1 The Compton cross–section

In the circumstance where the scattering is elastic in the electron rest frame (known as the Thomson limit) the differential Compton cross–section for unpolarized incident radiation in the electron rest frame is

$$\frac{d\sigma_T}{d\Omega_o} = \frac{1}{2}r_o^2(1 + (\vec{\Omega}_i.\vec{\Omega}_o)^2)$$

where $\vec{\Omega}_i.\vec{\Omega}_o$ is the dot product of the direction vectors of the input and output photon. The total cross–section (integrated over all possible output directions) is

$$\sigma_T = \frac{8\pi}{3}r_o^2$$

where r_o is the classical electron radius. This is independent of the relative energy of the two particles.

If the scattering is inelastic, electron recoil has a significant effect and the cross–section changes. The new version (the Klein–Nishina cross–section) in the electron rest frame is

$$\frac{d\sigma}{d\Omega_o} = \frac{r_o^2}{2}\frac{E_o^2}{E_i^2}\left(\frac{E_i}{E_o} + \frac{E_o}{E_i} - \left(1 + (\vec{\Omega}_i.\vec{\Omega}_o)^2\right)\right)$$

where E_i and E_o are the input and output energy. The Klein–Nishina cross–section drops as the photon energy approaches mc^2.

Generalising the Klein–Nishina cross–section to any frame gives

$$\frac{d\sigma}{d\Omega_o} = \frac{3\sigma_T}{16\pi}\frac{X}{\gamma^2(1 - \beta\vec{\Omega}_e.\vec{\Omega}_i)^2}\left(\frac{E_o}{E_i}\right)^2$$

where

$$X = \frac{x_i}{x_o} + \frac{x_o}{x_i} + 4\left(\frac{1}{x_i} - \frac{1}{x_o}\right) + 4\left(\frac{1}{x_i} - \frac{1}{x_o}\right)^2$$

and x_i and x_o are the electron rest frame values of the photon input and output energy.

$$x_i = 2\frac{E_i}{mc^2}\gamma(1 - \beta\vec{\Omega}_e.\vec{\Omega}_i)$$

and

$$x_o = 2\frac{E_o}{mc^2}\gamma(1 - \beta\vec{\Omega}_e.\vec{\Omega}_o)$$

Integrating gives the total cross–section for a photon encountering a moving electron

$$\sigma(x_i) = \frac{3}{4}\sigma_T \frac{1}{x_i}\left[\left(1 - \frac{4}{x_i} - \frac{8}{x_i^2}\right)\ln(1+x_i) + \frac{1}{2} + \frac{8}{x_i} - \frac{1}{2(1+x_i)^2}\right]$$

where x_i has the same definition as above. The cross–section is considerably reduced in those scatterings where $(E_i/mc^2)\gamma = 1$.

4.2.2 Final photon energy in the general case

In the case of a single scattering we use conservation of four–momentum to find the energy gained or lost by the photon. In general, photons have a four–momentum of

$$\mathbf{K} = \frac{E}{c}(1, \vec{\Omega})$$

and electrons have a momentum

$$\mathbf{P} = \gamma mc(1, \beta\vec{\Omega})$$

We should note that $\mathbf{K}^2 = 0$ and $\mathbf{P}^2 = m^2c^2$ in all circumstances. For any scattering, the momentum must be conserved so

$$\mathbf{K_i} + \mathbf{P_i} = \mathbf{K_o} + \mathbf{P_o}$$

where i and o denote input and output respectively. Squaring this and using the relations above, we get

$$\mathbf{K_i}.\mathbf{P_i} = \mathbf{K_o}.\mathbf{P_o}$$

but we can use the original conservation equation to remove the final electron momentum from the equation

$$\mathbf{K_i}.\mathbf{P_i} = \mathbf{K_o}.(\mathbf{P_i} + \mathbf{K_i} - \mathbf{K_o})$$

so

$$\mathbf{K_i}.\mathbf{P_i} = \mathbf{K_o}.\mathbf{P_i} + \mathbf{K_o}.\mathbf{K_i}$$

Using the Minkowski metric this becomes

$$\frac{E_i}{c}.\gamma mc(1 - \beta\vec{\Omega}_e.\vec{\Omega}_i) = \frac{E_o}{c}.\gamma mc(1 - \beta\vec{\Omega}_e.\vec{\Omega}_o) + \frac{E_iE_o}{c^2}(1 - \vec{\Omega}_i.\vec{\Omega}_o)$$

which can be rearranged to give

$$E_o = \frac{E_i(1 - \beta\vec{\Omega}_e.\vec{\Omega}_i)}{1 - \beta\vec{\Omega}_e.\vec{\Omega}_o + (\frac{E_i}{\gamma mc^2})(1 - \vec{\Omega}_i.\vec{\Omega}_o)}$$

This equation is for the general case and includes both the effect of electron recoil and relativistic boosting of the output photon.

4.2.3 Special cases

There are a few special cases which can shed light on the behaviour of the Compton process in certain extremes. Firstly, in the case where the initial electron is stationary, there is no relativistic boost, so the energy change is purely a result of recoil. The electron velocity, β, is set to zero, resulting in the rest frame output energy decrease given by the familiar Compton downscattering equation.

$$E_o = \frac{E_i}{1 + (\frac{E_i}{\gamma mc^2})(1 - \vec{\Omega}_i.\vec{\Omega}_o)}$$

If the momentum of the incoming photon is small in comparison to the apparent mass of the incoming electron, recoil is unimportant and relativistic effects dominate. Since there is no recoil, this is the Thomson limit. In such circumstances, the $\frac{E_i}{\gamma mc^2}$ term is so small as to tend to zero (which is the condition for Thomson scattering) and

$$E_o \approx E_i \frac{(1 - \beta\vec{\Omega}_e.\vec{\Omega}_i)}{(1 - \beta\vec{\Omega}_e.\vec{\Omega}_o)}$$

In the limit when $\gamma \gg 1$, the output photons are beamed into a cone of angle $1/\gamma$. Integrating over the dot product of the input and electron directions results in the approximate output energy as a function of the input energy and γ for the electron.

$$E_o \approx (\gamma^2)E_i$$

Conversely, in the extreme Klein–Nishina limit, when $\frac{E_i}{\gamma mc^2}$ dominates, the photon tends to the electron energy so

$$E_o \approx \gamma m_e c^2$$

We can also find an approximation for scattering of an electron with the average energy expected from a thermal (Maxwellian) distribution. Taking the equation for the output energy in Thomson scattering, we can express β in terms of a momentum, p. The average momentum in a non–relativistic thermal distribution is

$$\langle p^2 \rangle = 3mkT_e$$

Substituting for momentum in the output energy equation gives

$$E_o \approx E_i \left(1 + \frac{4kT_e}{mc^2}\right)$$

Guilbert (1986) calculates a more accurate version of this approximation and finds

$$E_o \approx E_i \left(1 + \frac{4}{x}\frac{K_3(x)}{K_2(x)}\right)$$

where $x = mc^2/kT_e$ and K_n is a modified Bessel function of order n. A simpler form of this equation (in which the Bessel functions have been expanded) is

$$E_o \approx E_i \left(1 + \frac{4kT_e}{mc^2} + 16\left(\frac{kT_e}{mc^2}\right)^2\right)$$

All the above information can be found (in various forms) in Pozdnyakov, Sobol & Sunyaev (1983) and Rybicki & Lightman (1979).

4.3 Compton scatterings of multiple particles

When there are many particles, the fraction which scatter is a function of the number density of photons and electrons in the system. Multiple scatterings (when a photon that has scattered once encounters *another* electron) must also be considered.

4.3.1 Optical depth

A simple parameter to quantify the fraction scattered is the optical depth. For a single photon encountering a distribution of electrons, it is defined as

$$\tau = N_e \sigma R$$

Where N_e is the number density of the electrons, σ is the cross–section of interaction and R is the distance that the photon travels though the electron field. In general the Thomson cross–section is used to define τ for a particular region. For those scatterings which are not in the Thomson limit the *effective* optical depth is found using the actual cross–section. In general, the probability of a photon scattering is $1 - e^{-\tau}$. So, approximately 60% of the photons scatter if $\tau \sim 1$. This leads to the definitions of regions which are optically thin ($\tau < 1$) and optically thick ($\tau > 1$). In the optically thin case the probability of a photon scattering is approximately τ, so a fraction τ of the photons would scatter when passing through an optically

thin region. In the case of optically thick scattering, the number of scatterings necessary for a photon to escape the system is dramatically increased. When a photon scatters its direction is changed so its mean free path is extended. As a result, a photon passing through an optically thick cloud of electrons is likely to scatter τ^2 times. An approximation for the number of scatterings in both optically thin and thick system is

$$n \approx \tau + \tau^2$$

4.3.2 The Compton y parameter

Multiplying the energy change per scatter by the probable number of scatters (both given above) results in the *total* fractional energy change for a photon passing through the system. This parameter (called the Compton y parameter) shows how important Compton scattering is for any given system. We represent the electron temperature by a dimensionless value $\Theta = kT_e/mc^2$ so

$$y = (4\Theta + 16\Theta^2)(\tau + \tau^2)$$

From now on we also use a dimensionless photon energy ϵ, which is defined as E/mc^2. In the case where the 'y' parameter is less than unity, there is not much change in the total energy of the system. If, however, it is greater than unity, there is a significant change in energy (Illarionov & Sunyaev 1972).

The relative amount of energy contained in the scattered and unscattered components of a spectrum relates to the y parameter. Hard spectra have more energy in the scattered component than the unscattered and so represent $y > 1$. Equally, soft spectra have only a small fraction of their total energy in the scattered tail and so have $y < 1$. The final energy of a photon which passes though a scattering medium is approximately

$$\epsilon_o \approx \epsilon_i e^y$$

(Rybicki & Lightman 1979).

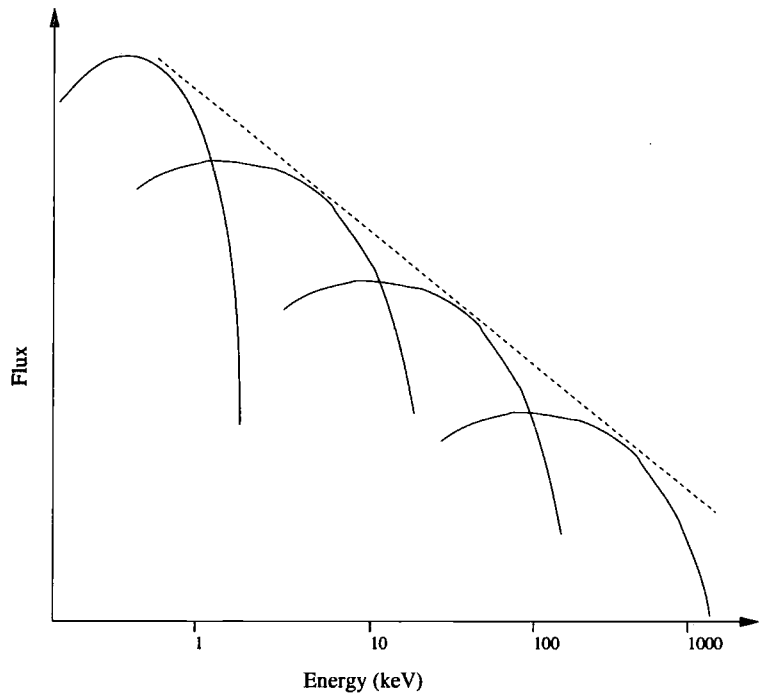

Figure 4.1: The first three scattering orders are shown here along with the initial black body spectrum. Since the plot is in flux, each order is a fraction τ below the previous one. Similarly, each has the same fractional increase in energy. The scattering orders sum to a powerlaw, shown by the dashed line.

4.3.3 Optically thin scattering by thermal electrons

If the electrons have a thermal distribution, the fractional energy gain and the optical depth can be used to predict the shape of the first order scattering spectrum. A schematic of an optically thin scattering is shown in figure 4.1 which plots flux against energy. The top of the first order scattered spectrum is a fraction τ below the peak of the input photon distribution and extends out to $(1+A)\epsilon_i$ (where A is the amplification: 4Θ in non–relativistic scattering). Each scattering order is the same fraction below the previous one and each is boosted by the same factor. Since each order of the spectrum is the same distance down the y–axis and across the x–axis, they sum to make an approximate powerlaw (shown as a dashed line) the index of which, α, is set by the electron energy and optical depth.

$$\alpha = \frac{-log(\tau)}{log(1+A)}$$

Figure 4.2 shows calculated versions of an optically thin, thermal scattering.

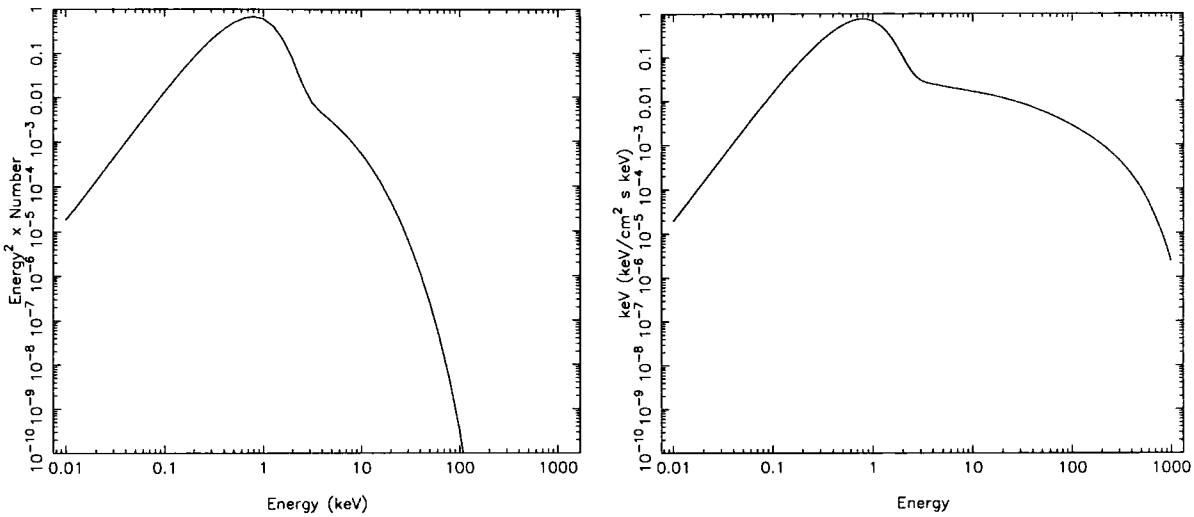

Figure 4.2: Left panel: A single scattering from a system with $kT_{bb} = 0.2$ keV, $\tau = 0.1$, and $kT_e = 102.2$ keV, so y = 0.144. A fraction, τ, of the photons have been boosted to a higher energy. Right panel: The total spectrum from all scattering orders of the same system. The spectrum is a powerlaw for most of its length with a roll–over at $\sim kT_e$. The approximation for the powerlaw index gives a value of 2.5 from the parameters. Fitting the powerlaw region ($5 - 40$ keV) with a powerlaw model gives a value of 2.45 ± 0.01.

The left panel shows a single scattering order, while the right shows the resultant powerlaw when all the orders are added together. The Compton y parameter is clearly less than unity.

The powerlaw cannot extend indefinitely because of the two processes which limit the maximum possible photon energy.

1) Conservation of energy means that the predicted final energy of the photons cannot be greater than the energy of the electrons. Any scattering that would make the photons have too high an energy, settles instead to the electron energy. From this point on, upscattering and downscattering are in balance and so no net energy exchange takes place. This causes the powerlaw to tail off at $\sim kT_e$ (hence the high energy roll–over in figure 4.2). The appearance in observed low/hard state spectra of a powerlaw which rolls over at around $100 - 200$ keV is one piece of evidence for a Compton cloud with a temperature in that region (*e.g.* Gierliński et al. 1997).

2) For the later scattering orders, the initial photon energy is quite high. Given a high enough initial energy, the scattering is not in the Thomson limit and the Klein–Nishina cross–section should be used. As a result, far fewer photons scatter

and they scatter to lower energies. This also results in a cut-off in the spectrum but at a fixed value of approximately 511 keV (Ghisellini 1989). This condition is not easily achieved in thermal electron distributions. It is more likely to occur when the electrons are non–thermal and so is shown later in figure 4.4.

4.3.4 Optically thick scattering by thermal electrons

As before, the probability of a photon scattering is $1 - e^{-\tau}$ but, in the optically thick case, this is now roughly unity. Clearly, most of the photons will be moved to a higher energy as only a small fraction escape without scattering. The highest energy they can reach is $\sim kT_e$. The shape of the resulting spectrum depends on the escape time of the system relative to the number of scattering necessary to reach the electron energy. If the number of scatterings to escape ($\sim \tau^2$) is less than the number of scatterings needed to reach the limiting energy, then the system is 'unsaturated'. In the reverse case, most of the photons are likely to end up at the electron energy. This 'saturated' scattering causes a peak at the high end of the spectrum, called a 'Wien peak' (Sunyaev & Titarchuk 1980). A Wien peak is caused by the photons at high energies scattering so often that they thermalize at the electron temperature. We can use the y parameter to judge whether a scattering will be saturated or not. Since y is approximately the fractional change in energy for a photon passing through the system, then the final energy will be $\sim \epsilon_i e^y$. If $\epsilon_i e^y \sim \Theta$ then most photons reach the electron temperature and the system will be saturated. Figure 4.3 shows the two types of optically thick scattering. In the left panel the y parameter is less than unity even though $\tau = 2$ so the spectrum has a steep powerlaw. The right panel shows the same parameters with a much higher optical depth ($\tau = 6$) which increases the y parameter. In this case, the spectrum has saturated so a Wien peak is visible.

One method of dealing with very optically thick Compton scattering is via the diffusion approximation. In a sufficiently thick system, the photons do not move very far before scattering. Provided that the energy change is similarly small (*i.e.* non–relativistic electrons), the photons can be treated as diffusing through space and energy. This is represented by Kompaneets' Equation (Sunyaev & Titarchuk

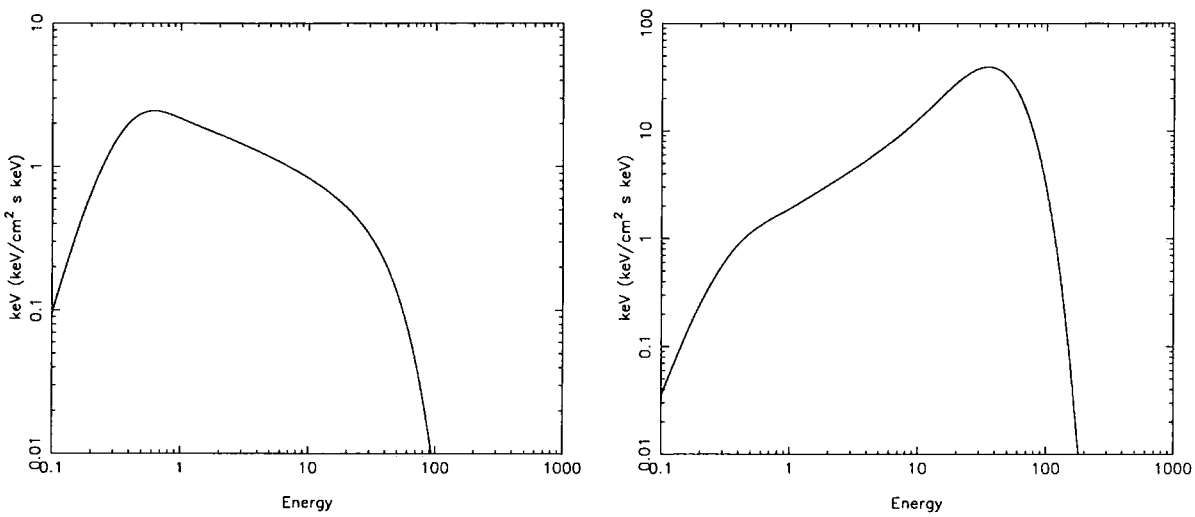

Figure 4.3: The spectrum shown in the left panel is that which results from a scattering with $kT_{bb} = 0.1$ keV, $\tau = 2$, and $kT_e = 10$ keV. The spectrum is a powerlaw for most of its length with a roll-over at $\sim 3kT_e$. Even though the optical depth is high the y parameter is only ~ 0.5. The right panel shows the results from a scattering with $kT_{bb} = 0.1$ keV, $\tau = 6$, and $kT_e = 10$ keV. The spectrum has a y parameter greater than 1 (~ 3.5) and is clearly saturated. A Wien peak (caused by thermalization of the photons at the electron temperature) is visible. These spectra were generated with the `compTT` model (Titarchuk & Lyubarskij 1995)

1980).

4.3.5 Scattering by Non–thermal electrons

In a single scattering, the energy to which a photon is scattered depends on γ. As stated above, the output energy in the Thomson limit and when $\gamma \gg 1$ is

$$\epsilon_o \approx (\gamma^2)\epsilon_i$$

This approximation is useful for individual scatterings, but we are more interested in distributions of particles. In non–thermal cases we assume the electrons have a powerlaw distribution (provided we a dealing with high values of γ).

$$N(\gamma) = N_0\gamma^{-p}$$

The Compton energy gain as a function of output energy must be equal to the rate at which energy is lost from the electrons.

$$\varepsilon(\epsilon)d\epsilon = \dot{\gamma}N(\gamma)d\gamma$$

Finding the rate of energy change and using the approximation for output energy (expressed in terms of γ) gives

$$\dot{\gamma} = U_{rad}\sigma c\gamma^2$$

so, substituting for $N(\gamma)$

$$\varepsilon(\epsilon) \propto \gamma^2\gamma^{-p}\frac{d\gamma}{d\epsilon}$$

and substituting for $d\gamma/d\epsilon$ and expressing in terms of ϵ_o

$$\varepsilon(\epsilon) \propto \epsilon^{-(p-1)/2}$$

(Ghisellini, quoted in Done 1989)

A single scattering order of a non–thermal Comptonized spectrum is therefore a powerlaw with energy index $\alpha = (p-1)/2$ assuming that the seed photons are mono-energetic. The second scattering is formed by using the first scattering order as seed photons. This has a very broad distribution so the second scattering is not a true powerlaw and each subsequent scattering is more curved than the previous ones.

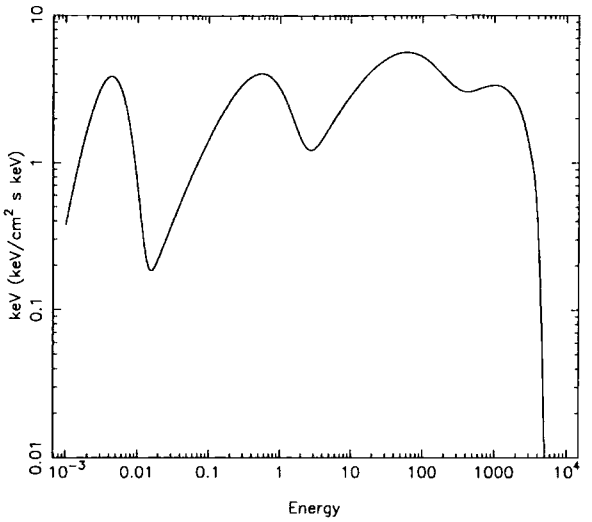

Figure 4.4: The spectrum shown here is from a non–thermal scattering with electron index $p = 0$, $kT_{bb} = 0.001$, $\gamma_{min} = 1$, $\gamma_{max} = 10$ and $\tau = 0.05$. The first and second scattering orders are clearly visible in this non–thermal scattering. The third order is visible but suppressed as the system is approaching the Klein–Nishina limit.

Up and down scattering balances when $\epsilon_o \gamma_{max} \sim 1$ (in the Klein–Nishina limit). Although non–thermal scattering produces a noticeably different final spectrum, the principles involved are identical to the thermal case. Figure 4.4 shows an example of a non–thermal scattering. The optical depth is very low so individual scattering orders become visible. The third order is visible but suppressed due to the scattering approaching the Klein–Nishina limit.

4.4 The Compton anisotropy

All the scatterings discussed so far have been assumed to be angle averaged. However, the equations for the energy distribution and cross–section are heavily angle dependent. The energy exchange is radically different depending on whether the collision is head–on or tail–on. Extrapolating from this, we can see that the resultant spectrum from a scattering will also be angle dependent.

In fact, there are two anisotropic effects which are best shown by assuming a highly relativistic electron that is encountered by a low energy photon. In such a collision, the output photon is most likely to be travelling in the direction of the electron. So, in a head on collision, the photon is turned 180^o and gains a large

amount of energy. In a tail on collision, the photon will barely change direction and the energy exchange will be small.

Similarly, the rate of collision is higher when the photons are travelling towards the electron rather than away from it. Consequently, the effective optical depth of a set of electrons will depend on the electron's direction relative to the photon.

The effect of this anisotropy is obvious in a situation where photons are travelling into a layer of isotropic relativistic electrons from below. It is at its strongest if the photons are unidirectional but a disk is better represented by a set of photons at a multitude of angles, all travelling into the electron region from its lower boundary. The two anisotropic effects combine so that the spectrum that is scattered out of the bottom of the layer has a higher intensity and energy than that which escapes through the top. A schematic diagram of this effect is shown in figure 4.5. The solid line shows the expected orders of scattering from an isotropic situation. The dashed line shows the spectrum which would pass through the bottom of the medium. Due to the anisotropic effect it has a higher apparent optical depth and reaches a higher energy. This is less true in the second order where the input photons (which have already scattered once) are more isotropic. By the third order the effect is negligible. The dotted line is the spectrum that would pass through the top of the system. It is at a lower energy and apparent optical depth. Again the effect fades as the number of scattering orders increases (Haardt & Maraschi 1993).

This Compton anisotropy was first noted in non–thermal scattering by Ghisellini et al. (1991). They calculated that, at its most extreme, the anisotropy boosts the intensity of returning photons by a factor of 5.5, assuming a disk geometry.

The above discussion holds true for less relativistic electrons. As the value of γ decreases, so does the anisotropy. Finally, for stationary electrons, the effect disappears completely, so upward and downward photons are identical. This is *not* to say that the scattering is completely isotropic. Photons emerging sideways from the collision will have a different energy from those emerging along the photon path, even for a stationary electron. This is caused by intrinsic anisotropies in the Compton cross–section.

Extrapolating this model of anisotropic behaviour in a slab to higher orders of scattering shows that the anisotropic effect is at its strongest at low energies. In the

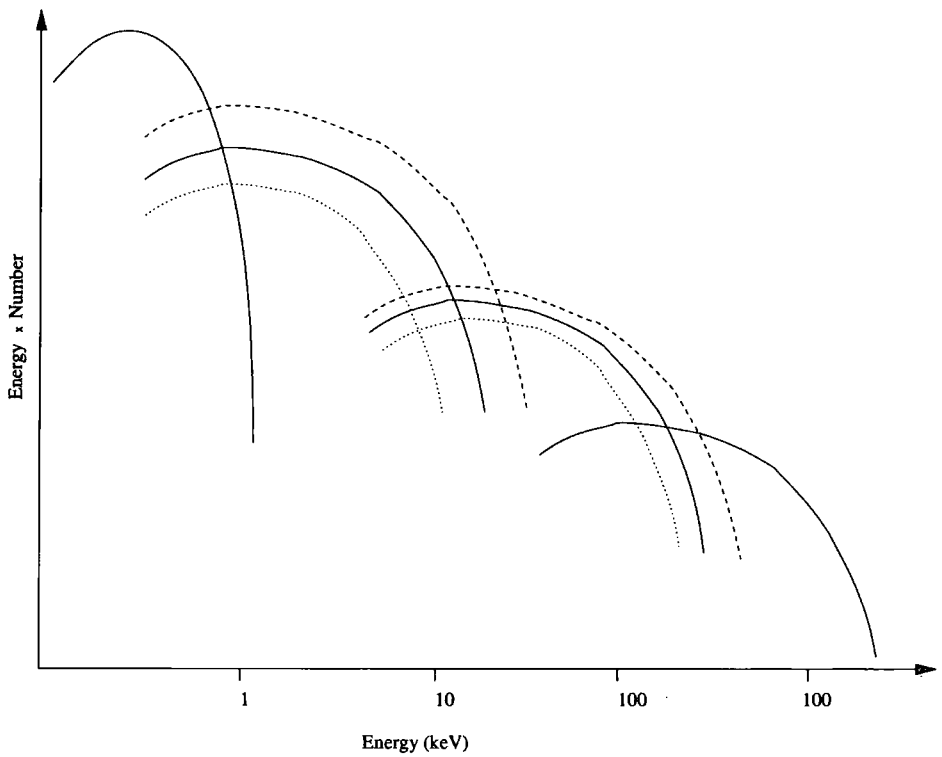

Figure 4.5: The solid line shows the expected orders of scattering from an isotropic situation. The dashed line shows the spectrum which would pass through the bottom of the medium. Due to the anisotropic effect it has a higher apparent optical depth and reaches a higher energy. This is less true in the second order where the input photons are more isotropic. By the third order the effect is negligible. The dotted line is the spectrum that would pass through the top of the system. It is at a lower energy and apparent optical depth. Again the effect fades as the number of scattering orders increases.

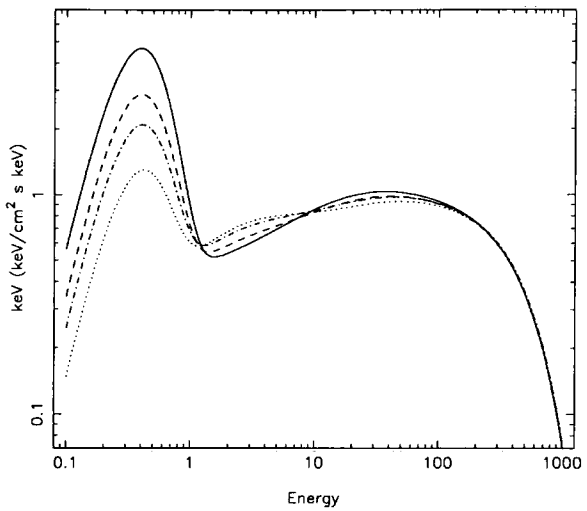

Figure 4.6: The spectra shown here result from scattering in a slab with $kT_{bb} = 0.1$ keV,$\tau = 0.2$, and $kT_e = 180.0$ keV. The solid line refers to $cos(\theta) = 0.9$, the dashed line to $cos(\theta) = 0.7$, the dot–dash line to $cos(\theta) = 0.5$ and the dotted line to $cos(\theta) = 0.3$. The anisotropy is clearly visible at low energies, around the region of the first two scattering orders. At higher energies there is no visible anisotropy.

case of the first scatter, the photons arrive preferentially from below. This will not be true once they have scattered, as their directions will be partially randomized by the scattering process. After the second scatter (which will be slightly anisotropic) the directions will be almost completely random and no anisotropy will be generated at higher order scatters. Figure 4.6 shows a series of spectra from Compton scattering in a slab geometry. The solid line ($cos(\theta) = 0.9$) is almost face on and so is lowest at energies in the region of the first scattering order. The dashed, dot–dash and dotted lines show $cos(\theta) = 0.7$, 0.5 and 0.3 respectively. The anisotropy is clear between energies of $1 - 10$ keV and vanishes at higher energies.

This sort of anisotropy has profound effects on the observed spectra from accreting objects. Any hot electron cloud will receive photons preferentially from the direction of the disk. Consequently there will be an anisotropy between the Comptonized photons that escape the system and those that return to the disk. As a result, the disk will reprocess a different continuum than the one which we observe.

For in depth discussions of the effects and theory of anisotropic Compton scattering see Haardt 1993; Haardt & Maraschi 1993; Haardt et al. 1993; Titarchuk 1994; Stern et al. 1995b; Poutanen and Svensson 1996; Gierliński et al. 1997, 1999

and also Sazanov and Sunyaev 2000.

4.5 Time dependence

Up to this point, Compton scattering has been considered as a static process. As such, the electrons have automatically maintained their temperature despite losing energy to the photons. Gaining an insight into the time dependence of a Comptonizing system requires comparing several key timescales.

The most fundamental timescale to any system is the light crossing time, t_{cross}. This not only gives us the minimum amount of time that light could be in the system but, more importantly, the smallest possible time in which a systemwide change can take place. For a system with a distance, R, between the photons entering and leaving, $t_{cross} = R/c$. In real systems the photons spend a longer time crossing the Comptonizing region because they interact with electrons on the way. Each interaction randomizes the photon direction and so increases the overall path length. Consequently, the amount of time for a photons to diffuse out of a system is $t_d \sim (1+\tau)R/c$.

The output spectrum of a system can be estimated by considering these times in relation to the thermalization time. This is the amount of time necessary for the photons to increase their average energy to that of the electrons. In the circumstance where $t_{therm} \ll t_d$ the photons will spend longer passing through the system than is necessary to reach the electron temperature. This is equivalent to saying that the system is saturated and that a Wien peak is formed. At the other extreme ($t_{therm} \gg t_d$) most photons pass through the system without reaching the electron energy, instead forming a powerlaw (this is covered in more detail in Guilbert, Fabian & Ross 1982).

To consider the effect of the photons on the electron temperature we need to consider the electron cooling time.

$$t_{cool} = \frac{E}{dE/dt} = \frac{\gamma_e m_e c^2}{dE/dt}$$

We can find dE/dt from the rate of collision between particles, multiplied by the energy loss per collision. Using the values for the photon energy gain (and hence

electron energy loss) found earlier, we find (in the limit where $\gamma \gg 1$),

$$\frac{dE}{dt} = \frac{U_{rad}}{\epsilon}\sigma_T c\gamma^2\epsilon = \frac{L\sigma_T}{\epsilon R^2}\gamma^2\epsilon$$

So

$$t_{cool} = \frac{mc^3R^2}{\gamma L\sigma_T c}$$

But R/c is the light crossing time, so

$$t_{cool} = \frac{mc^3R}{\gamma L\sigma_T}t_{cross}$$

Here we can introduce the compactness.

$$\ell = \frac{L}{R}\frac{\sigma_T}{mc^3}$$

which is a dimensionless representation of the luminosity to size ratio of a source. It is closely related to optical depth, which is a dimensionless representation of the number density *of photons*. Previously, we have discussed the optical depth as representing the number of electrons encountered by a single photon. The optical depth *here* is that formed by a distribution of photons being encountered by a single electron. The relation between the compactness and optical depth is $\ell = \epsilon\tau$ (Guilbert, Fabian & Rees 1983) where ϵ is the typical photon energy in dimensionless units.

This gives us a simple relation between the electron cooling time and the light crossing time.

$$t_{cool} = \frac{t_{cross}}{\gamma\ell}$$

For the electron temperature to remain roughly stable as light passes through the system $t_{cool} \gg t_{cross}$ clearly this can only happen if ℓ is very small. In those circumstances which obey this condition the electron temperature changes very slowly with time. However, if $t_{cool} < t_{cross}$, the electrons lose most of their energy on timescales shorter than the light crossing time.

The above analysis assumes that the energy in the electrons is not being replaced. If the electron were heated impulsively (*e.g.* by a short timescale flare) then we could use the cooling time to judge the gradual loss of energy. However, we can envisage a system where the electrons are heated over time (with an associated

timescale). Clearly, if this timescale is short enough ($t_{heat} \sim t_{cool}$) then the electron temperature will remain stable. The electron thermalization time is also important in such systems. This is the time necessary for the electron to reach thermal equilibrium. If this time is short enough the electron distribution will always be thermal, otherwise a more complex electron distribution is formed. For example, if the electrons were thermalized slowly by Coulomb collisions, a hybrid plasma would be formed. At low energies, Coulomb interactions would be the dominant cooling mechanism and the distribution would be thermal. However, Compton scattering would be the dominant coolant at high energies so the distribution would be a powerlaw. The relative levels of thermal and non–thermal electrons in the distribution would depend on the rate of cooling by each process (Poutanen & Coppi 1998; Coppi 2000).

4.6 Summary

Despite its apparent simplicity, Compton scattering is one of the most complex two particle interactions in astrophysics. It is also one of the most important, since it occurs in a wide variety of phenomena. It is fortunate that so many regimes exist in which approximations can be made. The Thomson limit and the extreme relativistic limit have allowed the scattering process to be modelled reasonably accurately even by relatively slow computers. However, the complexities of the Compton anisotropy and the problems of calculating time dependence have increasingly forced us to rely on numerical codes. As computational power increases over the next few years there is great potential for analytic codes which can be used to calculate Compton scattering in all regimes.

Chapter 5

Modelling Compton Scattering

5.1 Why do we need a new Compton code?

The X–ray spectra seen from both galactic black holes and AGN are generally attributed to Compton upscattering of lower energy seed photons by energetic electrons (Sunyaev & Titarchuk 1980). The temperature of the soft X–ray component is consistent with these seed photons coming from the disk. In the low/hard state there is a spectral roll–over at $\sim 100 - 200$ keV, which is a clear indicator that the electrons have a (quasi)thermal distribution, while the X-ray spectral shape implies an optical depth of order unity (Zdziarski et al. 1995; Gierliński et al. 1997). Accurate modelling of the Comptonized component is essential for interpreting complex spectra. This is especially true in the case of reflection, where a slight error in the continuum can have profound effects on the derived parameters (Weaver, Krolik & Pier 1998).

As we discussed in chapter 4, accurate analytic approximations for Compton scattering exist in several regimes such as moderate optical depth, low electron energies (Sunyaev & Titarchuk 1980; Titarchuk & Hua 1995), or small optical depths with relativistic electrons (Jones et al. 1980; Coppi 1992). Unfortunately, the spectral parameters inferred from the data are precisely where these analytic approximations do not work. Transrelativistic electron temperatures and optical depths of order unity make the situation very complex.

One approach to this problem is to use probability based codes (such as Monte–Carlo calculations). They produce accurate spectra for arbitrary geometries, optical depths and electron energies. An inherent problem of Monte–Carlo codes is that

the probability of forming very high energy photons is small and so an extremely large number of photons is required if the high energy spectra are to have accurate statistics. This can be solved by using a weighted photon system,which allows high energy photons to carry more statistical weight than low energy photons (Pozdnyakov, Sobol & Sunyaev 1983; Gorecki & Wilczewski 1984). The major drawback with Monte–Carlo codes is that they are inherently probabilistic and so never produce exactly the same results for the same set of input parameters. Consequently, they cannot be used for spectral fitting, which relies on a computer smoothly mapping an increase or decrease in χ^2 with a change in parameter.

An alternative approach is to numerically solve the radiative transfer equations in a given geometry. There are a several such numerical codes which can be used for spectral fitting. For example, `compPS` calculates the numerical solution of the radiation transfer equations in several possible geometries. However, it is only accurate up to optical depths of ~ 3 (Poutanen & Svensson 1996). For higher optical depths codes like `compTT` (Titarchuk & Lyubarskij 1995) and `thComp` (Zdziarski, Johnson & Magdziarz 1996) are used. These solve the Kompaneets' equation using a diffusion approximation and so are only accurate in regions of medium to high optical depth and low to medium electron temperature.

All of these codes produce static spectra but the spectral shape and normalization of observed X–ray emission is variable on all timescales (van der Klis 1994). Clearly Comptonization is time dependent as well as geometry dependent. Some progress has been made in developing time dependent probability codes. For example, a large–particle Monte–Carlo code (Stern et al. 1995a) has been used to predict the time dependent behaviour of moving electron clouds (Malzac & Joudain 2000; Malzac, Beloborodov & Poutanen 2001).

We have developed a time dependent, direct numerical (analytic) code, which can be used for an arbitrary geometry, optical depth and electron temperature. Until recently, such work has been too computationally intensive to achieve in a reasonable time. Here we describe several features which reduce the problem to more manageable timescales.

5.2 Modelling Compton scattering by distribution functions

5.2.1 Methodology

The basic methodology is descended from that of Guilbert (1981), which breaks the Comptonizing region into smaller parts both temporally and spatially. Across small enough regions of space there is no change in the number and energy distributions of photons and electrons. Consequently, the scattering is computationally identical within each small region. Similarly, over small enough steps in time, we can assume that the photons and electrons only scatter once. The time dependent behaviour can be generated by allowing the photons to propagate on the light travel time. This is shown in the following algorithm (adapted from Guilbert 1981):

(i) divide the electron gas up into elements small enough that the probability of scattering does not significantly change within each element;

(ii) calculate the scattering probability for each element;

(iii) calculate the new photon distribution in each element by using the present distribution and the scattering probability;

(iv) transport the photons spatially;

(v) return to step (ii).

The behaviour of a region of arbitrary geometry can be generated by stacking the small cells together. Fortunately, a disk geometry generates a situation with a broad angle distribution of photons. Consequently, we have envisaged the scattering region as an infinite slab atop a disk which allows us to the use the inherent azimuthal symmetry. The photon distribution only changes with height in the slab and with inclination angle, θ. We break the slab of optical depth τ into many equal layers of small optical depth, $d\tau$. Because each layer is optically thin we can safely make the assumptions required to use the Guilbert method. A three layer slab is shown schematically in figure 5.1.

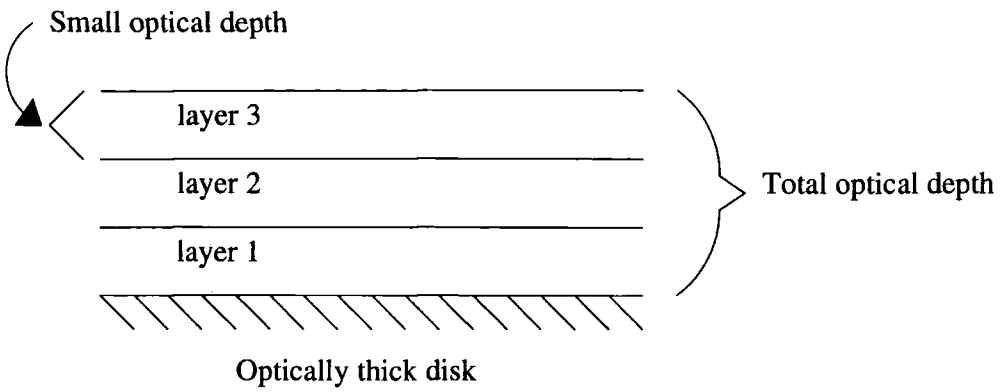

Figure 5.1: The layer structure allows us to construct optically thick systems while calculating in the optically thin regime. In this example, three layers of a small optical depth have been placed above an optically thick disk, making a higher total optical depth.

5.2.2 Initial photon distribution

Following Guilbert (1981), we use a fixed angle grid with axes that are set up to utilize the symmetry of our geometry. The z–axis, from which θ is measured, is perpendicular to the layer boundaries. Consequently, the input photons and electrons are symmetric in ϕ. As a result, the same symmetry is true for the output photons. The solid angle subtended by each bin is given by $d\Omega = dcos(\theta)d\phi$ and we set each bin to have the same solid angle ($dcos(\theta) = 2/8$ and $d\phi = 2\pi/16$). This is a very coarse angle grid but we are severely limited by run–time issues. We need to keep track of the angles of three particles (the input photon, the input electron and the output photon). Because of the photon and electron symmetry in ϕ, we need only keep track of 5 independent angles. Therefore, if we were to double the angle grid resolution, the run–time would increase by a factor of $2^5 = 32$.

To allow for the large range of energies which can result from a scattering we use a logarithmic energy grid whose upper boundary is defined by the electron temperature ($15kT_e$) and whose lower boundary is defined by the photon temperature ($0.05kT_{bb}$). The energy and direction are taken at the mid point of the energy and angle bins. Since we are using a system which is similar at any point in an infinite

layer, we calculate in number densities (*i.e.* the photon and electron distributions are taken to be in a unit volume).

The photon spectrum which is input into the program is a bosonic black body and is a function of $\epsilon, \vec{\Omega}$ and the layer number.

$$\frac{dn}{d\epsilon d\Omega} = \begin{cases} \frac{\epsilon^2/kT_{bb}}{e^{\epsilon/kT_{bb}}-1}, & cos(\theta) > 1 \\ 0, & cos(\theta) < 1 \end{cases}$$

Because we are modelling radiation entering the disk from below, we limit the incoming photons to upward directions. The amount of photons at each angle is multiplied by $cos(\theta)$ which is a geometrical factor resulting from the photons passing over the boundary between the disk and the electron cloud. These photons are initially uniformly present in all layers and directions, to model a situation where electrons are impulsively heated in a region above the disk.

5.2.3 Initial electron distribution

First we consider a purely thermal distribution and, at this stage, we do not take electron cooling into account (so the electron temperature does not change over time). We use a logarithmic grid which counts over $\gamma - 1$ to store the electron distribution ($\gamma_{min} = 1$, $\gamma_{max} = 1 + 15(kT_e/mc^2)$). The electron distribution is dependent only on the electron temperature (kT_e) as the electrons are isotropic in direction. We use a relativistic Maxwellian to describe the electron distribution

$$\frac{dN}{d\gamma} \propto \gamma(\gamma^2 - 1)^{1/2} e^{-\gamma/(kT_e/mc^2)}$$

(taken from Pozdnyakov, Sobol and Sunyaev 1983)

5.2.4 The calculation of the Compton scattering

Having now established both the electron and photon distributions in the layer we process the scattering. In reality, a series of discrete collisions take place continuously over the whole time step. We reduce this to a single event in which *all* the scatters are processed at once (following our assumption that the timestep is short enough for only one scatter to occur). In principle, the entire photon distribution and the entire electron distribution interact. That is not to say that *every* photon

or *every* electron scatters, merely that there is a probability for a photon of every energy and direction to encounter an electron of every energy and direction.

A single photon can move a distance dr in a time dt. Therefore

$$dr = cdt$$

We let the layers (each of optical depth $d\tau$) be of height dr and set a time–step as dt. This ensures that a photon will only move through one layer at a time. We use the definition of optical depth

$$d\tau = N_{total}\sigma_T dr = N_{total}\sigma_T cdt$$

where N_{total} is the total number density of electrons in a layer. Each layer contains a photon distribution

$$\frac{dn}{d\epsilon d\Omega}(\epsilon, \vec{\Omega})$$

which scatters off a similar electron distribution.

$$\frac{dN}{d\gamma d\Omega}(\epsilon, \vec{\Omega})$$

For convenience, we always represent photon distributions as dn and electron distributions as dN. The output energy from a Compton scattering is

$$\epsilon_o = \frac{\epsilon_i(1 - \beta\vec{\Omega}_e.\vec{\Omega}_i)}{1 - \beta\vec{\Omega}_e.\vec{\Omega}_o + (\frac{\epsilon_i}{\gamma})(1 - \vec{\Omega}_i.\vec{\Omega}_o)}$$

Using this equation we derive the output energy directly. The cross–section is

$$\frac{d\sigma}{d\epsilon_o d\Omega_o} = \frac{3\sigma_T}{16\pi}\frac{X}{\gamma^2(1 - \beta\vec{\Omega}_e.\vec{\Omega}i)^2}(\frac{\epsilon_o}{\epsilon_i})^2\delta(\epsilon - \epsilon_o)$$

We calculate the probability that a photon scatters from one given energy and direction to another. To start, we consider the loss rate of photons which have a particular energy and direction (ϵ_i and $\vec{\Omega}_i$) when they encounter electrons at a particular energy and direction (γ and $\vec{\Omega}_e$). This rate is proportional to the total cross–section which exists between the two distributions of particles (σ). We use the total cross–section as we are integrating over all output energies and directions.

$$\frac{-dn_i}{dt} = dn_i(\epsilon_i, \vec{\Omega}_i)dN(\gamma, \vec{\Omega}_e)(1 - \beta\vec{\Omega}_e.\vec{\Omega}_i)\sigma(\epsilon_i, \vec{\Omega}_i, \gamma, \vec{\Omega}_e)c$$

The factor of $(1-\beta\vec{\Omega}_e.\vec{\Omega}_i)$ results from the relativistic transform into the lab frame (Blumenthal & Gould 1970). We convert this to the rate of transfer of photons to *and from* a particular energy and direction (ϵ_o and $\vec{\Omega_o}$). The total cross–section is now a partial cross–section, $d\sigma$.

$$\frac{d}{dt}\frac{dn}{d\epsilon_o d\Omega_o}d\epsilon_o d\Omega_o = \frac{dn}{d\epsilon_i d\Omega_i}d\epsilon_i d\Omega_i(1-\beta\vec{\Omega}_e.\vec{\Omega}_i)\frac{dN}{d\gamma d\Omega_e}d\gamma d\Omega_e\frac{d\sigma}{d\epsilon_o d\Omega_o}d\epsilon_o d\Omega_o c$$

Substituting the optical depth for cdt in our rate equation generates the output distribution of photons from a particular input distribution that has travelled through an optical depth of $d\tau$ (note that σ_T has cancelled).

$$\frac{dn}{d\epsilon_o d\Omega_o}d\epsilon_o d\Omega_o = \frac{dn}{d\epsilon_i d\Omega_i}d\epsilon_i d\Omega_i(1-\beta\vec{\Omega}_e.\vec{\Omega}_i)\frac{dN}{d\gamma d\Omega_e}d\gamma d\Omega_e\frac{d\sigma}{d\Omega_o}d\Omega_o\frac{d\tau}{N_{total}}$$

This equation gives the number of photons which are scattered to energy (ϵ_o) and direction ($\vec{\Omega_o}$) when a number of photons (at energy ϵ_i and direction $\vec{\Omega_i}$) encounter a distribution of electrons (at γ and direction $\vec{\Omega_e}$) with optical depth τ. In general multiple inputs can result in an identical output. Consequently we must numerically integrate over all the input parameters (*i.e.* the energy and direction of the input photon, the energy and direction of the input electron and the direction of the output photon). This fully defines the output energy of the photon so there are no free parameters. Using the equation above, we find the number of photons which scatter from an initial energy bin to a final energy bin and place the differential number density of scattered photons into their new energy and direction bins. Similarly, we remove this number from the input photon bins to represent their loss. This results in the scattered spectrum after the light has crossed the layer.

5.2.5 Moving photons between layers

We have now modelled the photons crossing a layer of electrons and scattering off them. Our final task is to establish which of the scattered photons move into other layers. In a slab geometry we are only interested in whether an electron has crossed into the layer above or below it. For a particular angle bin, a fraction $cos(\theta)$ of the photons pass from one layer to the next. There is no ϕ dependence, as Compton scattering is symmetric in azimuth. Any photons which pass out of the top layer have escaped the scattering medium and are used to generate the output spectrum.

Reprocessing is not included at this stage, so any photons which pass out of the bottom of the medium are lost.

Those systems with higher optical depths have several layers. Naïvely, we would expect such systems to take longer to run but this is not the case. The calculation of the cross–section is the most computationally intensive part of the code. However, this calculation is identical for each layer and so only needs to be computed once per scattering. By arranging the loops so that any calculation involving different layers (those which include the photon and electron distribution) is inside the loops required to find the cross–section there is only a small increase in run–time for high optical depth systems.

5.3 Modelling Compton scattering with a coarse angle grid

The fixed angle grid method outlined above develops a problem at reasonably high electron temperatures (nearing or above 511 keV). The cross–section is heavily peaked due to the high momentum of the incoming electron, resulting in the output spectrum being beamed into a cone of opening angle $\sim \gamma$. When the cone is smaller than the angular resolution of the angle bins, the cross–section and output energy change enormously across one angular bin. Figure 5.2 shows the change with angle of the photon output energy and the Compton cross–section. The two vertical lines are the size of one bin in our system. It is clear that, by taking the value of these parameters from the centre of a bin, the coarse–binned method badly overestimates the total number scattered and the photon output energy.

For relativistic electrons, the cross–section is always peaked in the direction of the incoming electron so the effect is most marked when the output photon and the input electron are aligned (in the same angular bin). In this circumstance we use an altered scattering routine which models the correct distribution of photon and electron scattering angles within a bin.

The variation in cross–section over an angle bin is mainly dependent on the angle between the electron and the output photon (which we label χ) and mostly

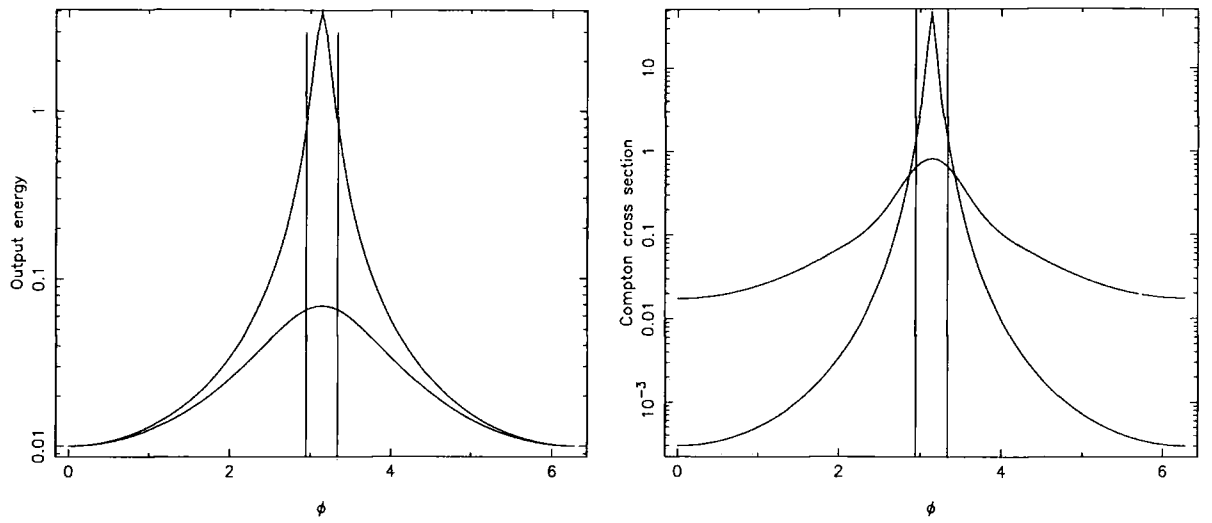

Figure 5.2: The electron is set at a ϕ value of π and the output energy (left panel) and cross–section (right panel) are calculated as the output photon direction is varied. The lower line is for $\gamma = 1.5$ and the upper line is for $\gamma = 10$. The two vertical lines are the width of one ϕ bin. Clearly in the latter case the assumption of constancy across a bin is invalid.

independent of the input photon direction. Since the angle bins are so wide, there are many possible directions inside each bin that a particle could be travelling. Previously we have assumed that the direction of a particle *within* a bin was unimportant and it is this assumption which causes the inaccuracy. Plainly we need to know the probability of each possible χ on sub–bin scales.

The probability of a particular χ occurring is a function of the bin geometry. If we break the bin down into infinitesimal fragments of direction we can calculate how often a particular χ occurs within a bin. Clearly, the output photon travelling in the same direction as the electron is most likely because every direction inside the electron bin has a correspondingly similar direction in the photon bin. As the angle becomes more oblique, there are less combinations of direction which can result in a given value of χ. Only photons and electrons travelling exactly along the bin edge can make the sharpest angles, so those angles have the smallest probability. This is shown schematically in figure 5.3.

In the bin system we are using, the probability of scattering can be represented as a sum of two exponentials. The accuracy of this approximation is demonstrated in figure 5.4. The crosses are actual values of the probability of scattering at a

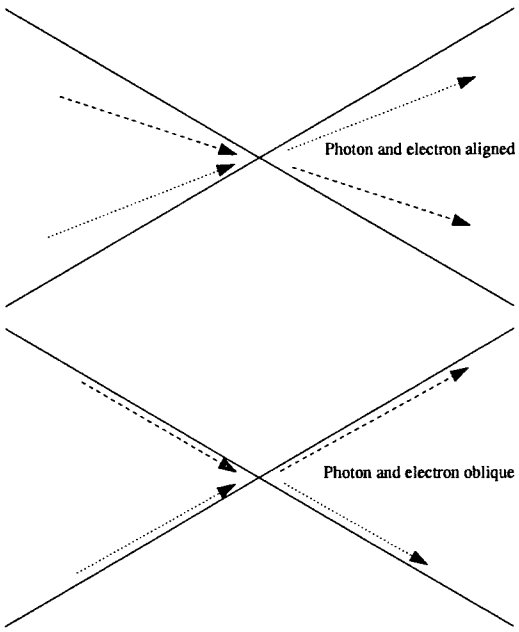

Figure 5.3: This picture is a schematic of the probability of different scattering angles that can occur within a single bin. A pair bins (for the input electron and output photon) have been collapsed into 2 dimensions. As can be seen from the top picture, any input angle will have a corresponding output angle which will be aligned (the dotted and dashed pair). Consequently, combinations that can achieve $\chi = 1$ are the most probable within a bin. The lower picture shows two very oblique scatters. In 2 dimensions there are only 2 input angles which can achieve such sharp angles of scatter. Consequently the most oblique angles are the least likely.

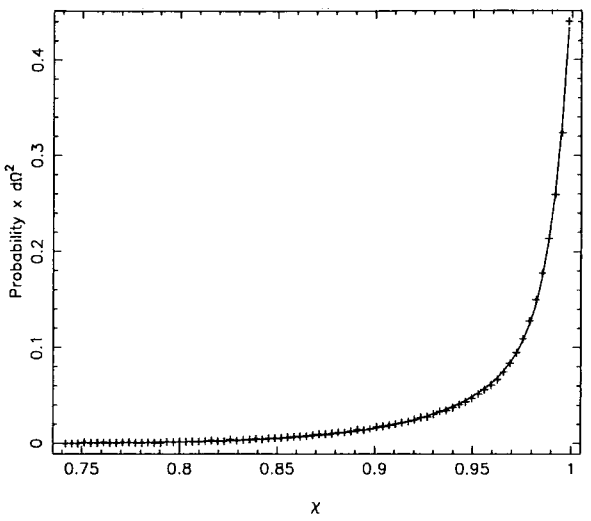

Figure 5.4: The probability of scattering at a particular value of χ in the uppermost θ bin ($cos(\theta) = 0.875$). This is expressed as a multiple of $d\Omega^2$. The solid line is the double exponential fit which is very accurate ($< 1\%$).

particular value of χ in the uppermost θ bin (expressed as a multiple of $d\Omega^2$). The solid line is the double exponential approximation which is very accurate (the difference is less than 1%).

To calculate the correct scattering probabilities we step over the energy grid. We start with the energy of the lowest energy photon that can be generated from within the angle bin (the sharpest possible angle) and count to the energy which results from the particles being exactly aligned (which has to be the highest possible energy). For each energy bin, we calculate the range of χ values that result in a photon of energy within that bin. We then find an average value of the cross–section for each range of χ. We use this in the main scattering equation and multiply by the integral of the probability between the two values of χ. The scattering can now be handled normally and will result in the right number of photons being scattered into the right energy bins even though the angle grid can be substantially coarser than the cross–section peak.

If the input photon is *also* in the direction of the electron and output photon the dot product of the input electron and input photon is unity. As a result the scattering probability is zero. In our correction we assume that this dot product is invariant, even as the electron direction changes within a bin. This is reasonable in most cases but is clearly untrue in this specific case. Letting the dot product vary

would complicate the correction considerably. Instead, because the scattering rate is almost zero, we neglect this case.

5.4 Steady state spectra and time dependence

Once each scattering and movement has been carried out, the set of photons which pass out of the top of the slab are used to generate the output spectrum. In the early stages of the scattering, only a small number of photons have been inserted into the system so only a small number escape. As time progresses the number and energy of photons in the system increases (both by scattering and by more photons being inserted) until the the energy exchange settles (*i.e.* there is no net change in photon energy and output spectrum). To generate a static solution, we model many scatterings and stop when the total energy in the photons at the start of a scatter is identical to the total energy at the start of the previous scatter (to the 0.0001% level).

By writing out *each* output spectrum even before a steady solution has been reached, we have harnessed the inherent time dependence of our model. Each spectrum represents the output from the electron region at a time $dt = dr/c$ after its formation. Hence we are not just modelling the steady state output from a rapidly heated electron region above a disk, we are also modelling its formation over time.

5.5 Comparisons with known methods

5.5.1 Analytic solution for a single scattering

The first comparison is with an analytic solution for Compton scattering using the following equation for relativistic scattering (taken from Blumenthal & Gould 1970).

$$\frac{dN}{dtdE_o} = \frac{2\pi r_0^2 mc^3}{\gamma} \frac{n(\epsilon_i)d\epsilon_i}{\epsilon_i} \left[2qln(q) + (1+2q)(1-q) + \frac{1}{2}\frac{(\Gamma_e q)^2}{1+\Gamma_e q}(1-q) \right]$$

where

$$q = E_o/\Gamma_e(1-E_o)$$

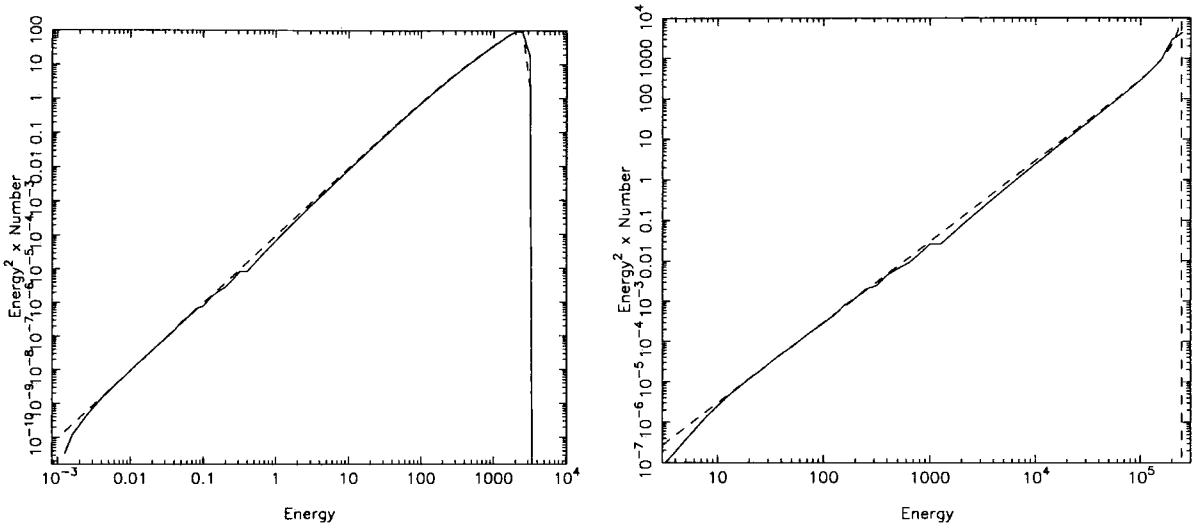

Figure 5.5: Comparisons of our code (solid line) with an analytic approximation for highly relativistic scattering (dotted line) taken from Blumenthal and Gould 1970. Left panel: a set of photons at $kT = 0.003$ keV were scattered off electrons at $\gamma = 500$. Right panel: a set of photons at $kT = 10.0$ keV were scattered off electrons at $\gamma = 500$. The instabilities at mid energies are caused by the cross–section and output energy changing rapidly over angle bins which are not aligned with the electron direction.

$$\epsilon_o = \gamma mc^2 E_o$$

and

$$\Gamma_e = 4\epsilon_i \gamma / mc^3$$

This equation includes all Klein–Nishina effects in the scattering. It models the output kernel for an isotropic, single energy (ϵ_i) photon distribution scattering off an isotropic, single energy (γ) electron distribution. To mimic this, we use δ functions for the input distributions rather than the black body and Maxwellian described earlier. In the first test we set $\epsilon_i = 0.003$ keV and $\gamma = 500$ so the scattering is in the Thomson limit. We use an optical depth of $\tau = 0.1$ and isotropic angular distributions. Figure 5.5 shows the match between the code and the analytic result.

The small instabilities in the lower energy sections of the graph do not have a significant effect on the total energy and number of photons in the scattering. Integrating the curves shows that the total energy matches to within 3% (with an individual point deviation of up to 50%). These instabilities are a result of the coarse angle grid at mildly-relativistic energies (hence their appearance in the mid

point of the curve). The code to correct the problems with the coarse angle bins at high electron energies only operates when the output photon and input electron are aligned. However, there can also be significant change in the cross–section and output energy in the situation where the output photon is slightly skewed from the input electron angle to the adjacent angle bin. The left panel of figure 5.6 shows the theoretical structure of the curve we are trying to model. The solid line is the output which results from scattering where the output photon is in the same angular bin as the incoming electron. The dashed line shows the output from the other bins and the dotted line shows the total output. It is obvious that the off angle bins make up a significant fraction of the output even at quite high energies. The right panel shows the same curves as calculated by our code. The solid line is much the same although there are some differences at the high energy end when out energy bins become rather large. The dashed line (off angle calculation) shows serious instabilities and cuts off too early. This is because the output energy curve is changing rapidly across the off–axis bin. Again we are taking the central value which is not the maximum energy that could be generated from a scattering within that bin. In principle, we could use the same approach as we use for on–axis calculations to correct all such problems, but since the effect is relatively small we neglect it.

We also perform the scattering with the input photons at a temperature of 10.0 keV, which is well within the Klein–Nishina region. The match, shown in the right hand panel of figure 5.5 is excellent and the area under the two curves is again the same. The analytic solution does not include downscattering so the mismatch at energies lower than the photon input temperature is not relevant.

We have shown that the code correctly models the scattering of δ functions. To demonstrate that distributions of photons and electrons are also correctly handled we compare the scattering of a thermal photon and electron distribution with the analytic solution. By envisaging the photon and electron distributions as a sum of δ functions at varying temperatures we construct the final spectrum as a sum of these analytic output spectra. As can be seen from figure 5.7 the results are generally good and the distributions of input photons and electrons smoothes out some of the numerical effects.

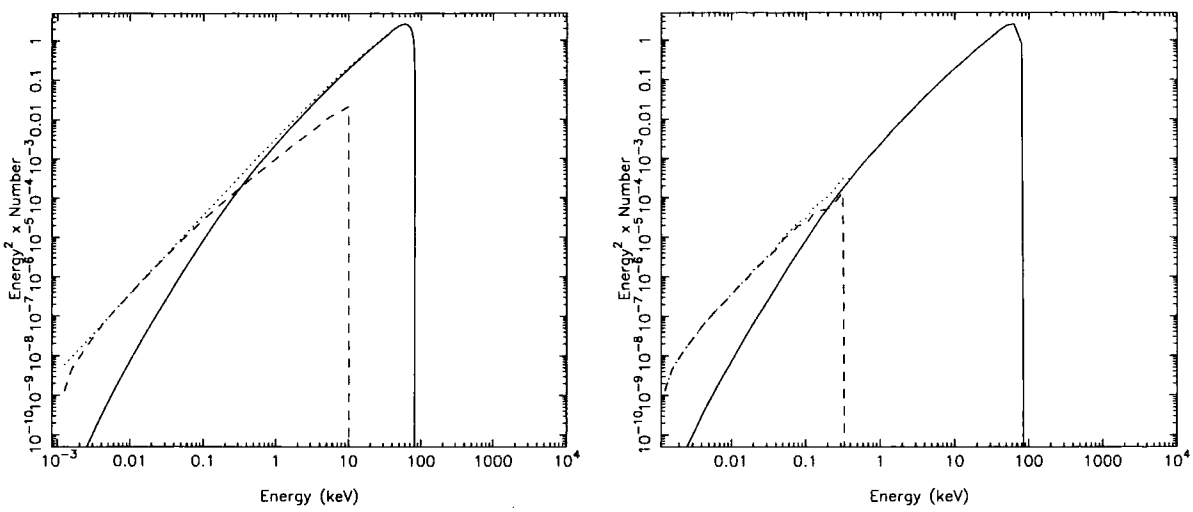

Figure 5.6: The left panel shows the theoretical structure of a scattering from a set of photons at $kT = 0.003$ keV which were scattered off electrons at $\gamma = 500$. The solid curve is from the output photons which are in the same angle bin as the incoming electron. The dashed curve is from those which are not and the dotted curve is the total of the two. The right panel shows the same curve as calculated by our code. The off-axis curve (dashed) shows instabilities at the high energy end resulting in unusual features in the total curve. It also does not extend to high enough energies. This occurs because we do not model those interactions in the off-axis bin that result in such energies.

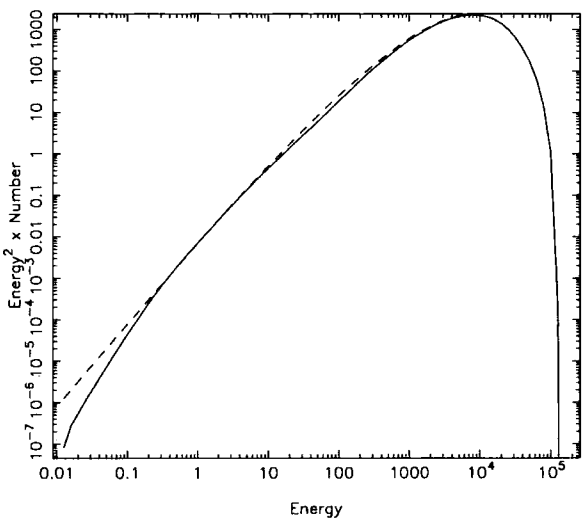

Figure 5.7: Comparison of our code (solid line) with an analytic approximation for thermal scattering (dotted line) taken from Blumenthal and Gould 1970. A black body set of photons at $kT = 0.2$ keV were scattered off a thermal set of electrons at $kT = 10$ MeV.

5.5.2 Numerical solution of radiative transfer for multiple scatterings

Poutanen and Svensson's `compPS` code (Poutanen & Svensson 1996) models the radiative transfer equations for Compton scattering in a number of geometries, assuming a low optical depth ($\tau < 3$). We use the slab geometry to check that our code models anisotropic scattering correctly. To show the working of our code at both low, medium and high electron temperatures we use values of $\Theta = 0.2$, $\Theta = 2.0$ and $\Theta = 20.0$ (corresponding to 102.2 keV, 1022.0 keV and 10220.0 keV respectively). The photon black body has a temperature of 0.2 keV and the system has an optical depth of $\tau = 0.1$.

As can be seen from figures 5.8, and 5.9 our results match well although there is a slight difference in photon index which we attribute to the coarse angle grid. The problem discussed above, where there is significant change in cross–section and output energy across *several* angle bins can be a more serious issue at these sort of electron temperatures. The errors (which are only dependent on γ) are at their worst between $\gamma = 2$ and $\gamma = 60$. An electron temperature of 1022.0 keV is thus in the worst place. Similarly, a fraction of the electrons will be at these unfortunate energies even if the temperature is lower (*e.g.* 102.2 keV where $\gamma \sim 1.5$). The resulting inaccuracies can lower the number of photons reaching the highest energies. This tips the spectral index, causing a steepening of the spectrum. The right panel of figure 5.8 shows that the problem with the spectral index vanishes at the highest energies for the 10220.0 keV curve. The electron distribution would have an average γ of ~ 60 so most of the distribution would be out of the problematic region.

All these comparisons were at an angle of $cos(\theta) = 0.875$ which corresponds to the first angular bin in our system. We show a comparison at more oblique angles in figure 5.9 ($cos(\theta) = 0.375$ and $kT_e = 102.2$ keV). The relative amounts of black body and Compton tail have clearly changed with angle. In a slab geometry, more black body photons escape upwards than sideways as the optical depth is higher at more oblique angles. Consequently, more of the black body photons are scattered before they leave the system. The low energy end of the spectrum contains the

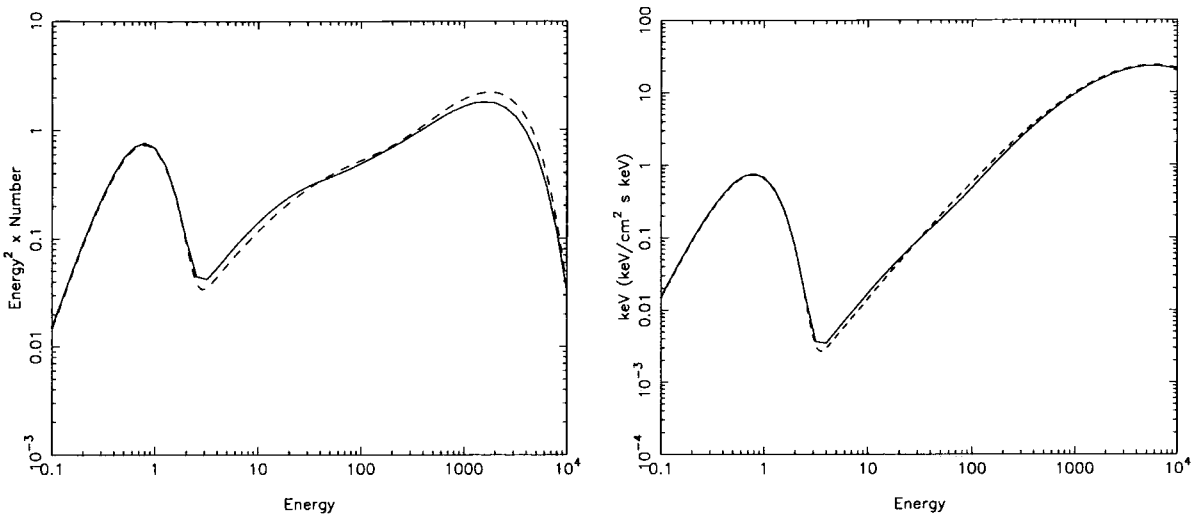

Figure 5.8: Comparison of our code (solid line) with **compPS** (dotted line) at an electron temperature of 1022.0 keV (left panel) and 10220.0 keV (right panel).

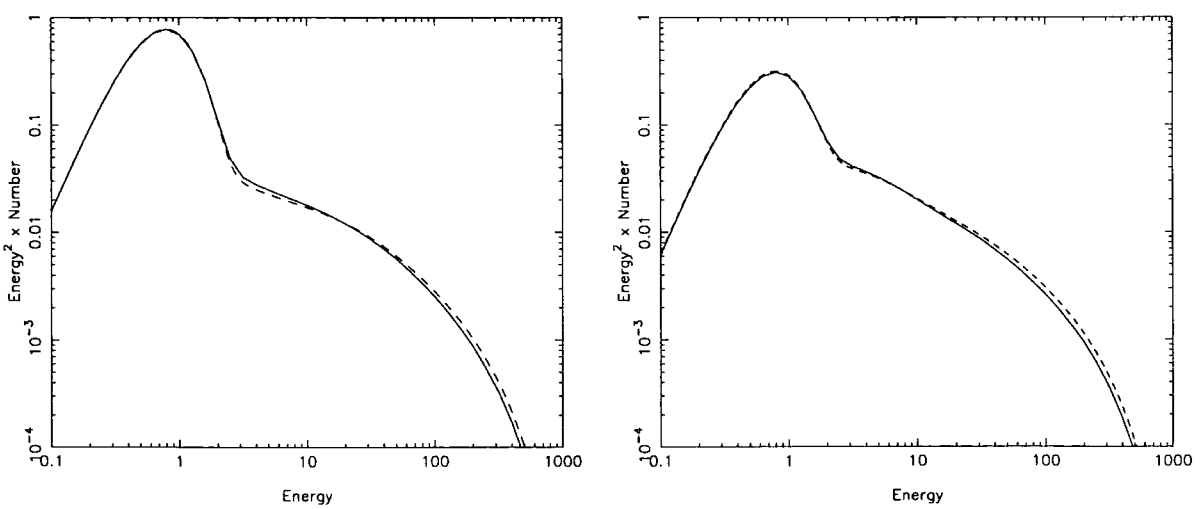

Figure 5.9: Comparison of our code (solid line) with **compPS** (dotted line). Left panel: $kT_e = 102.2$ keV and $cos(\theta) = 0.875$. Right panel: $kT_e = 102.2$ keV and $cos(\theta) = 0.375$.

unscattered photons so there are less in the $cos(\theta) = 0.375$ plot.

5.5.3 Monte–Carlo numerical solution for multiple scatterings

Thus far we have referred to the code as if it had arbitrary optical depth but all the tests have been on optically thin systems. Here we use $kT_{bb} = 0.2$ keV, $kT_e = 180$ keV and $\tau = 1.0$, which results in a 10 layer system. We use `compPS` as a comparison and also use a Monte–Carlo code (Gierliński 2000) as we are moving out of the accurate range of `compPS`. This is shown in figure 5.10 where our code is the solid line, `compPS` is the dashed line and the Monte–Carlo code is the dotted line. The scattered spectrum is well modelled by `compPS` which matches the Monte–Carlo code. Again, our spectral index is steeper in relation to both codes. However, our code is more accurate at low energies where the unscattered spectrum is over–estimated by `compPS`. From an observational point of view, the hard X–ray spectrum shown in figure 5.10 cannot be represented as a powerlaw. The anisotropic input photons cause spectral curvature, which is poorly fit by a powerlaw fit except over a very small energy range.

5.5.4 Non–thermal electron distributions

Converting the code to model a scattering from a non–thermal distribution is very simple. Replacing the relativistic Maxwellian with a powerlaw of given limits does not change the operation of the code. For comparison, we use

$$\frac{dN}{d\gamma} \propto \gamma^{-2}$$

where $\gamma_{min} = 1$ and $\gamma_{max} = 100$. As before, we use an optical depth of 0.1 and $kT_{bb} = 0.2$ keV (figure 5.11). The codes match well, although the difference in photons index is still apparent. This is to be expected as we have made no changes to the angle grid and most of the electron distribution is within the range at which the distribution of scattering angles in adjacent bins to $\vec{\Omega_e}.\vec{\Omega_o} = 1$ is important. Again the problem is disappearing at the highest energies. Comparison beyond

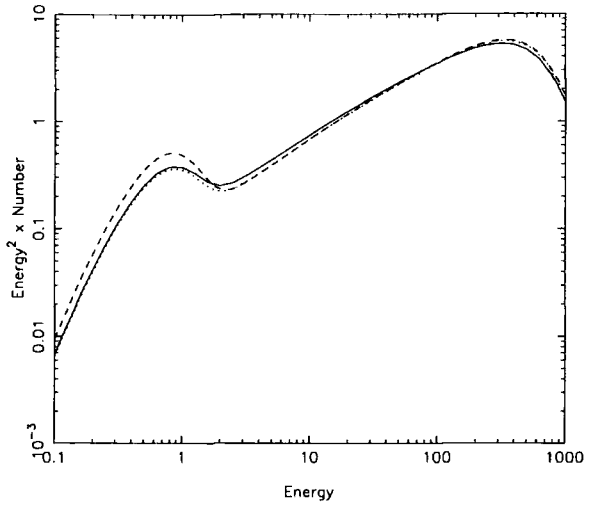

Figure 5.10: A comparison of our code (solid line) with compPS (dashed line) and a Monte–Carlo code (dotted line) with $kT_e = 180.0$ keV, $kT_{bb} = 0.2$ keV and $\tau = 1.0$ at an angle of $cos(\theta) = 0.875$. The scattered spectrum is well modelled by compPS. Once again, the spectral index is slightly steeper when modelled by our code. At low energies, compPS over–estimates the number of unscattered photons. Our code is a good match to the Monte–Carlo simulation in such energies.

these energies is impossible because compPS has a fixed end–point to its internal energy grid.

5.6 Cylindrical geometry and spectral fitting

5.6.1 Modelling a cylindrical system

One of the possible uses of a static code of this type is to investigate the spectral fitting of outputs from differing geometries. In theory, we can make any, cylindrically symmetric, geometry by redefining the rules for passing photons between layers (or cells in a 3-D situation). Unfortunately, this can increase the run–time and memory requirements beyond currently available levels. However, cylindrically symmetric systems, in which $\tau_{horizontal} \leq 0.1$ are easily modelled as they can still be treated as 1-D situations. Using this fact, we find the output from a cylinder with $H \gg R$. We define our cylinder as having a height of $\tau = 1$, a radius of $\tau = 0.05$ and an electron temperature of 180 keV. It is composed of 10 cylindrical cells each

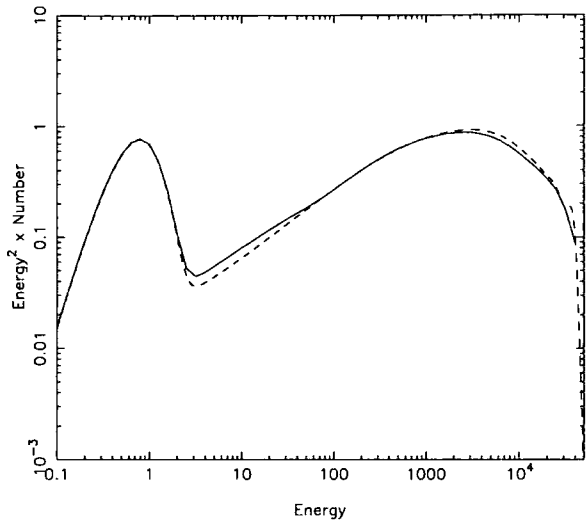

Figure 5.11: A comparison of scattering with a non–thermal electron distribution. The parameters are $p = 2$, $\gamma_{min} = 1$, $\gamma_{max} = 100$, $kT_{bb} = 0.2$ and $\tau = 0.1$. Again the spectral index is not well modelled at medium energies. At the highest energies it is clear that the index is beginning to match `compPS`. Comparison beyond these energies is impossible because `compPS` has a fixed internal energy grid.

of height and diameter $\tau = 0.1$ (shown schematically in figure 5.12).

After each scatter, $sin(\theta)$ of the photons escape through the sides of the system (if we envisage the edge of the cylinder as a vertical layer boundary, this follows the same logic as earlier). As before, a fraction $cos(\theta)$ of the photons will pass into the layers above and below. Consequently, a fraction $cos(\theta)(1 - sin(\theta))$ of the photons pass into the layers above and below and do not leave the cylinder. Equally, a fraction $(1 - cos(\theta))(1 - sin(\theta))$ remain in their original cell. Those photons which pass through the sides of the system are added to the observed photon distribution. New photons are introduced at the bottom of the system as normal. Equally, photons can enter through the sides of the cells. Again, this can be seen as a vertical layer boundary so we add a distribution proportional to $sin(\theta)$ (where $cos(\theta) > 0$ to ensure upward only photons).

This is a different approach to that used in the cylinder geometry of `compPS` which introduces photons isotropically from the bottom and does not insert any through the sides. Modelling the input in this way forces the photons into a beam of the same width as the cylinder. Compared to a slab, this increases the anisotropy of the system rather than decreasing it. By allowing photons to enter through the

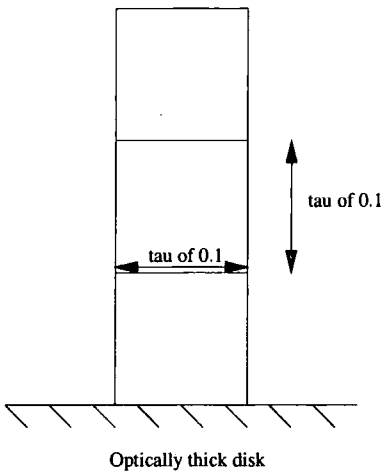

Figure 5.12: By using cylindrical cells of equal height and width we are able to construct an optically thick cylindrical geometry with no increase in complexity.

sides of the system we are modelling a more realistic situation, one in which the cylinder is sitting on the surface of a disk and receiving light from thermal disk emission at any height.

The resulting steady state spectrum is shown in figure 5.13. At the lowest energies ($0.01 - 1$ keV) the angles at which photons which pass through the lowest optical depth should have the highest luminosity but there is also an intrinsic angle distribution in the disk flux. These effects combine so that the upper angle bins are the most luminous. Between 1 keV and 100 keV there is a large anisotropy. This is *not* the same anisotropy as discussed earlier. It is a geometric effect caused by the optical depth being lower in some directions than others. Several scatters must have occurred to generate energies higher than 100 keV. Consequently, those photons which have passed through the highest optical depth are most likely to reach these energies. For these photons, the angle dependence in the spectrum depends only on the photon direction which results from the final scatter. Even though the maximum $\tau = 1$, the y–parameter is quite small (roughly 1) because the optical depth varies substantially across the system.

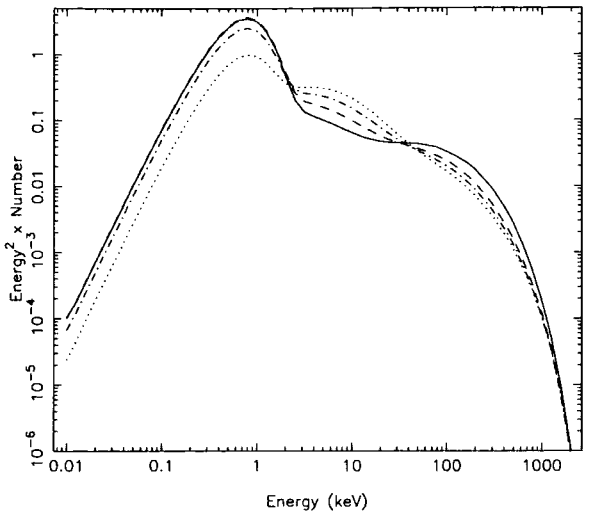

Figure 5.13: The steady state spectrum of photons passing through a cylinder of hot electrons ($kT_e = 180$ keV). The cylinder has a height of $\tau = 1$ and a diameter of $\tau = 0.1$. The solid line represents photons travelling at an angle $cos(\theta) = 0.875$, for the dashed line, $cos(\theta) = 0.625$, for the dash–dot line, $cos(\theta) = 0.375$ and for the dotted line, $cos(\theta) = 0.125$.

5.6.2 Spectral fitting of cylindrical systems

We use the output from a cylinder to simulate a data set which we can then fit with other models. Data from the results at an inclination of $cos(\theta) = 0.625$ (the dashed line in figure 5.13) were simulated using the RXTE (PCA and HEXTE) response matrices. By fitting the resulting data with differing models we can see if data such as this might exist in observed sources, pointing to cylindrical geometry in genuine systems. The simulated data is identical in structure to that used in chapter 3. Although we use all channels for the simulation, for fitting purposes the energy range was limited to $3 - 20$ keV for the PCA data and $30 - 200$ keV data for HEXTE. Systematic errors of 0.5% were added to the PCA data.

Phenomenological model

We initially fit the data with a phenomenological model of a disk black body and a powerlaw. Since the data have no visible high energy roll–over there was no need to include an exponential cut–off. Despite there being no relation between the model used and the model from which the data was generated, the fit was

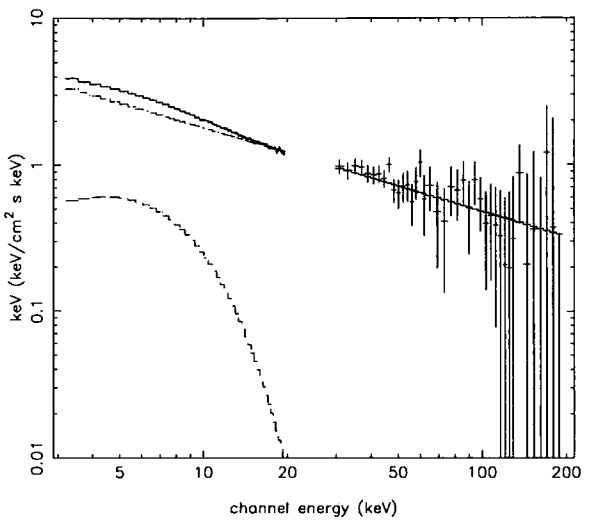

Figure 5.14: RXTE data is simulated from the output of the cylinder code at an inclination of $cos(\theta) = 0.625$. Fitting with a phenomenological model results in an excellent fit ($\chi^2_\nu = 49.7/81$) but with unphysical parameters. Although the powerlaw is reasonable for this sort of spectrum, the unphysically hot disk ($kT_{bb} = 1.87$ keV) is actually modelling the spectral curvature.

excellent ($\chi^2_\nu = 49.7/81$). The best fit parameters (shown in figure 5.14) give a powerlaw spectral index of $\Gamma = 2.5$ and a disk temperature of $kT_{bb} = 1.87$ keV. This disk temperature is far above that expected for a normal accretion disk. Since we know that the *real* disk in the spectrum is outside our spectral range, this disk is actually modelling the spectral curvature caused by the geometric anisotropy. Even though the model fits spectacularly well, the resulting parameters are meaningless because they bear no relation to a physical system. This is generally true for such phenomenological models where the price of excellent fitting is the physical meaning of the parameters.

Single Compton spectrum model

Fitting the data with a single Compton spectrum and a black body shows whether it is possible to fit a Compton spectrum from one geometry with a spectrum from another. It also examines the robustness of the Compton parameters when the geometry has not been fully understood. We use `compPS` set to a slab geometry and achieve a fit of $\chi^2_\nu = 92.34/80$, considerably worse than the phenomenological model (shown in figure 5.15). The best fit parameters show an electron temperature of

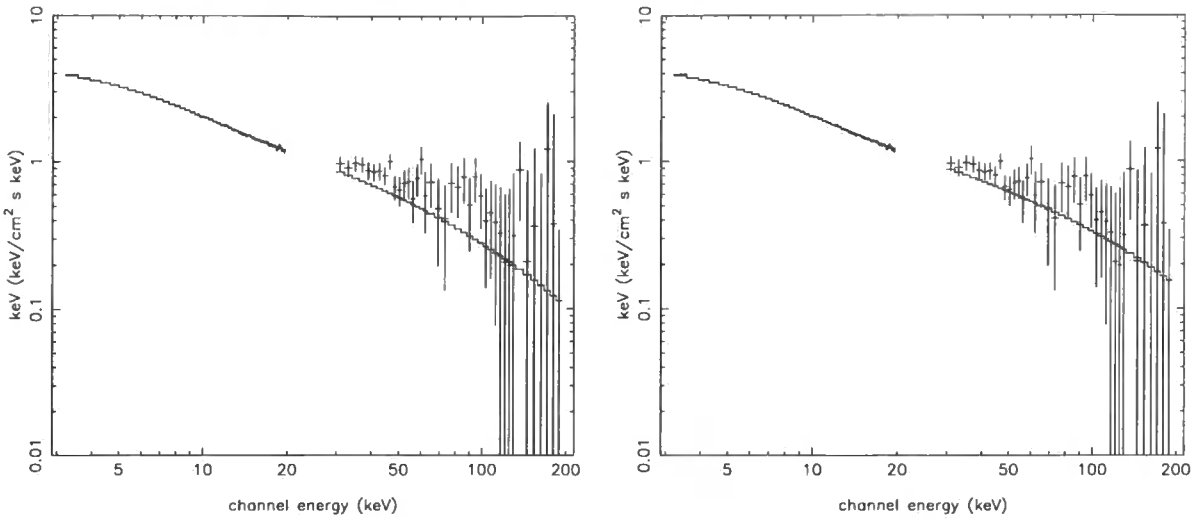

Figure 5.15: RXTE data is simulated from the output of the cylinder code at an inclination of $cos(\theta) = 0.625$. Left panel: Fitting with a disk black body ($kT_{bb} = 0.2$ keV) and Compton spectrum from a slab achieves a fit of $\chi^2_\nu = 92.34/80$. The electron parameters are $kT_e = 108.1$ and $\tau = 0.08$ neither of which are in agreement with the parameters of the original model. Similarly, the inclination is found to be $cos(\theta) = 0.28$. Right panel: Fitting with a disk black body ($kT_{bb} = 0.15$ keV) and Compton spectrum from a sphere achieves a fit of $\chi^2_\nu = 84.9/80$. The electron parameters are $kT_e = 121.1$ and $\tau = 0.22$. Again, neither are in agreement with the parameters of the original model.

$kT_e = 108.1$, an optical depth $\tau = 0.08$ and an inclination of $cos(\theta) = 0.28$ (which is radically different from the value of $cos(\theta) = 0.625$ used to generate the data). It is this that allows the slab model to fit the simulated data from a cylinder. In observational cases it is therefore clearly important to find the inclination of a system (via optical observation). It is pleasing that the disk temperature is correctly found in this case, even though the rest of the model is not very accurate. Adding reflection (which is not present in the original model) does not improve the fit. Switching `compPS` to a spherical geometry does improve the fit slightly ($\chi^2_\nu = 84.9/80$). It results in parameters of $kT_{bb} = 0.15$ keV, $kT_e = 121.1$ and $\tau = 0.22$ (shown in figure 5.15).

Double Compton spectrum model

As we mentioned in chapter 3, curvature in an observed spectrum can be modelled by two Compton components. Using the same model with which we fit J1550–564,

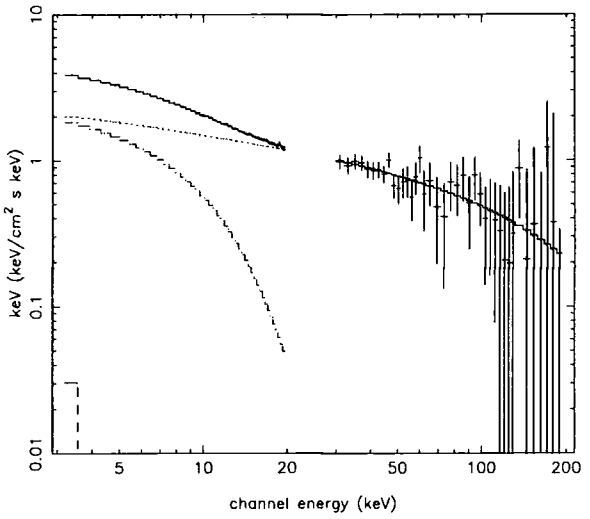

Figure 5.16: RXTE data is simulated from the output of the cylinder code at an inclination of $cos(\theta) = 0.625$. Fitting with a disk black body ($kT_{bb} = 0.17$ keV) and two Compton spectra achieves a fit of $\chi^2_\nu = 40.8/75$. The electron parameters are $kT_e = 998.0$ keV and 2.37 keV, the second of which is unusually low.

a fit of $\chi^2_\nu = 40.8/75$ is found (show in figure 5.16). This model contains a disk black body ($kT_{bb} = 0.17$ keV) and two (non reflecting) Compton tails at temperatures of $kT_e = 998$ keV and 2.2 keV. The second of these is a low, but not implausible, electron temperature (Życki, Done & Smith 2001). The spectral index of the two hard components is $\Gamma = 2.3$ which is reasonable for a very high state type spectrum. Once again the spectral curvature is modelled by an extra Compton component at low temperatures. Although the model fits well, there are not actually two Compton regions, nor even a hybrid plasma in the model which spawned the data. Models like this fit spectral curvature well but do not really explain its cause.

Clearly most models, if sufficiently free in parameter space, can be made to fit a spectrum of this sort, despite its complexity. In the example here, there was no reflection in our simulated data set, but the addition of reflection would only have worsened the situation. We cannot find accurate parameters for the continuum and so any parameters derived from reflection must be suspect.

In the RXTE energy range, the cylinder model produces a spectrum not unlike the very high state spectra of J1550–564 (figure 3.6). However, a broad bandpass spectrum would show significant differences between the two spectra. The cylinder model shows a large soft component (the disk emission) below our energy band. We

know from broad band data that this sort of feature is not generally seen in very high states (Ueda et al. 2002; Kubota et al. 2003). Similarly, data from OSSE shows the powerlaw extends to *very* high energy (γ–ray) regions (Grove et al. 1998). Our thermal spectrum rolls over sharply, a little above our energy range. Consequently, it seems unlikely that cylinder regions of the sort modelled here exist frequently in nature.

5.7 Summary

In recent years, models of Compton spectra have either been produced by probability based codes, or by making limiting approximations. We have shown that the computational power now exists to analyse the distribution functions directly. We have shown that it is possible to construct a model which has a fairly coarse angle grid but which can mimic the effects of an arbitrarily fine one. The method described here includes an inherent time dependence which shows how a system achieves steady state as well as the final spectra generated.

By using this model to simulate data from a thin cylinder, we have shown that many models can fit this sort of data without necessarily generating an accurate picture of the original system. It is clear that the limitations of the physical picture must always be taken into account when fitting data. Equally, broad band data can lower the possibility of models being easily fit to unsuitable data.

Chapter 6

Self Consistent Time Dependent Compton Scattering

6.1 Time dependence in single temperature codes

We have shown that our code can calculate steady state Comptonized spectra but this is a very inefficient method. Its key difference to previous Compton codes is the explicit treatment of time dependence. The spectra shown in chapter 5 are all generated by calculating photon transport over time. Consequently, the lightcurves are automatically generated by the calculation process. The behaviour of these lightcurves in simple situations is analytic and can be used to test the efficacy of the code in time dependent calculations.

The lightcurves shown in the left panel figure 6.1 are the $2-6$ keV (solid), $6-20$ keV (dashed) and $40-60$ keV (dotted) bands (normalized to their maximum value). They result from a calculation where the electron temperature was set at a constant value of 102.2 keV. These curves model the situation where photons with a black body distribution are continuously inserted into the system. Unsurprisingly the flux in each energy band starts off at a low level before saturating as the number of photons escaping the system equals the number of photons entering it. It takes more scatters for the photons to reach higher energies so the higher energy curves take longer to reach their maximum value.

Comparing our code with a theoretical prediction regarding time dependence requires a simpler input of photons. We model an injection of isotropic photons at an energy of 0.6 keV. The photons are added as an initial impulse and not replaced

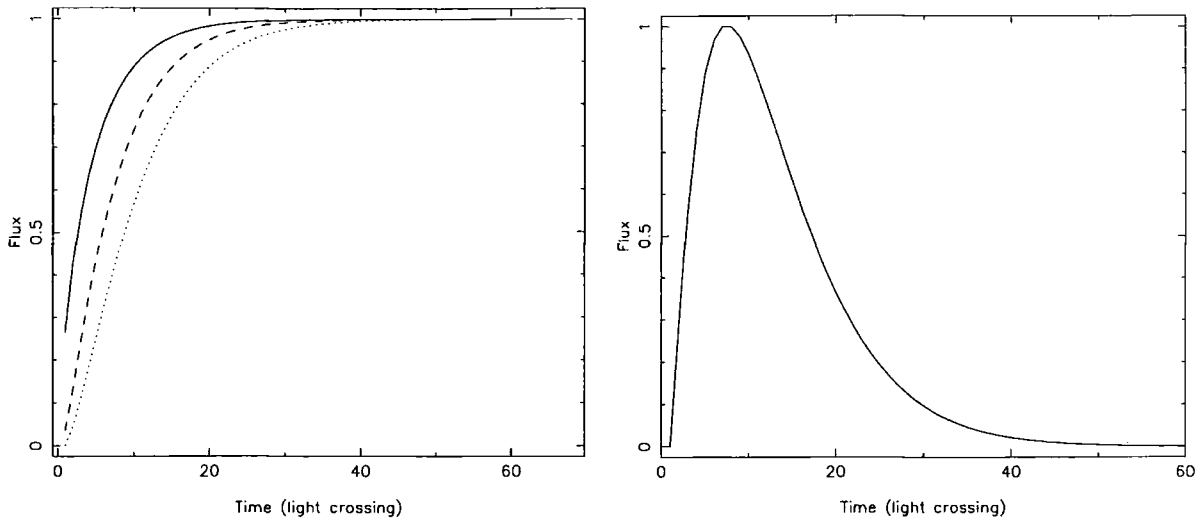

Figure 6.1: The lightcurves shown in the left panel are those from a single temperature calculation with the following parameters: $\tau = 0.1$, $kT_{bb} = 0.2$ and $kT_e = 102.2$. The three curves represent the $2-6$ keV band (solid), the $6-20$ keV band (dashed) and the $40-60$ keV band (dotted). The curves are each normalized to their maximum value. The right panel shows the temporal evolution of the 50 keV flux for an impulse of photons passed though a region of electrons at a constant temperature.

so they drain out of the system over time. The time profile of the output photons at any energy is analytic if the diffusion approximation holds (Payne 1980). The right panel of figure 6.1 shows the curve of the 50 keV flux. The flux of photons at 50 keV increases to a maximum as an increasing number of photons are Compton scattered to that energy. It then decreases as the number of photons in the system reduces (eventually to zero). The shape of this lightcurve is analytic when the optical depth is high and the electron temperature low (Payne 1980), however we are in conditions where the functional form for the curve cannot be used (Hua & Titarchuk 1996). The time, after the initial input, at which the maximum flux is reached is dependent on the energy of the photons. The approximation for this lag time is valid in the case when $4(9/4+4\alpha/y)^{-1/2}(lnE/E_i)^2 \gg 1$ (Payne 1980). For the energy range in which we are interested, this ranges from 50 to 2000 so we are able to use this equation. The relative time lag between the initial impulse and the peak time at a given energy is

$$\tilde{t}_{max} \propto \frac{1}{2}\left(\frac{9}{4}+\frac{4\alpha}{y}\right)^{-1/2} ln\frac{E}{E_i}$$

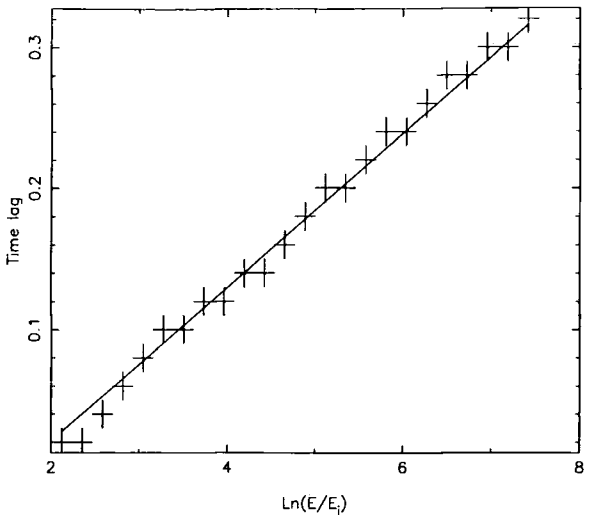

Figure 6.2: The time lags against the energy are given by an analytic linear equation, plotted as a solid line. The time lags, as calculated by our code, are shown as crosses. The two are clearly compatible.

where y is the Compton y parameter (in this case where τ is measured from the mid plane of our slab rather than surface to surface). The value of α depends on the geometry and is, in the case of a semi–infinite plane, equal to $\pi^2/12$, E is the energy of the output photons we are interested in and E_i is the starting energy of the photons. The timescale included in this calculation is defined

$$\tilde{t} = \frac{kT_e}{mc^2} N_e \sigma c t$$

Our code outputs in light crossing times so, in this specific example (where $kT_e/mc^2 = 0.2$ and $\tau = 0.1$), the relation is $\tilde{t} = 0.02 t_{cross}$.

Figure 6.2 shows the time lag (measured in $\tilde{t}$ against $ln\frac{E}{E_i}$). This is a linear equation with a predicted gradient of 0.0543 and the best fit to the data is 0.0573 ± 0.0021 ($\Delta\chi^2 = 2.7$). The figure shows the data plotted against the predicted gradient which is clearly within the error bars. Since the time dependence generated by the code is in agreement with theory, we can use it for more complicated systems.

6.2 Self consistent time dependence

The examples shown above and in chapter 5 treat the electrons as if they were heated from an infinite energy source, hence there is no change in electron temperature as

the photons scatter from them. Generating a time dependent model which takes account of electron temperature (a self consistent Comptonization model) is difficult because all the parts of a scattering system are interdependent. As photons pass through an electron cloud, they gain energy and cool the electrons. Some of the energy gained by the photons is then absorbed in the disk. It is re-emitted as low energy photons which further cool the electrons (Haardt & Maraschi 1993). Clearly, the amount of energy gained by the photons affects the amount of cooling once they have reprocessed. This sort of behaviour makes the timing and temperature properties of the system very complex, however we have developed a system to adapt the code shown in chapter 5 to model a self consistent system.

6.3 Obtaining physical normalizations

Until this point our normalizations have been arbitrary. The number of electrons cancels in the equations so our output normalizations have been a function of the number of photons generated by an un–normalized black body equation. Now that we wish to vary the energy in the electrons we need physical normalizations, so we use compactnesses. The other necessary input parameters are the optical depth per layer and the actual distance a layer represents.

We start by using the definition of the optical depth.

$$d\tau = N_{total}\sigma_T dR$$

From here we set a value for dR (the physical depth of one layer) and $d\tau$ and then calculate N_{total}.

$$N_{total} = \frac{d\tau}{dR\sigma_T}$$

Which is the total number density of electrons in a layer. We now use the definition of compactness, ℓ (from chapter 4).

$$\ell = \frac{U_{rad}}{m_e c^2}\sigma_T dR$$

Where dR is the same as in the definition of $d\tau$. By re-arranging we find that the photon energy density is

$$U_{rad} = \frac{\ell_{soft} m_e c^2}{\sigma_T dR}$$

Where ℓ_{soft} is the compactness of soft photons entering the system.

We can use the same logic to find the electron energy density from ℓ_{hard} (the electron compactness). This can be used as the amount of energy introduced into the electrons during each timestep (the energy injection rate). Since we also know the number of electrons in the system we can find their temperature (in the case of a thermal distribution). The photon energy density automatically gives us the number of photons required, because the photon black body temperature is an input of the system. For any black body

$$E_\gamma = U_{rad}/n = 2.73kT_{bb}$$

So

$$n_{phot} = \frac{U_{rad}}{2.73kT_{bb}}$$

6.4 Fast cooling times and electron recoil

A crude method by which we could model self consistent time dependence would be one where we develop a new electron temperature at the beginning of each timestep. We know the injection rate and we can find the energy loss from the electrons at the end of each timestep (it is equal to the energy gained by the photons). Subtracting these losses from the original electron energy and adding the new injected energy results in a new electron temperature which we can use in the subsequent timestep.

The danger in this method is that the energy loss could be sufficient to change the electron temperature significantly *within* the timestep. It is likely that in real systems the Compton cooling time is shorter than the light crossing time (Guilbert & Fabian 1982). In theory this means that energy is removed from the electrons so quickly that the injected energy is removed as soon as it arrives. Using the method outlined above, the result would be that more energy was lost than was in the electrons in the first place. To avoid this, we allow the temperature to change *during* the timestep.

6.4.1 Method of predicting the energy loss

This is achieved by using an approximation to predict the energy loss at any point within the timestep. The temperature of the electrons at a number of points can then be factored into a more accurate calculation carried out by the main code.

As a first step, we break each timestep into a number of smallsteps (initially 5). Since we know the energy injection rate, we can find the average electron energy during the first smallstep. This is equal to half the injection energy divided by the number of smallsteps (the half comes from the fact that we want the *average* energy in the smallstep, not the energy at the end of it). We then convert the average electron energy to a temperature and calculate the approximate photon energy gain at that temperature. This calculation involves interpolating over a grid of energy losses constructed using the steady state code. We start by finding the fractional photon energy gain for a single isotropic scattering at a particular input photon energy and electron γ. By constructing a grid containing these energy losses for a large number of combinations of photon energy and electron γ we can interpolate to any combination of particle energies (within the limits of our grid). We then step over each energy and γ in the photon and electron distributions, totalling the energy gain (taking into account the number of particles at each energy). Since the photon energy gain is equal to the electron energy loss, we remove that energy from the electrons and add the next smallstep injection energy. A new electron temperature is then found and we iterate until all the smallstep temperatures have been calculated.

The set of derived temperatures give us a good approximation to the energetic behaviour of the electrons throughout the timestep provided there are a sufficient number of them. Too few smallsteps results in the temperature not stepping smoothly across a timestep and so the predicted energy loss is compromised. In the event that the Compton cooling time is too short, one of the smallstep energy losses is greater than the total energy contained in the electrons. If this occurs, the number of smallsteps is doubled and the calculation is restarted. This continues until the smallsteps are shorter than the Compton cooling time.

Although we have only used this method to deal with thermal electron distribu-

tions, it can be generalized to any electron distribution. A non–thermal (powerlaw) distribution can be constructed from a series of δ functions and so an electron energy loss can be found.

6.4.2 From time dependence to multi–temperature scatterings

Having derived our temperatures in an approximate code, we need to use them in our non–angle averaged, accurate code. Clearly, we cannot break our timestep into shorter steps and use each temperature in each step. That would increase the run–time beyond all feasibility and would render the prediction pointless anyway.

We know that a fraction of the photons passing through the layer (equal to the reciprocal of the number of smallsteps) will encounter each electron temperature. A simple example of this can be seen if we had only two smallsteps. The first half of the photons would encounter the electrons at their initial temperature. However, by the time the second half arrive, the first half have already cooled the electrons to a lower temperature.

If we generate an electron distribution made up of several temperatures then the photons would encounter each possible temperature distribution in a single timestep. This allows us to use a multi-temperature scattering in the main code to accurately model a time dependent scattering, even if the Compton cooling time is short. For a thermal scattering the multi–temperature distribution is a sum of Maxwellians at each temperature. It is important to note that this still assumes a short thermalization timescale for the electrons.

To test that our predicted temperatures are accurate, we check that the total electron energy loss of the predictive code is within 10% of the value from the main code. We then take the *actual* energy loss and subtract it from the total amount of energy that was injected into the electrons. This gives us the correct electron starting temperature for the next timestep. Slight mismatches between the predicted and actual energy loss can lead to instabilities in the smallstep temperatures. Provided that the mismatch is not too bad, the instabilities do not become catastrophic. However, for ease of viewing, we quote all electron temperatures as

averages across each timestep.

6.5 Testing the time dependent code

To test this time dependent code, we introduce reprocessing. Previously, those photons which moved out of the bottom layer of the system were lost. Now, they interact with the photon producing region (the disk) and return. We use the reflection code of Magdziarz & Zdziarski (1995) and assume that the disk has standard abundances, so disk ionization is the only new parameter introduced. Only a fraction of the incident photons are actually reflected. The rest (which are absorbed) are reprocessed into the next incident blackbody. We calculate the total energy of the incident photons that are reprocessed and find the number of photons (at the black body temperature, kT_{bb}) which would carry that much energy. That number of photons are added to the new photon distribution which enters the first layer from the disk.

If the disk is contiguous with the Comptonizing region, reprocessing happens throughout the timestep. To model such a system would require us to factor the reprocessed photons into our smallstep temperature predictions. This is a complex process so, instead, the reflected photons from one scattering are added at the beginning of the next timestep. As a result, the minimum distance between the disk and the hot electron region that we can model is $dr/2$ (because it takes one timestep for the photons to reach the disk and return). If we wished to model a larger distance we could put a delay on the number of timesteps before the reprocessed photons return.

By setting $\ell_h = 0.5$ and $\ell_s = 0.02$ we model a reprocessing dominated situation, which settles to a well known temperature. As the temperature in the electrons increases, more high energy photons are produced. These encounter the disk and are reprocessed driving up the soft flux. Consequently, the rate of cooling increases and the electron temperature is pulled down. This puts a limit on the highest possible steady state electron temperature, and so also on the lowest achievable spectral index (Haardt & Maraschi 1993). The predicted temperature that a non-ionized system with an optical depth of $\tau = 0.1$ and a black body temperature of

$kT_{bb} = 0.05$ will reach is $kT_e \sim 250$ keV (Haardt & Maraschi 1993). When allowed to reach a steady temperature, our code settles to a value of $kT_e = 246$ keV showing that our electron cooling routine works.

6.6 The change in electron parameters over time

Two low optical depth codes ($\tau = 0.1$) were run to see the change in the electron temperature in a reprocessing dominated system as time progressed. Using the same compactnesses as before but with a photon temperature of $kT_{bb} = 0.2$ we ran codes with ionization parameters of $\xi = 10^{-6}$ and $\xi = 10^{6}\,\mathrm{ergss^{-1}cm}$.

6.6.1 Reflection from a neutral disk

The final spectrum and temperature curve for the first case (low ionization) are shown in the left panels of figures 6.3 and 6.4. The system we are modelling starts with very little soft flux and a lot of energy being injected into the electrons so we expect the temperature to rise during the first few scatters. After a short time, the large amount of energy that is being reprocessed by the disk starts to have a significant effect on the electron temperature. The electrons cool as the energy lost is greater than the energy injected. An equilibrium is reached when the energy loss to the photons is equal to the energy injected into the electrons. We are using a slightly higher black body temperature than in the previous section, so we should expect a slightly higher settling temperature. The black body photons will remove less energy from the electrons so the equilibrium temperature will be higher. Figure 6.4 shows this temperature to be $kT_e = 280$ keV. The system has basically reached its equilibrium temperature within 20 light crossing times showing how quickly a steady state can be established.

The final spectrum looks very much like a single temperature scattering from an electron temperature of 280 keV. Clearly, the high energy photons generated in the early stages of the code have exited the system before stability was reached. This is necessitated by our stopping condition that no net energy exchange must take place.

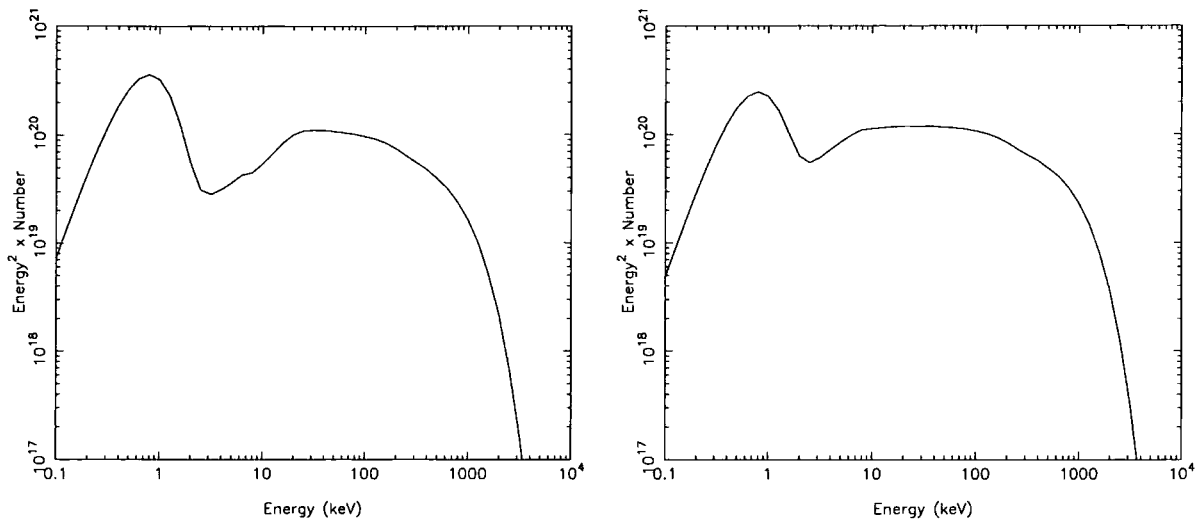

Figure 6.3: These are the final spectra resulting from a planar system. Left panel: $\tau = 0.1$, $\ell_h = 0.5$, $\ell_s = 0.02$ and $\xi = 10^{-6}$. Right panel: $\tau = 0.1$, $\ell_h = 0.5$, $\ell_s = 0.02$ and $\xi = 10^6$.

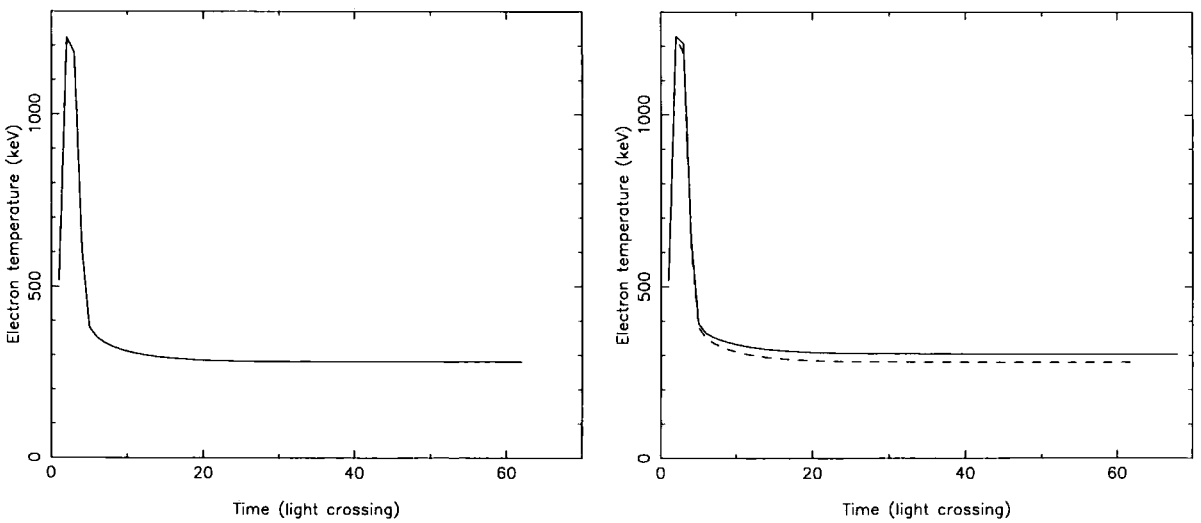

Figure 6.4: The change in electron temperature over time from a slab. Left panel: $\tau = 0.1$, $\ell_h = 0.5$, $\ell_s = 0.02$ and $\xi = 10^{-6}$. Right Panel: $\tau = 0.1$, $\ell_h = 0.5$, $\ell_s = 0.02$ and $\xi = 10^6$. The temperature curve of the neutral reflection case is shown for comparison (dashed line).

6.6.2 Reflection from a highly ionized disk

The relative amounts of reflection and reprocessing of the photons incident on the disk, depends on the ionization state of the disk and the spectral index of the illuminating flux. Figure 6.5 shows the neutral and fully ionized albedo as the spectral index changes. The solid line is for a powerlaw incident spectrum with no high energy roll–over and the dotted lines for a powerlaw with a roll–over at 200 keV. Whatever the spectral index, there is an increase in albedo as the disk becomes ionized. A fully ionized reflected spectrum has no photo–electric absorption at low energies and so reflects a larger amount of photons than a neutral spectrum. Although the albedo changes significantly as the disk ionization increases it is clear that, for hard spectra, there is a limit on how much it can change. In the case of neutral reflection, very few low energy photons are reflected. For hard spectra most of the energy is contained in photons above $\sim$ 50 keV, but these photons are not reflected elastically so the albedo is around 40%. However, in soft spectra, most of the energy is contained in the low energy spectral region where very little reflection occurs. Consequently the neutral albedo is lower in softer spectra. Changing the ionization state of a disk only changes the reflected spectrum at energies lower than $\sim$ 50 keV. This makes very little difference to the hard spectra as the reflection properties do not change at the important temperatures ($>$ 50keV). However, in soft spectra, the photons at low energies (where most energy resides) now nearly all reflect whereas they were nearly all absorbed before. This leads to a large change in albedo. For the very hardest spectra, ionizing the disk makes no significant difference to the albedo at all so the albedo is not a free parameter in spectral fitting.

In neutral spectra (low albedo) reprocessing means that there are lots of low energy photons available to cool the hot electrons. In an ionized disk (higher albedo), there are less low energy photons to cool the electrons so the equilibrium temperature is higher. The final spectrum and temperature curve for self consistent scattering with reprocessing from a highly ionized disk are shown in the right panels of figures 6.3 and 6.4. As in the low ionization case, the electron temperature rises and then drops as reprocessing becomes important. The difference caused by

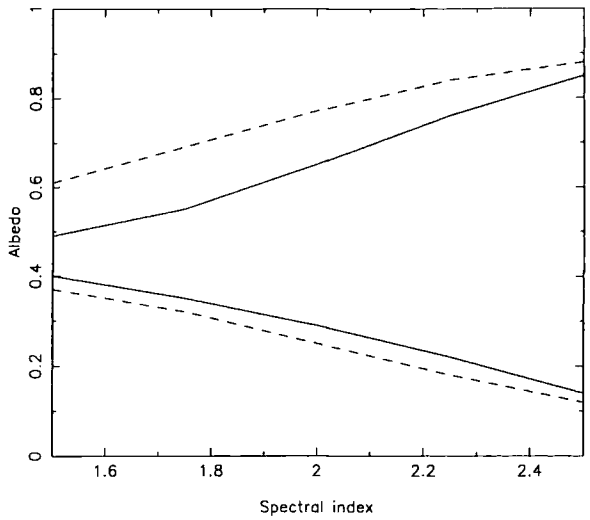

Figure 6.5: The albedo of a disk is dependent on its ionization state and the spectral index of the illuminating flux. In this plot the solid lines represent the neutral (lower) and ionized (upper) albedo from a disk being illuminated by a single powerlaw. The dashed lines represent a disk being illuminated by a powerlaw with a roll–over at 200 keV. Changing the ionization state of the disk does not have a large effect in hard spectra.

ionization is demonstrated by the final temperature settling to a value of 304 keV rather than the neutral disk value of 280 keV. The spectral index is reasonably flat so there is only a small increase in albedo and, consequently, a small decrease in reprocessed flux.

Despite the fact that the temperature (and hence y parameter) is higher, the index of the ionized spectrum (right panel of figure 6.4) *appears* steeper than the index of the neutral spectrum (left panel). This is not caused by any intrinsic change to the Compton spectrum but is a reflection effect. In the neutral spectrum the reflected curve is the same as that shown in figure 2.5 so the Compton hump is significantly flatter than the intrinsic spectrum. The ionized reflection spectrum below 20 keV is dominated by scattering and so has the same spectral index as the incident spectrum (see figure 2.8). Consequently, when ionized reflection is added to the Compton spectrum there is no change in spectral index.

6.6.3 Spatial variation of electron temperature

We would expect the temperature in a slab to increase from the disk surface to the slab boundary. Most models of Compton scattering assume that the scattering medium has a single temperature which describes the entire region. This cannot be the case, however, as the number of cool photons in any scattering system will decrease as photons are scattered to higher energies. With fewer cool photons, the electrons have less opportunity to scatter, lose energy and so maintain a higher temperature. Since the number of cool photons decreases towards the top of a slab system, we would expect the temperature to increase with height. This is most noticeable in optically thick systems but will occur in optically thin ones too. This effect has been computed using a Monte–Carlo code (Dove, Wilms & Begelman 1997).

Because the code breaks the scattering region into independent layers, we can model this multi–temperature behaviour. To show this, we run a code similar to the neutral reflection code shown above. Instead of using a single layer of $\tau = 0.1$, we use two layers, each of $\tau = 0.05$. In principle, the results should be identical but now the layers will settle to two different temperatures, resulting in a more complex behaviour.

Halving the standard layer size has several side–effects which must be considered. We generate the normalizations from the compactnesses and optical depth, so it is vital that the same normalizations are used. To maintain the same *physical* region size, we halve the layer depth. Our compactnesses also refer to a single layer, not the whole system, and so these also need to be halved to maintain the same number density of photons and electrons. However, by halving our layer size, we have halved the light crossing time of a layer (but not of the system). Consequently, we are now sampling over time twice as often as before. Our compactnesses are used to generate an energy input *rate*, dE/dt. It is this rate that must be kept constant, requiring another division by 2 for both the soft and hard compactness (since the soft compactness is a rate of injection from the disk into the bottom layer). Therefore, the final parameters are $\xi = 10^{-6}$ and $kT_{bb} = 0.2$ keV and, for each layer, $\ell_h = 0.125$ and $\ell_s = 0.005$.

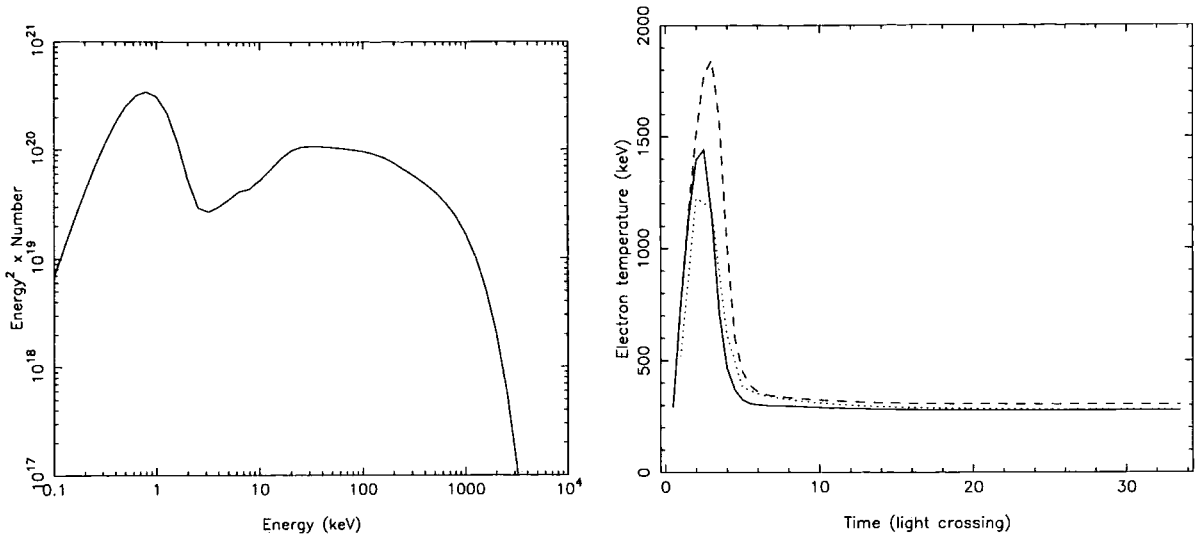

Figure 6.6: The spectrum and temperature change over time from a two layer system ($\tau = 0.1$, $\ell_h = 0.125$, $\ell_s = 0.005$ and $\xi = 10^{-6}$). The solid temperature line is that from the lower layer and the dashed line is that from the higher. The dotted line is the temperature profile from a single layer system with the same normalizations. The light crossing time is for the whole system (twice that for one layer) and so is the same as that used for figure 6.4.

The spectrum and temperature distribution is shown in figure 6.6. In a system with such a low optical depth the variation in temperature with depth is quite small. The lower layer settles to a temperature of 278 keV and the higher layer to a temperature of 305 keV (as opposed to 280 keV for a single layer). The reflected photons travel first through the lower layer where they gain energy. There are then fewer soft photons to cool the upper layer so that layer peaks and settles to a higher temperature. The upper layer also peaks slightly later as it takes more time for the reflected photons to penetrate and cool that layer. The fact that both layers have clearer peaks than the single layer temperature curve (dotted line in figure 6.6) is a result of the increased sampling rate.

6.6.4 Lightcurves from self consistent Comptonization

Again, we can use the inherent time dependence of our method to investigate the behaviour of the system as it reaches stability. Figure 6.7 shows the lightcurve from the 2 layer system outlined above. The bands are $2 - 6$ keV (solid), $6 - 20$

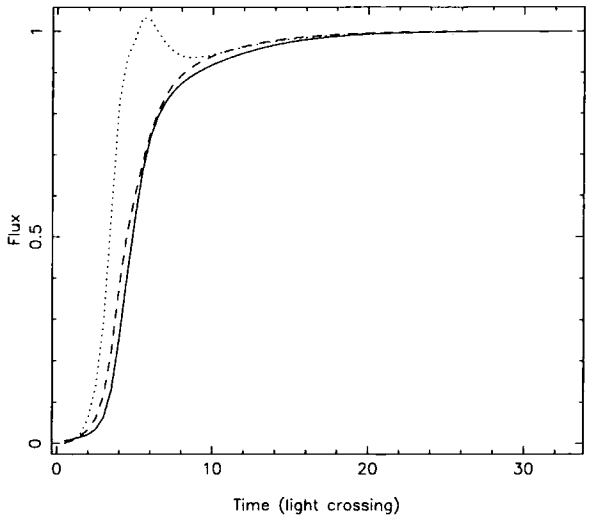

Figure 6.7: Lightcurves from a two layer system ($\tau = 0.1$, $\ell_h = 0.125$, $\ell_s = 0.005$ and $\xi = 10^{-6}$). The bands shown are $2 - 6$ keV (solid), $6 - 20$ keV (dashed) and $40 - 60$ keV (dotted). The high energy line shows a peak from the associated peak in electron temperature.

keV (dashed) and $20 - 40$ keV (dotted) and are normalized to their steady state value. Unlike the lightcurves from the fixed electron temperature (no reprocessing) situation (shown in figure 6.1) there is an unusual feature in the $40 - 60$ keV band. It takes some time for the reflected photon flux to cool the electrons so the electron temperature reaches high levels in the first few light crossing times. The resulting spectrum has a very flat index as the y parameter is large. This results in a peak in the hard X–ray band. After a short time, the temperature (and y parameter) settles to lower values and the three curves reach a stable situation shortly after.

6.7 Timing behaviour of observed Comptonizing sources

6.7.1 Time lags: Discovery

The observed spectra from compact objects show very complex timing behaviour. There have been many investigations into the timing behaviour of X–ray sources (*e.g.* Weisskopf, Kahn & Sutherland 1975; Sutherland, Weisskopf & Kahn 1978; Preidhorsky et al. 1979; Nolan et al. 1981; Miyamoto et al. 1988; Miyamoto &

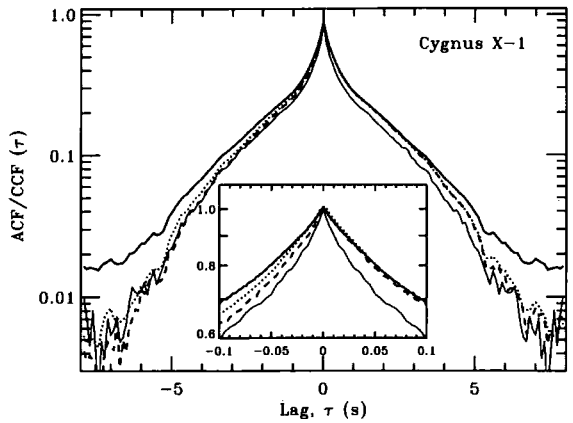

Figure 6.8: The auto and cross–correlation functions of the December 1997 observation of Cygnus X–1. Solid curves show the ACFs for the $2-5$ keV band (thick) and the $24-40$ keV band (thin). Dotted curves show the CCF between the $8-13$ keV band and the $2-5$ keV band and dashed curves, the CCF for the $24-40$ keV band and the $2-5$ keV band. The peaks align around zero lag but it is impossible to resolve short lags on a linear scale. Taken from Maccarone et al. (2000).

Kitamoto 1989; Miyamoto et al. 1991; Cui et al. 1997; Nowak et al. 1999). The auto–correlation functions of the lightcurves of several objects reveal correlation over a large timescales. Figure 6.8 show the auto and cross–correlation functions of the December 1997 observation of Cygnus X–1 (Maccarone, Coppi & Poutanen 2000). The solid curves show the ACFs for the $2-5$ keV band (thick) and the $24-40$ keV band (thin). The dotted curves show the CCF between the $8-13$ keV band and the $2-5$ keV band and dashed curves, the CCF for the $24-40$ keV band and the $2-5$ keV band. The peaks align around zero lag and show correlation of up to 5 seconds which is far longer than the light crossing or Keplerian orbit timescale in a disk.

Detailed cross–correlation of different energy bands show that hard energies tend to lag behind softer bands (called a hard lag). Hard lags follow logically from the fact that is takes more scatterings for photons to achieve a higher energy and so such photons take a correspondingly longer time to leave the system (Payne 1980). However, the exact energy dependence predicted by Comptonization and the timescale of the lags is not in good agreement with observations (Cui et al. 1997; Crary et al. 1998, Nowak et al. 1999).

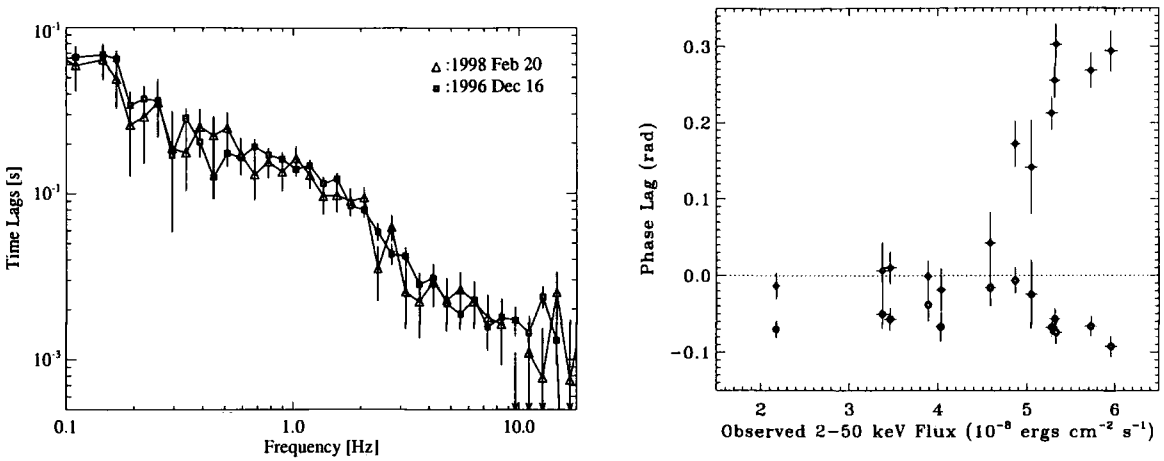

Figure 6.9: Left panel: The lags from 1998 and 1996 observations of Cygnus X–1 are shown. The correlation was taken between energies $\leq$ 4 keV and the 8 – 13 keV band. The frequency dependence of the lag is clearly shown. Taken from Pottschmidt et al. 2000. Right panel: The soft and hard lags detected at the QPO frequency (filled) and first harmonic (open) during the rise phase of the 1998 outburst of J1550–564. The lags are shown changing with flux as the outburst progressed (Taken from Cui et al. 2000 where the lags are expressed in phase rather than time (*i.e.* $t = \phi/2\pi f$).)

Miyamoto et al. (1988) showed that the lags were dependent on Fourier frequency which is difficult to justify by Comptonization. The left panel of figure 6.9 shows the lags from 1998 and 1996 observations of Cygnus X–1. The correlation was taken between energies $\leq$ 4 keV and the 8 – 13 keV band. The frequency dependence of the lag is clearly shown (taken from Pottschmidt et al. 2000). These lags are typical of the hard state of Cygnus X–1. There is some evidence that lag behaviour changes during state transition but is essentially similar at other times (Pottschmidt et al. 2000).

However, data containing strong QPOs (*e.g.* GRS 1915+105 and J1550–564) tend to show soft lags (Cui 1999; Wijnands, Homan & van der Klis 1999; Reig et al. 2000; Cui, Zhang & Chen 2000). As we showed earlier (figures 6.1 and 6.2) in Comptonization we expect the hard X–ray band to lag a short time behind the soft X–ray band (Payne 1980; Hua & Titarchuk 1996). Therefore, soft lags run counter to the expected behaviour of sources which are undergoing simple Comptonization. The right panel of figure 6.9 shows the soft and hard lags detected at the QPO

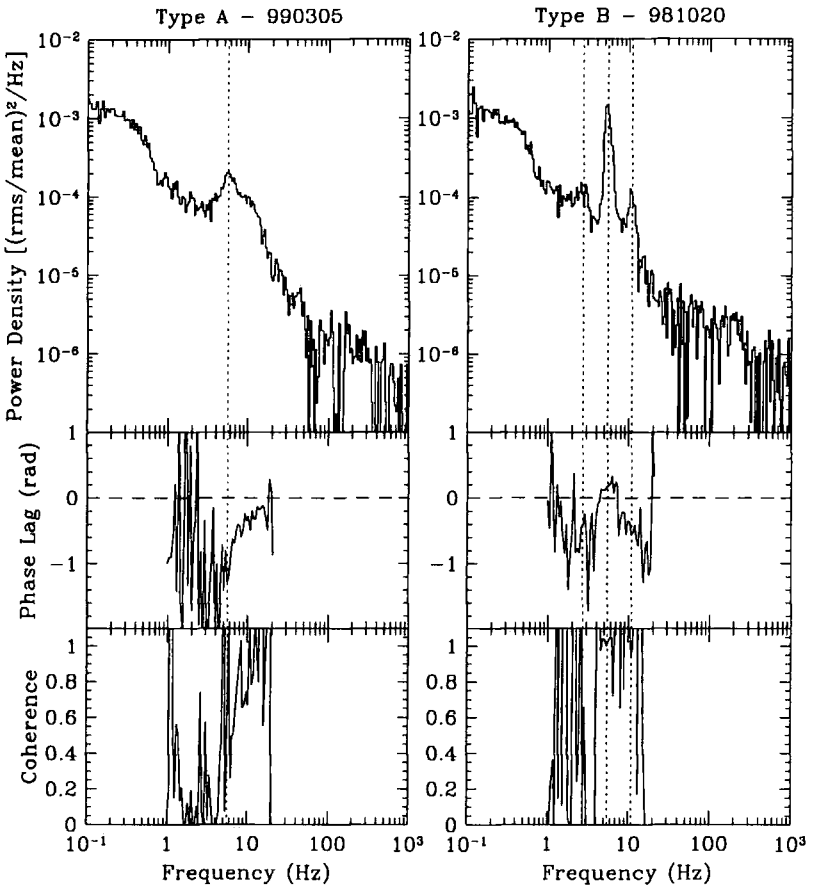

Figure 6.10: The power spectrum, lag and coherence function for QPOs from J1550–564. The lags and coherence are found from the 2 – 13 keV and 13 – 30 keV bands. The lags are generally soft (negative) around the QPO frequencies (or around the harmonics). Taken from Remillard et al. 2002

frequency during the rise phase of the 1998 outburst of J1550–564. The lags are shown changing with flux as the outburst progressed. This is taken from Cui et al. 2000 where the lags are expressed in phase rather than time (*i.e.* $t = \phi/2\pi f$). Figure 6.10 (taken from Remillard et al. 2002) shows the power spectrum, lag and coherence function for QPOs from J1550–564. The lags and coherence are found from the 2 – 13 keV and 13 – 30 keV bands. The lags are generally soft (negative) around the QPO frequencies (or around the harmonics).

6.7.2 Time lags: Proposed solutions

Comptonization within large coronae has been suggested as a mechanism for generating the long lags (Payne 1980) and the observed Fourier dependence of the lags could be produced from a non–uniform density distribution (Kazanas, Hua & Titarchuk 1997). The long lags in these models are attributed to photons travelling large distances so shorter lags are produced in the central (more dense) region of the cloud. However, the variability predictions of this model do not match the observations (Nowak et al. 1999). These models can also only explain the hard lags.

A hot inner disk (*e.g.* an ADAF) in which soft photons are produced by cold matter passing through has also been suggested (Böttcher & Liang 1999). Hard lags can be generated by the increasing amount of seed photons as the cold matter drifts inwards. However, the model relies on a change in local energy dissipation rate as the cold matter moves through the hot, inner region and the physical likelihood of this occurring is still in some doubt (Poutanen 2001).

Evolving magnetic flares are quite popular as a method of generating hard lags (Haardt, Maraschi & Ghisellini 1994; Stern et al. 1995b; Poutanen & Svensson 1996; Beloborodov 1999; Poutanen & Fabian 1999). These models often use the local Keplerian timescale for the flare timescales and allow the magnetic corona to move away from the disk. This alteration of energy dissipation rate and local geometry can generate the observed hard lags by allowing the spectrum to harden over time (Poutanen & Fabian 1999). The model can also generate high frequency soft lags (Malzac & Jourdain 2000) for very rapid electron flares (timescales comparable with the light crossing time). Fine tuning the parameters of the flare (including bulk motion) can match the observed data for Cygnus X–1 well.

Reflection has also been put forward as a mechanism for generating long, hard lags. Using the light travel time between the hot cloud and far regions of the disk, long lags can be generated. They are believed to be hard as the reflection is generally harder than the incident spectrum. However, the energy dependence of the lags is not well matched and reflection from very large distances is unlikely to have a significant effect. For a review of the models of timing behaviour, see Poutanen 2001.

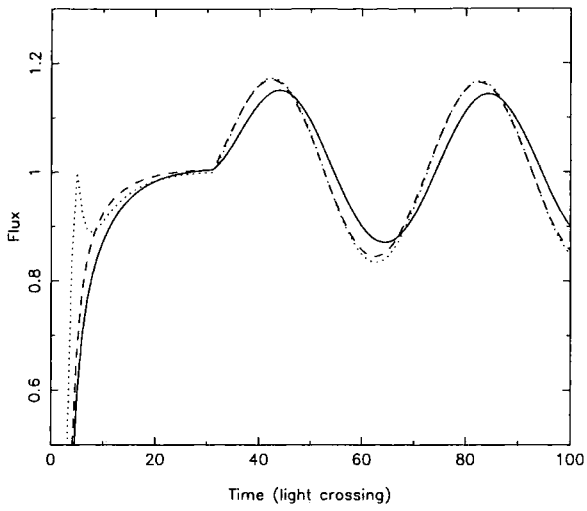

Figure 6.11: The lightcurve from a system ($\tau = 0.1$, $\ell_h = 0.5$, $\ell_s = 0.02$ and $\xi = 10^{-6}$). The bands shown are $2 - 6$ keV (solid), $6 - 20$ keV (dashed) and $40 - 60$ keV (dotted). The energy injection rate (ℓ_h) is varied by 20% in a *sin* wave pattern with a period of 40 light crossing times. The softest energy band lags behind the two harder X–ray bands.

6.7.3 Modelling lags through changing hard compactness

The idea that soft lags are inconsistent with simple Comptonization is a natural result of the assumption that it is the level of soft photon input which is adjusting. However, if it were the rate at which energy is injected into the electrons which was changing then the system is considerably more complex. As time progresses, each scattering order will have input photons which have already scattered off electrons of a different temperature. The reprocessed soft photon flux would naturally lag behind a change in the injection rate as the energy would have to leave the medium, reprocess and return.

We model a situation where the electron injection rate is changing over time using the slab geometry. Initially, the same parameters as the single layer code above are used ($\tau = 0.1$, $\ell_h = 0.5$, $\ell_s = 0.02$ and neutral reflection). The hard compactness is kept constant for 30 scatters to allow the system to reach stability (at which point the electrons have a temperature of 290 keV). We then use a *sin* wave (with an amplitude 20% either side of the initial value) to model a simple change in compactness. For the lightcurves, we use the same energy bands as before ($2 - 6$ keV, $6 - 20$ keV and $40 - 60$ keV).

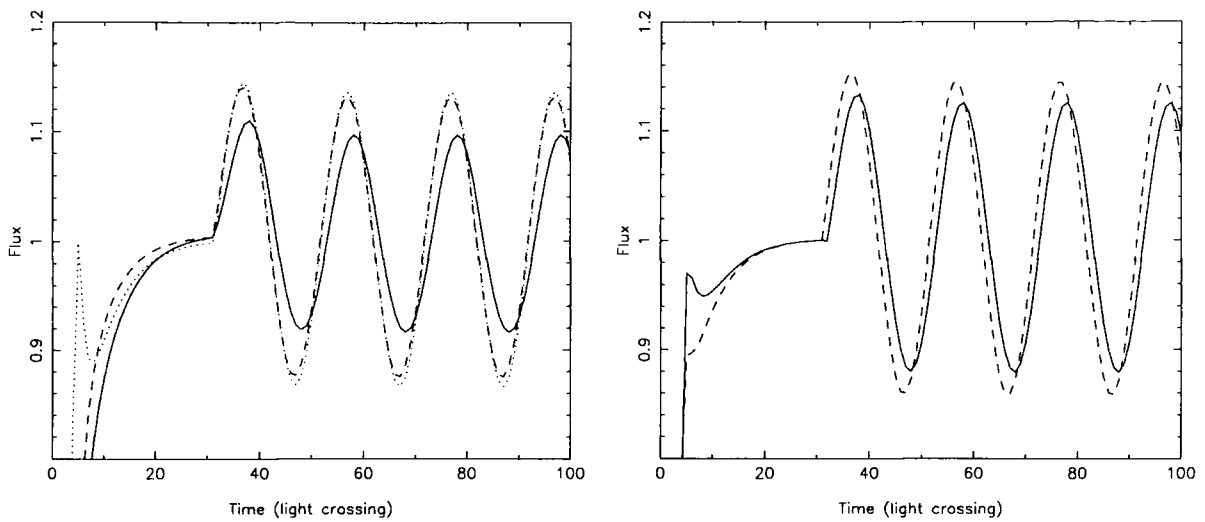

Figure 6.12: The lightcurve from a system ($\tau = 0.1$, $\ell_h = 0.5$, $\ell_s = 0.02$ and $\xi = 10^{-6}$). The energy injection rate (ℓ_h) is varied by 20% in a *sin* wave pattern with a period of 20 light crossing times. Left panel: The bands shown are $2 - 6$ keV (solid), $6 - 20$ keV (dashed) and $40 - 60$ keV (dotted). The softest energy band lags behind the two harder X–ray bands and the peak change in flux is dependent on energy. Right panel: The same system is shown with energy bands $0.1 - 2$ keV (solid) and 2 keV – 10 MeV (dashed).

As can be seen from figure 6.11, a variation of the compactness over long timescales (in this case 40 light crossing times for a complete *sin* wave) results in a soft X–ray lag. Even though the injection of energy into the electrons is varying by 20%, the variation of flux (relative to each band's maximum value) is less and is a function of the energy: 16% in the hard bands and 14% in the soft. The hard energy bands show no detectable lag with the input energy change whereas the soft bands are one light crossing time behind. We find similar results if we shorten the timescale of the variation. This can be seen in the left panel of figure 6.12 where a complete *sin* wave occurs in 20 light crossing times. The lag time in this case is the same (one light crossing time) although the fractional change in flux is dampened by the increase in frequency of injection energy (13% hard and 9% soft).

A close examination of the system reveals the cause of the soft lag and energy dependent fractional change. As the electron injection rate is increased, the scattered spectrum follows closely. The first scattering order always scatters photons from the black body which are always at the same energy. Consequently, the energy band containing this scattering ($6 - 20$ keV) only moves a small fraction as the electron

temperature changes. However, the photons in the first scattering order (which are at a higher energy) then become the input photons for the next scattering. There are now two effects: a higher starting energy and a higher electron energy, so the higher scattering orders increase by a greater fraction than the lower ones.

A fraction of the Compton scattered spectrum interacts with the disk and reprocesses. Once it arrives back in the scattering system, it boosts the soft photon (black body) flux. As the electron energy increases, the Compton scattered spectrum contains more energy. Consequently, more energy is reprocessed and the soft photons increase in flux. There is an inherent time delay in this picture as the photons have to travel to the disk and back, which will always take at least one light crossing time. In systems where the disk is a longer distance from the Comptonizing region, the time lags would be longer. This lag is seen in the $2-6$ keV band which contains some photons from the black body as well as the first scattering. To resolve this lag more clearly we can use new energy bands. The right panel of figure 6.12 shows lightcurves when the energy bands are $0.01-2$ keV (the black body, solid) and 2 keV – 10 MeV (the Compton tail, dashed). When the change in electron energy occurs on such a long timescale there is not much change between the two pictures except that the percentage change in flux is about equal in the two bands. The lag is still clear at one light crossing time. The clearest change is at the point where the energy injection rate changes. Previously, there was a visible change in the $2-6$ keV band at the earliest times as its high energy end was affected by the change in injection rate. In the new plot, the low energy band does not change until one timestep later, showing the lag clearly.

If we shorten the timescale even further (down to 6 light crossing times for a complete *sin* curve) the problem of using arbitrary energy bands becomes more serious. The left panel of figure 6.13 shows the output from such a system in the 3 original bands. Again the percentage change is smaller than before (7% and 3%) but any lag is not clear. The electron injection rate is moving so fast that the lag (which takes place at the low end of the $2-6$ keV energy band) is being counter–acted by movement in the rest of the band. This will always occur when the lag timescale is comparable to the timescale of the parameter change. The right panel shows the lightcurve from the system with the energy bands defined by the black body and

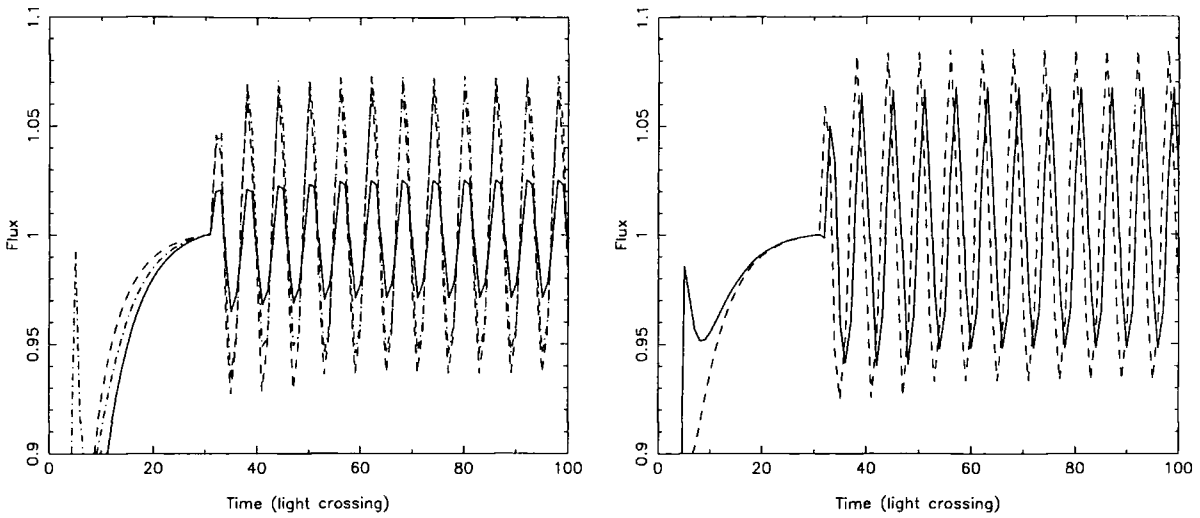

Figure 6.13: The lightcurve from a system ($\tau = 0.1$, $\ell_h = 0.5$, $\ell_s = 0.02$ and $\xi = 10^{-6}$). The energy injection rate (ℓ_h) is varied by 20% in a *sin* wave pattern with a period of 6 light crossing times. Left panel: The bands shown are $2 - 6$ keV (solid), $6 - 20$ keV (dashed) and $40 - 60$ keV (dotted). The peak change in flux is dependent on energy but any lag is difficult to resolve. Right panel: The same system is shown with energy bands $0.1 - 2$ keV (solid) and 2 keV – 10 MeV (dotted). The lag is clearer in this situation as the spectrum has been decomposed into the two spectrally separate regions.

Compton spectrum. The lag is now perfectly clear (again one light crossing time) because we have untangled the rapid shifting of the Compton tail from the shifting of the black body. The early peak in the low energy band is the reprocessed energy from the peak in the highest bands that was seen earlier.

Fortunately, a situation where such rapid changes occur is very hard to achieve in nature. The parameters of the system can only change on the light crossing time so to move the electron temperature this fast would be difficult.

This model involves no bulk motion of the electron region and does not require complicated input parameters. A simple time dependent model of Compton scattering, which includes reprocessing, automatically results in soft lags on roughly the scale of the light crossing time. We would expect longer lags if the reprocessing region were further from the disk. Lags such as this should be seen in all sources where the seed photons are formed predominantly from reprocessing of the hard X–ray flux. However, these lags do not vary with frequency and are not hard lags (which are observed most often) so this mechanism cannot be the only (or even the

main) source of the observed timing behaviour.

Interestingly, we would expect a similar effect if the optical depth were to be adjusted with time. Rather than changing the maximum energy of each scattering, the number of scattered photons would change. This would lead to a similar increase in hard flux which would be followed by an increase in soft flux as the energy was reprocessed. Although there would be little difference in the timing behaviour of these two cases there would be clear spectral differences which could be used to differentiate between them.

6.7.4 Lags in non–reprocessed systems

Any reprocessing system should generate soft lags on a short timescale. To establish that these lags vanish when there is no reprocessing we modelled a similar system without reflection. We used the single temperature code described in chapter 5 with the same parameters ($\tau = 0.1$ and $kT_{bb} = 0.2$ keV). This code does not use compactnesses so we set the electron temperature directly. Initially, we used a temperature of 281.0 keV, which is the settling temperature for the neutral, reprocessing dominated code when $\ell_h = 0.5$. Once the spectrum had settled (after 40 scatters) we vary the temperature as a *sin* wave with a period of 20 scatters. The amount of temperature variation was set to be identical to that which would result from a 20% variation in compactness (this involved inverting the compactness–average energy–temperature relation). A 20% change results in a variation of ± 48 keV (17%).

The results, shown in the left panel of figure 6.14 show a clear difference to the reprocessed case. There is now a hard lag that increases with energy, one light crossing time between the $6 - 20$ keV and $2 - 6$ keV bands and two between the $40 - 60$ keV and $2 - 6$ keV bands. Even though the electron temperature changes instantaneously, the lower order scatterings peak first. Once a high temperature scattering has taken place, the lower order photons (which are now at a higher energy than normal) are the seed photons for the higher order scatterings. Consequently, the higher orders peak later as the highest temperature first order scattering propagates through the system. This lag could be compromised if the

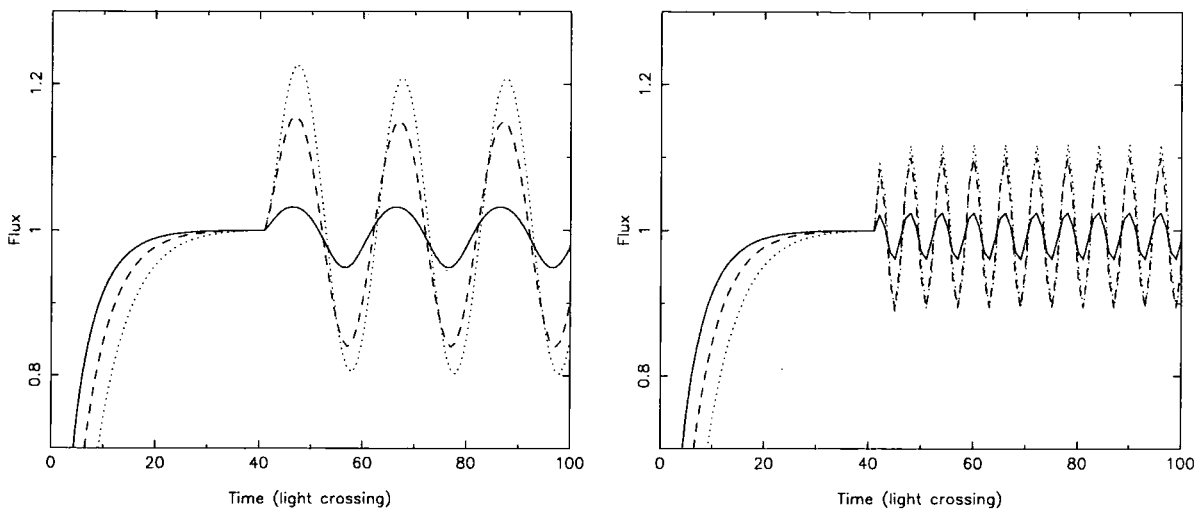

Figure 6.14: The lightcurve from a system ($\tau = 0.1$, $kT_{bb} = 0.2$ keV and $kT_e = 281$ keV). Left panel: The electron temperature (kT_e) is varied by 17% (equivalent to varying ℓ_h by 20%) in a *sin* wave pattern with a period of 20 light crossing times. The bands shown are $2-6$ keV (solid), $6-20$ keV (dashed) and $40-60$ keV (dotted). The peak change in flux is dependent on energy and the harder scattering orders lag behind the softer ones. Right panel: The same parameters and variation are used with a *sin* wave period of 6 light crossing times. The energy dependence is still clear (although of lower value) but the lag is smeared by the fast temperature variation time.

timescale of electron temperature variation were short enough. If it were comparable with the timescale necessary for photons to scatter to the highest orders the temperature could have dropped significantly before the high energy seed photons were scattered. This is demonstrated in the right panel of figure 6.14 where a 6 light crossing time period has been used. The energy dependence remains (although the percentage change has dropped) but the lag has been lost.

The fractional change in the light curve is also dependent on energy (Right panel of figure 6.14: 3% in the $2-6$ keV band, 15% in the $6-20$ keV band and 20% in the $40-60$ keV band). This is because the change in electron temperature is cumulative with scattering order. The first order only increases by a small amount as it uses black body temperature (kT_{bb}) seed photons. However, the second scattering order has a higher electron temperature *and* higher temperature seed photons and so increases by a large amount. This effect is cumulative with scattering order, leading to large changes in the high energy lightcurve.

6.8 Summary

By using a code of the type discussed in chapter 5 it is comparatively easy to investigate time dependent Compton behaviour. Electron cooling introduces problems of maintaining self consistency. These can be overcome by using a predictive method to resolve the average electron temperature on times smaller than the light crossing time. An accurate scattering can then be modelled as a scattering by a multi–temperature plasma.

A self consistent, time dependent code can include reprocessing from the disk and can be used to investigate the change in electron temperature both spatially and temporally within a scattering region. The dependence of the cooling rate on disk ionization can also be examined.

The timing behaviour of the Compton spectrum is comparatively simple to model. When the electron compactness changes with time, delayed reprocessing from the disk results in a *soft* lag. The length of this lag is set by the distance of the disk from the hot electron cloud. This lag can be difficult to resolve if the energy bands are not matched to the spectral shape. This becomes especially true if the

reprocessing time is comparable to the timescale of the change in kT_e. Modelling changes in the electron temperature without reprocessing results in a hard lag, which is expected from Compton theory. It seems likely that the observed short time lags result from changes in the disk and electron parameters which propagate via scattering and reprocessing. Longer lags (which are on timescales far greater than the scattering or Keplerian time) are more likely to be a result of overall spectral evolution caused by wide ranging changes in source structure.

Chapter 7 | *Further work*

7.1 Timing properties

We have only touched the surface of the timing properties that could be investigated by this code. Since our cooling approximation can be applied to any electron distribution, we can model the time lags that would result from changes in a non–thermal or hybrid plasma just as easily. In a non–thermal electron distribution, changes in γ_{max} or the powerlaw index can have profound effects on the spectrum.

Since reprocessing is the key to the lags that we have modelled, an investigation of the effects of changing the reprocessing region would be productive. If the region was further away, we would expect the lags to be longer, but perhaps there would be interference as the lag time and energy injection change timescale become similar. Equally we can model reprocessing from several regions at different distances and ionizations.

A further step would be to model an energy input which modulates over many frequencies and has an associated power spectrum. The resulting outputs would show the filtering properties of the corona and could be used to investigate the effects of Comptonization on QPOs and other timing features.

7.2 Electron heating mechanisms

Apart from a single test in chapter 5, we have only modelled thermal electron distributions. By assuming that the electrons were always described by a relativistic Maxwellian, we are automatically assuming a fast thermalization timescale. However, the predictive method to maintain self consistency (described in chapter 6) is constructed using δ functions and can be applied to *any* distribution. As a result we can model totally non–thermal electron heating mechanisms or hybrid plasmas.

Bulk motion of the electron region can also have enormous effects on the timing and spectral behaviour of a system. If we insert an angle dependent velocity β into the electron distribution we can model a system where the hot electron cloud is approaching or receding at almost any speed. We could even vary β with time and so model a rising and falling magnetic flare region.

7.3 New geometries

As we have said at a number of points, the method is generalizable to any geometry. However, we have limited ourselves to either infinite parallel planes or cylinders. This is because more complex geometries have higher memory and run–time requirements. In theory it would be possible to calculate the scattering in a string or a sphere. The primary limitation would be set by the amount of symmetry in the geometry. Less symmetric cell systems would require that the distributions in a greater number of cells to be held in the memory at any one time. If this problem could be overcome, the applications are obvious. For example, a sphere with light entering from an external, equatorial source would be a good model for a hot flow (ADAF or SLE).

To maintain a reasonable run–time we have used the fact that the photons and electrons are symmetric in ϕ. Any geometry in which this is not the case will take a longer time to run (16 times longer on the present angle grid) which makes such geometries impossible at present.

7.4 New interactions

Modelling particle interactions other than Compton scattering should be reasonably simple. Replacing the equations for the Compton output energy and cross–section with those for a new process would be enough for most situations. In those cases where the encountered photon is virtual a new photon distribution would have to be generated which would depend on other parameters (*e.g.* Magnetic field strength). This sort of adjustment would allow us to model Synchrotron/cyclotron radiation. By allowing more than one type of interaction to occur we could model situations

where several processes are happening together.

Modelling processes like pair production would be less simple. In that case, two high energy photons collide to form an electron and positron pair. The number of each type of particle is not conserved during the scattering. We would therefore need to model a photon distribution which encounters itself and store the resulting particles in separate electron and positron distributions. This would require full angular distributions for *all* the particles as described above. Although modelling such systems would require sweeping changes to the distribution storage sections of the code, the principles of modelling the scattering and correcting for a large angle grid remain sound.

We could also model other electron interactions. Given a non–thermal input we can find the thermalization timescale (a result of Coulomb collisions) and calculate the level of thermalization after a given time. From there we can create an electron distribution which contains a low energy thermal component and a high energy non–thermal tail. We can predict the behaviour of any electron distribution using this sort of method. With sufficient memory it should be possible to make the electron distribution angle dependent in the same fashion as the photon distribution. This could then model anisotropic electron distributions which could evolve naturally from anisotropic Compton cooling. We could also model angle dependent Coulomb cooling which will change the angle dependence of the electrons as they are thermalized.

7.5 Comptonization of reflection

In chapter 3 we mentioned that subsequent Comptonization of a reflected spectrum can be difficult to model. This Compton scattering of reflected photons takes place in both the disk and the electron atmosphere. The second of these processes is included automatically in our code because the reflected photons (which have to pass through the medium to escape) are treated identically to non–reflected photons. It is also included in the model of Petrucci et al. (2001). In our model, we could find the effect of Comptonization at various temperatures on the reflection profile by suppressing the initial photon spectrum. Although the code is presently too slow

to allow direct data fitting it should be possible to create a data table of reflection profiles which could be interpolated over on a reasonable timescale.

7.6 Correcting for the coarse angle grid

As we discussed in chapter 5 the code requires a correction if the cross–section is very peaked. We also mentioned that the coarse angle grid still introduces instabilities when the output photon and input electron are not quite aligned. Since we have a working method for the head on correction, it should be possible to use that method in general. Replacing the core code with one that uses the χ probability method would generate accurate results for *any* angular combination, irrespective of the angle grid used. In the head on situation the probability of a particular combination of angles within a bin is easily modelled (especially because there is a symmetry over ϕ). If we were to use the method in general, we would have to calculate the probability of each sub–bin angle for *every* possible combination of input and output bins.

7.7 Summary

The code outlined in this thesis is a significant advancement of Guilberts's original methodology (Guilbert 1981). We have removed many of the approximations, which were only applicable to non-relativistic systems, and can predict the scattering behaviour of *any* electron distribution. We have also developed a method by which self consistent cooling can be included and so hugely increased our ability to model time dependence in Compton scattering. Even so, there is still room for plenty of further work. The principle of calculating the individual distribution functions within contiguous cells is almost infinitely usable, not only for Compton scattering but for any particle process. Equally, time dependence is always a feature of such systems.

In time, a code of this sort cold be adapted to model the full time dependent behaviour of the disk/corona structure. It could be coupled with magneto-hydrodynamic models of an accretion disks which accurately model both the radi-

ation and reflection of the disk. By including a temporal feedback from the corona we could measure the effects of each part of the system on the other. We could also use the arbitrary geometry of our modelled system to find measurable timing differences between ADAF and coronal models of electron clouds. Given enough time, we could create combined programs which can model all parts of an accreting system as it changes over time (*e.g.* over an outburst). The only limit at present is that of computer memory and speed and since computer technology is moving so fast at this time, that should not remain a limit for long.

Bibliography

Abramowicz M.A., Jaroszynski M., Sikora M., 1978, A&A, 63, 221

Abramowicz M.A., Czerny B., Lasota J.-P., Szuszkiewicz E., 1988, ApJ, 332, 646

Abramowicz M.A., Igumenshchev I.V., Quataert E., Narayan R., 2002, ApJ, 565, 1101

Agol E., Krolik J.H., 2000, ApJ, 528, 161

Arnaud K. A., 1996, in: Jacoby G. H., Barnes J., eds., Astronomical Data Analysis Software and Systems V, ASP Conf. Series Vol. 101, San Francisco, p. 17

Atoyan A.M., Aharonian F.A., 1996, MNRAS, 278, 525

Audley M.D, 1998, PhD Thesis, University of Maryland

Balbus S.A., Hawley J.F., 1991, ApJ, 376, 214

Balbus S.A., Papaloizou J.C.B., 1999, ApJ, 521, 650

Barrio E., Done C., Nayakshin S., 2003, MNRAS, Accepted.

Beloborodov A.M. 1999, ApJ, 510, L123

Blumenthal G.R., Gould R.J. 1970, Rev Mod Phys, 42, 237

Böttcher M., Liang E.P., 1999, ApJ, 511, L38

Burderi L., King A.R., Szuszkiewicz E., 1998, 509, 85

Cannizzo J.K., 1998, ApJ, 494, 366

Chakrabarti S., Titarchuk L.G., 1995, ApJ, 455, 623

Chen X., Abramowicz M.A., Lasota J.-P., Narayan R., Yi I., 1995, ApJ, 443, L61

Coppi P.S., 1999, in: Poutanen J., Svensson R., eds., High Energy Processes in Accreting Black Holes, ASP Conference Series 161, 375

Coppi P.S., 2000, AAS HEAD, 32, 2311

Cowley A.P., 1992, ARA&A, 30, 287

Crary D.J., et al. 1998, ApJ, 493, 71

Cui W., Zhang S.N., Focke W., Swank J.H., 1997, ApJ, 484, 383

Cui W., Zhang S.N., Chen W., Morgan E.H., 1999, ApJ, 512, 43

Cui W., 1999, ApJ, 524, L59

Cui W., Zhang S.N., Chen W., Morgan E.H., 2000, ApJ, 531, L45

di Matteo T., 1998, MNRAS, 299, L15

di Matteo T., Psaltis D., 1999, ApJ, 526, L101

Done C., 1989, PhD Thesis, IoA, University of Cambridge

Done C., Mulchaey J.S., Mushotzsky R.F., Arnaud K.A., 1992, ApJ, 395, 275

Done C., Życki P.T., 1999, MNRAS, 305, 457

Done C., Nayakshin S., 2001, ApJ, 546, 419

Done C., Gierliński M., 2003, MNRAS, Forthcoming.

Dove J.B., Wilms J., Begelman M.C., 1997, ApJ, 487, 747

Dubus G., Hameury J.-M., Lasota J.-P., 2001, A&A, 373, 251

Ebisawa K., et al. 1994, PASJ, 46, 375

Eddington A.D., 1925, MNRAS, 85, 408

Esin A.A., 1997, ApJ, 482, 400

Esin A.A., McClintock J.E., Narayan R., 1997, ApJ, 489, 865

Fabian A.C., Rees M.J., 1979, Proc. Symp. X–ray Astr., 381, Publisher: Pergamon, Oxford

Fabian A.C., Rees M.J., Stella L., White, N.E. 1989, MNRAS, 238, 729

Fabian A.C., Iwasawa K., Reynolds C.S., Young A.J., 2000, PASP, 112, 1145

Fender R., 2000, In: L. Kaper, E.P.J. van den Heuvel and P.A. Woudt, eds., 'Black Holes in Binaries and Galactic Nuclei', Springer-Verlag.

Fleming T.P., Stone J.M., Hawley J.F., 2000, ApJ, 530, 464

Frank J., King A., Raine D., 1992, Accretion Power in Astrophysics. Publisher: Cambridge University Press.

Frontera F. et al., 2000, ApJ, 546, 1027

Galeev A.A., Rosner R., Vaiana G.S., 1979, ApJ, 229, 318

Gammie C.F., Menou K., 1998, ApJ, 492, L75

Garcia M.R., Murray S.S, McClintock J.E., Narayan R., 2000, AAS, 19711804G

George I.M. Fabian A.C., 1991, MNRAS, 249, 352

Ghisellini G., 1989, MNRAS, 236, 341

Ghissellini G., George I.M., Fabian A.C., Done C., 1991, MNRAS, 248, 14

Ghisellini G., Haardt F., Fabian A.C., 1993, MNRAS, 263, L9

Giacconi R., Gursky H., Paolini F., Rossi B., 1962, Phys Rev Lett, 9, 439

Gierliński M., Zdziarski A. A., Done C., Johnson W. N., Ebisawa K., Ueda Y., Phlips F., Haardt F., 1997, MNRAS, 288, 958

Gierliński M., Zdziarski A.A., Poutanen J., Coppi P.S., Ebisawa K., Johnson W.N., 1999, MNRAS, 309, 496

Gierliński M. 2000, PhD Thesis, Nicolous Copernicus Astronomical Centre, Warsaw

Gierliński M., Maciolek–Niedzwiecki A., Ebisawa K., 2001, MNRAS, 325, 1253

Gilfanov M., Churazov E., Revnivtsev M., 1999, A&A, 352, 182

Gilfanov M., Churazov E., Revnivtsev M., 2000, Proceedings of the 5th CAS/MPG workshop on High Energy Physics (Astro-ph 0002415)

Gorbatsky V.G., 1965, Proceedings of Leningrad University Observatory, 22, 16

Gorecki A., Wilczewski W., 1984, AcA, 34, 141

Grant, R., Naylor D., 1989, 'Red Dwarf: Marooned', BBC / Paul Jackson Productions

Grove J.E. et al., 1998, ApJ, 500, 899

Guilbert P.W., 1981, MNRAS, 197, 451

Guilbert P.W., Fabian A.C., Ross R.R., 1982, MNRAS, 199, 763

Guilbert P.W., Fabian A.C., 1982, Nature, 296, 226

Guilbert P.W., Fabian A.C., Rees M.J., 1983, MNRAS, 205, 593

Guilbert P.W., 1986, MNRAS, 218, 171

Haardt F., Maraschi L., 1991, ApJ, 380, 51

Haardt F., Maraschi L., 1993, ApJ, 413, 507

Haardt F., 1993, ApJ, 413, 680

Haardt F., Maraschi L., Ghisellini G., 1994, ApJ, 432, L95

Haardt F., Done C., Matt G., Fabian A.C., 1993, ApJ, 411, L95

Hoshi R., 1979, Prog. Theor. Phys., 61, 1307

Hua X.-M., Titarchuk L., 1996, ApJ, 469, 280

Igumenshchev I.V., Chen X., Abramowicz M.A., 1996, MNRAS, 278, 236

Igumenshchev I.V., Abramowicz M.A., Novikov I.D., 1998, MNRAS, 298, 1069

Igumenshchev I.V., Abramowicz M.A., 1999, MNRAS, 303, 309

Igumenshchev I.V., Abramowicz M.A., 2000, ApJS, 130, 463

Igumenshchev I.V., Abramowicz M.A., Narayan R., 2000, ApJ, 537, L27

Illarionov A.F., Sunyaev R.A., 1972, Astro Zh, 49, 58

Janiuk A., Czerny B., Siemiginowska A., 2002, ApJ, 576, 908

Kazanas D., Hua X.-M., Titarchuk L., 1997, ApJ, 480, 735

Kerr R.P., 1963, Phys Rev Lett, 11, 237

King A.R., Ritter H., 1998, MNRAS, 293, 42

Krolik J.H., 1999, Active Galactic Nuclei, Publisher: Princeton University Press

Kubota A., et al. 2003, In preparation

Laor A., 1990, MNRAS, 246, 369

Lasota J.P., Abramowicz M.A., Chen X., Krolik J., Narayan R., Yi I., 1996, ApJ, 462, 142

Lasota J.-P., 2001, NewAR, 45, 449

Laurant P., Titarchuk L.G., 1999, ApJ, 511, 289

Lightman A.P., Eardley D.M., 1974, ApJ, 187, L1

Lightman A.P., White T.R., 1988, ApJ, 335, 57

Lin D.N.C., Papaloizou J.C.B., Faulkner J., 1985, MNRAS, 305, 473

Lynden-Bell 1969, Nature, 223, 690

Maccarone T.J., Coppi P.S., Poutanen J., 2000, ApJ, 537, L107

Magdziarz P. Zdziarski A.A., 1995, MNRAS, 273, 837

Magorrian J., et al. 1998, ApJ, 115, 2285

Malzac J., Jourdain E., 2000, A&A, 359, 843

Malzac J., Beloborodov A.M., Poutanen J., 2001, MNRAS, 326, 417

Massaro E., Cusumano G., Litterio M., Mineo T., 2000, A&A, 361, 695

Matt G., Perola G.C., Piro L. 1991, A&A, 247, 25

Menou K., Hameury J-.M., Lasota J-.P., Narayan R., 2000, MNRAS, 314, 498

Merloni A., Fabian A.C., Ross R.R., 2000, MNRAS, 313, 193

Meyer F., Meyer–Hofmeister E., 1994, A&A, 288, 175

Meyer–Hofmeister E., Meyer F., 1999, A&A, 348, 154

Migliari S., Vignarca F., Belloni T., 2001, ApSSS, 276, 183

Mineshige S., Osaki Y., 1983, PASJ, 35, 377

Miyamoto S., Kitamoto S., Mitsuda K., Dotani T., 1988, Nature, 336, 450

Miyamoto S., Kitamoto S., Nature, 1989, 342, 773

Miyamoto S., Kimura K., Kitamoto S., Dotani T., Ebisawa K., 1991, ApJ, 383, 784

Morrison R., McCammon D., 1983, ApJ, 270, 119

Mukai K., Wood J.H., Naylor T., Schlegel E.M., Swank J.H., 1997, ApJ, 475, 812

Narayan R., Yi I., 1995, ApJ, 452, 710

Narayan R., Garcia M.R., McClintock J.E., 1997, ApJ, 478, L79

Narayan R., Mahadevan R., Quataert E., 1998, in: Abramowicz M.A., Bjornsson G., Pringle J.E., eds., The Theory of Black Hole Accretion Disks, Cambridge University Press, 148

Narayan R., Igumenshchev I.V., Abramowicz M.A., 2000, ApJ, 539, 798

Nayakshin S., 2000, ApJ, 534, 718

Nayakshin S., Kazanas D., Kallman T.R., 2000, ApJ, 537, 833

Nayakshin S., Svensson R., 2001, ApJ, 551, L67

Nolan P.L., et al. 1981, ApJ, 246, 494

Nowak M.A., 1995, PASP, 107, 1207

Nowak M.A., Wagoner R.V., Begelman M.C., Lehr D.E., 1997, ApJ, 477, L91

Nowak M.A., Vaughan B.A., Wilms J., Dove J.B., Begelman M.C., 1999, ApJ, 510, 874

Orosz J.A., et al. 2002, ApJ, 568, 845

Osaki Y., 1974, PASJ, 26, 429

Osaki Y., 1996, PASP, 108, 39

Payne D.G., 1980, ApJ, 237, 951

Petrucci, P.O., Merloni A., Fabian A., Haardt F., Gallo E., 2001, MNRAS, 328, 501

Pietrini P., Krolik J.H., 1995, ApJ, 447, 526

Piran T., 1978, ApJ, 221, 652

Popham R., Sunyaev R.A., 2001, ApJ, 547, 355

Pounds K.A., Nandra K., Stewart G.C., George I.M., Fabian A.C., 1990, Nature, 344, 132

Poutanen J., Svensson R., 1996, ApJ, 470, 259

Poutanen J., Krolik J. H., Ryde F., 1997, MNRAS, 292, 21

Poutanen J., Coppi P.S., 1998, Phys. Scripta T77 57-59

Poutanen J., Fabian A.C., 1999, MNRAS, 306, L31

Poutanen J., 2001, Adv Space Res, 28, 267

Pottschmidt K., Wilms J., Nowak M.A., Heindl W.A., Smith D.A., Staubert R., 2000, A&A, 357, L17

Pozdnyakov L.A., Sobol I.M., Sunyaev R.A., 1983, in: Sunyaev R., ed., Astrohphys. & Space Phys. Rev., Harwood Academic Publishers, Chur, Vol. 2, p. 189

Pravdo S.H. Angelini L., Harding A.K., 1997, ApJ, 491, 808

Preidhorsky W., Garmire G.P., Rothschild R., Boldt E., Serlemitsos P., Holt S., 1979, ApJ, 233, 350

Prendergast K.H., 1960, ApJ, 132, 162

Prendergast K.H., Burbidge G.R., 1968, ApJ, 151, L83

Pringle J.P., Rees M.J., 1972, Astron. Aph., 21, 1

Pringle J.P., Rees M.J., Pacholczyk A.G., 1973, A&A, 29,179

Psaltis D., Norman C., 2003, astro-ph, 0001391

Quataert E., Gruzinov A., 1999, ApJ, 520, 248

Quataert E., Narayan R., 1999, ApJ, 520, 298

Quataert E., Gruzinov A., 2000, ApJ, 539, 809

Reig P., Belloni T., van der Klis M., Mendez M., Kylafis N.D., Ford E.C., 2000, ApJ, 541, 883

Remillard R. A., McClintock J. E., Sobczak G. J., Bailyn, C. D., Orosz J. A., Morgan E. H., Levine A. M., 1999, ApJ, 517, L127

Remillard R.A., Sobczak G.J., Muno M.P., McClintock J.E., 2002, ApJ, 564, 962

Ross R.R., Fabian A.C., 1993, MNRAS, 261, 74

Ross R.R., Fabian A.C., Young A.J., 1999, MNRAS, 306, 461

Rowan-Robinson M., 1977, ApJ, 213, 638

Różańska A., Czerny B., 2000, A&A, 360, 1170

Rybicki G.B., Lightman A.P., 1979, Radiative processes in astrophysics, Publisher: Wiley-Interscience.

Sanchez-Fernandez C., Castro-Tirado A.J., Duerbeck H.W., Mantegazza L., Beckmann V., Burwitz, V., Vanzi L., Bianchini A., della Valle M., Piemonte A., Dirsch B., Hook I., Yan L., Giminez A. 1999, A&A, 348, L9

Sazonov S.Y., Sunyaev R.A., 2000, AstrL, 26, 494

Shahbaz T., Groot P., Phillips S.N., Casares J., Charles P.A., van Paradijs J., 2000, MNRAS, 314, 747

Shakespeare W., 1609, in: Tyler T., Shakespeare's Sonnets, Ballantyne Press, 1890

Shakura N.I., 1972, Aston. Zh., 49, 921

Shakura N.I., Sunyaev R.A. 1973, A&A, 24, 337

Shapiro S.L., Lightman A.P., Eardley D.M. 1976, ApJ, 204, 187

Sobczak G.J., McClintock J.E., Remillard R.A., Levine A.M., Morgan E. H., Bailyn C.D., Orosz J.A., 1999, ApJ, 517, L121

Smak J., 1982, Acta Astr., 32, 199

Smak J., 1984, Acta Astr., 34, 161

Smak J., 1999, Acta Astr., 49, 391

Stella L., Rosner R., 1984, ApJ, 277, 312

Stella L. Vietri M., 1998, ApJ, 492, L59

Stern B.E., Begelman M.C., Sikora M., Svensson R., 1995a, MNRAS, 272, 291

Stern B.E., Poutanen J., Svensson R., Sikora M., Begelman M.C., 1995b, ApJ, 449, L13

Stone J.M., Pringle, J.E., Begelman M.C., 1999, MNRAS, 310, 1002

Sunyaev R.A., Trumper J., 1979, Nature, 279, 506

Sunyaev R.A., Titarchuk L.G., 1980, A&A, 86, 121

Sutherland P.G., Weisskopf M.C., Kahn S.M., 1978, ApJ, 219, 1029

Szuszkiewicz E., Miller J.C., 2001, MNRAS, 328, 36

Titarchuk L., 1994, AJ, 434, 570

Titarchuk L., Lyubarskij Y., 1995, ApJ, 450, 876

Titarchuk L., Hua X-.M., 1995, ApJ, 452, 226

Treves A., Maraschi L., Abramowicz M., 1988, PASP, 100, 427

Ueda Y., et al. 2002, ApJ, 571, 918

van der Klis M., 1994, ApJS, 92, 511

van der Klis M., 1995, Lecture notes in Physics, 454, 321

van der Klis M., 2000, ARA&A, 38, 717

van Paradijs J., Verbunt F., 1984 in: Woosley S.E., ed., High Energy Transients in Astrophysics, AIP Conf. Proc., New York, 49

van Paradijs J., 1996, ApJ, 464, L139

Wagoner R.V., Silbergleit A.S., Ortega–Rodríguez M., 2001, ApJ, 559, L25

Wandel A., Liang E.P., 1991, ApJ, 380, 84

Weaver K.A., Krolik J.H., Pier E.A., 1998, ApJ, 498, 213

Weisskopf M.C., Kahn S.M., Sutherland P.G., ApJ, 1995, 199, L147

White N.E., Nagase F., Parmar A.N., 1995, in: Lewin W.H.G., van Paradijs J., van den Heuvel E.P.J., eds., X–Ray Binaries, Cambridge University Press

Wijnands R., Homan J., van der Klis M., 1999, ApJ, 526, 33

Wilson C.D., Done C., 2001, MNRAS, 325, 167

Zdziarski A.A., Johnson N.W., Done C., Smith D.A., McNaron–Brown K., 1995, ApJ, 438, L63

Zdziarski A.A., 1998, MNRAS, 296, L51

Zdziarski A.A., Johnson W.N., Magziarz P., 1999, MNRAS, 283, 193

Zdziarski A.A., Lubiński P., Smith D.A., 1999, MNRAS, 303, 11

Zdziarski A.A., 2000, in: Martens P.C.H., Tsuruta S., Wever M.A., eds., Highly Energetic Physical Processes and Mechanisms for Emission from Astrophysical Plasmas, Astron. Soc. Pac., p. 153

Zdziarski A.A., Grove E.J., Poutanen J., Rao A.R., Vadawale S.V., 2001, ApJ, 554, L45

Zdziarski A.A., Poutanen J., Paciesas W.S., Wen L., 2002, ApJ, 578, 357

Zeldovitch Y.B., Novikov I.D., 1971, 'The theory of the gravitation and stars evolution', Nauka, Moscow

Zhang S.N., Cui W., Chen W., 1997, ApJ, 482, L155

Życki P.T., Czerny, B. 1994, MNRAS, 266, 653

Życki P.T., Done C., Smith D.A., 1997, ApJ, 488, L113

Życki P.T., Done C., Smith D.A., 1998, ApJ, 496,L25

Życki P.T., Done C., Smith D.A., 1999, MNRAS, 305, 231

Życki P.T., Done C., Smith D.A., 2001, MNRAS, 326, 1367